KTH Electrical Engineering

Analysis of a Novel Transverse Flux Machine with a Tubular Cross-section for Free Piston Energy Converter Application

ALIJA COSIC

Doctoral Thesis
Stockholm, Sweden 2010

TRITA-EE 2010:044
ISSN 1653-5146
ISBN 978-91-7415-786-4

KTH School of Electrical Engineering
SE-100 44 Stockholm
SWEDEN

Akademisk avhandling som med tillstånd av Kungl Tekniska högskolan framlägges till offentlig granskning för avläggande av teknologie doktorsexamen i datalogi Fredagen den 19:e november 2010 klockan 10.00 i Sal B2, Kungl Tekniska högskolan, Valhallavägen 79, Stockholm.

Tryck: Universitetsservice US AB

Abstract

Constantly growing need for oil, all over the world, has caused oil price to rise rapidly during the last decade. High oil prices have made fuel economy as one of the most important factors when consumers are buying their cars today. Realizing this, many car manufacturers have developed or are looking for some alternative solutions in order to decrease fuel consumption. Combining two different technologies in a vehicle, the so called hybrid vehicle, can be seen as the first step toward a better and more sustainable development.There are several different solutions for hybrid vehicles today, among the best known are the Serie Electric Hybrid Vehicle (SEHV), the Parallel Electric Hybrid Vehicle (PEHV) and the Serie-Parallel Hybrid Electric Vehicle (SPEHV).

By integrating a combustion engine with a linear electric machine into one unit, a system that is called Free Piston Energy Converter (FPEC) is achieved. The FPEC is suitable for use in a SEHV. Other application areas like stand alone generator are also possible.

In this report a novel Transverse Flux Machine (TFM) with a tubular cross section of the translator has been investigated. Application of the machine in a FPEC has put tough requirement on the translator weight, specific power and force density. Different configurations of the winding arrangements as well as the magnet arrangement have been investigated. It has been concluded that the buried magnet design suffers from high leakage flux and is thus not a suitable TFM concept. Instead the surface mounted magnet design has been chosen for further investigation. An analytical model has been developed and a prototype machine has been built based on the analytical results. In order to have a better understanding of the machine characteristic a 3D-FEM analysis has been performed.

The results from the analytical model, FEM model and measurements are analyzed and compared. The comparison between the measured and FEM-simulated results shows very good agreement. Furthermore, the results from the analytical model indicates that it can be successfully developed for further analysis and optimization of the design to give a cost-effective solution of the novel generator for mass production.

Sammanfattning

Det ständigt växande behovet av oljan runt om i världen, har fått oljepriset att stiga snabbt under det senaste decenniet. Detta har gjort bränsleekonomin till en av de viktigaste faktorer när konsumenterna väljer sina bilar i dag. Många biltillverkare har därför utvecklat eller söker efter alternativa lösningar till dagens förbränningsmotorer i hopp om att minska bränsleförbrukningen. Ett hybridfordon, ett fordon som är försedd med fler än en energiomvandlare, kan ses som ett första steg mot en bättre och mer hållbar utveckling. Det finns flera olika lösningar för hybridfordon i dag, bland de mest kända är Seriehybrid, Parallellhybrid och Serie-Parallelhybrid fordon.

Genom att integrera en förbränningsmotor med en linjär elektriskmaskin, erhålls ett system som kallas Frikolvsenergiomvandlare. Dennna typ av energiomvandlare lämpar sig bäst för användning i en seriehybridfordon, men andra användningsområden som fristående generator är också möjliga.

I denna avhandling har en ny typ av Transversalflödesmaskin (TFM) med en cirkulärt tvärsnitt undersökts. Tillämpningen av maskinen i en Frikolvsenergiomvandlare har medfört tuffa krav på translatorvikten, specifikeffekten och kraftdensiteten. Olika lindnings- och magnetkonfiguratationer har undersökts. Forskningen har visat att designen med begravdamagneter lider av stort läckflöde och är därför inte lämplig för det nya TFM koncept. Istället har designen med ytmonterade magneter valts för vidare undersökning. En analytisk modell har utvecklats och en prototyp maskin har byggts med utgångspunkt i analysresultaten. För att få en bättre förståelse av maskinkarakteristiken har en 3D-FEM modell tagits fram och analyserats.

Resultaten från den analytiska modellen, FEM modellen och mätningar har analyserats och jämförts. Överensstämmelsen mellan de simulerade och de uppmätta resultaten är mycket bra. Dessutom, resultaten från den analytiska modellen visar på att modellen kan framgångsrikt användas för fortsatt analys och optimering av maskinen för att ge en kostnadseffektivlösning för masstillverkning.

Acknowledgements

First time I entered the door of the Department of Electrical Machines and Power Electronics was in the beginning of 2001. From then until now the time spent here will probably be the most rememberable part of my life.

First I would like to thank my supervisor Prof. Chandur Sadarangani for his guidance, support and encouragement throughout this project. I would also like to thank him for making this project possible.

I would like to thank Tek. Lic. Mats Leksell and prof. Hans-Peter Nee for useful discussions on the subject.

My gratitude goes to the to my former co-supervisors Dr. Peter Thelin and Dr. Fredrik Carlson who have contributed with valuable input to the project. I'm indebted to Dr. Waqas Arshad who kindly answered my questions in the beginning of the project and showed me the way into the world of linear machines.

This project is funded partly by the EU commission and partly by the Swedish Energy Agency which I hereby gratefully acknowledge. Furthermore, I would also like to acknowledge all the participants in the FPEC project with whom I shared many interesting meetings followed by good discussions.

My special thanks goes to mr. Jan-Olov Brännvall and mr. Jan Timmerman who have been of great help during the construction of the prototype and for their encouragement during this project. I further would like to thank the staff at Emaus Mekaniska AB and especially Bertil who made the majority of parts for the prototype machine and also contributed with many useful suggestions.

Thanks to Ass. Prof. Juliette Soulard for helping me solve some problems with the Flux3D software.

Two special thanks goes to my former room mates Jörgen and Alexander for interesting discussion and for their good company.

As mentioned the time will be the most memorable in my life and I hereby would like to express my gratitude to the staff and my fellow PhD students who very much contributed to a nice time and relaxed working atmosphere at the Department. Thank you Tommy, Oskar, Lennart, Stefan, Noman, Antonios, Rathna, Henrik, Kalle, Nicklas, Kashif, Andreas,

Naveed, Tomas, Shafigh, Dimosthenis, Samer, Dmitry, Georg, Shuang, Stephan, Florance, Freddy, Mattias, Karsten, Staffan, Lilantha, Torbjörn, Erik, Björn, Robert, Hailian.

Special thanks to Eva Petersson and Emma Petterson for help with financial issues and Peter Lönn for the computer support.

Finally I would like to thank my parents and my family, my wife Mirsada and my dotter Sara for their love and support and for their lovely smiles.

Contents

Chapter 1

Introduction

In recent decades, the number of newly discovered large oil wells have been few, or almost none at all. Based on this fact and the level of the current oil consumption, it can be predicted that there will be an acute shortage of oil within less than a few decades. This is a major problem for the world's economy and further development since oil has been the single largest energy source in the world from the 60s onwards. In order to retain the present level of development and avoid a crisis similar to the oil crisis in the middle 70s, oil consumption in the world has to be decreased, or some alternative energy sources has to be found.

The transportation sector is one of the largest oil consumers in a global perspective, and as such it also offers considerable scope for improvements. Vehicles equipped with an Internal Combustion Engine (ICE) have been around for more than a century. Ever since its introduction the performance of the ICE has improved continuously and has gone through dramatic change. However, the technology based on the ICE will still require oil, the question is how far this technology can be improved and what are the alternatives.

One solution is to get rid of oil as the main energy source and develop a propulsion system that can utilize other sources as the primary energy source. Examples of such are the fuel cell and pure electric vehicles. However, there are some technological issues that these vehicles have to overcome before they can enter the market broadly. One difficulty with fuel cell vehicles is simply the infrastructure for the supply of hydrogen. There are also some safety issues regarding the fuel storage. In the case of electrical vehicles the biggest challenge is the batteries. The driving range of the vehicle strongly depends on the battery size. Furthermore, once the battery is empty the recharging time is too long. Electrical vehicles may however be seen as a complementary solution to the hybrid technology as the majority of the cars actually have a drive cycle that makes it possible

to optimize the electrical system of the vehicle so that the problems mentioned above can be avoided. This is very obvious when the passenger car is to be used only to drive back and forth to work.

There is another problem that is closely related to the oil consumption, and that is the emissions of the harmful particles and carbon dioxide. Transport's contribution to the emissions within the EU and especially within big cities is so large that dramatic reductions are necessary. In some cities in the U.S. emissions of pollutants from traffic are regulated by laws. However, these measures have a limited impact on emissions and can only be seen as a last resort. To really get to the problem more radical action needs to be taken.

A solutions that is broadly accepted today is the combination of the electric propulsion system together with the internal combustion engine. With the electrical machine, the combustion engine can be complemented and downsized accordingly. Furthermore, the combustion engine can be adjusted to operate optimally, which in the end reduces the oil consumption.

There exist several different solutions of hybrid cars on the market today. Most of these are equipped with conventional engines. One common problem with these is the crankshaft, where the compression volume can not be varied. Hence, the combustion process is more or less determined in prior. The only possible control of the process takes place through the time adjustment of the fuel injection. In diesel-propelled engines, for example, there exists a trade off between efficiency and NOx exhaust gases. An increase in efficiency implies an increase of NOx particles and vice versa. However, it is possible to keep the efficiency at a high level, and still reduce the exhaust of the NOx particles. The solution is called 'Homogeneous Charge Compression Ignition' (HCCI). One of the key parameters in achieving a good HCCI process is the possibility of variable compression. The HCCI is achieved easily in an 'Free Piston Energy Converter' (FPEC).

FPEC is also an acronym of a European project, which aims at creating a bridge between today's existing technologies and future technologies.

1.1 Objectives

The project's objective is to achieve high efficiency and reduce emissions of dangerous particles. The technology is intended to be used primarily for automotive applications but, it can also be used in a number of other applications, such as an auxiliary power unit or for distributed power generation. The new technology is based on a free piston principle, which comprises a combustion system and an electric generator for the conversion of mechanical energy into electrical energy. It will use diesel as a fuel but it is also conceivable that other types of fuels can be used.

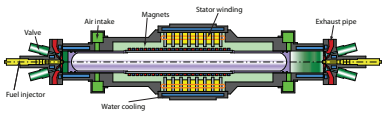

Figure 1.1: *Schematic view of the FPEC*

Electric machinery is a very important part of a FPEC. The main goal for the FPEC project is to develop an electrical machine with the following requirements:

- Moving mass of electrical machine: 6 kg.
- Electrical machine nominal force: 2.7 kN, (9 kg, 32 Hz, 10.5 $\frac{\mathrm{m}}{\mathrm{s_{max}}}$, 8300 $\frac{\mathrm{m}}{\mathrm{s^2}}$ max).
- Electrical machine operating force: 4 kN, (9 kg, 37 Hz, 12.2$\frac{\mathrm{m}}{\mathrm{s_{max}}}$, 9200 $\frac{\mathrm{m}}{\mathrm{s^2}}$ max)
- Electrical machine specific power: > 1 $\frac{\mathrm{kW}}{\mathrm{kg}}$.
- Efficiency: > 90 %

In most electrical machines the flux plane lies in the same plane as the force produced. In order to decrease the iron losses the stator and the rotor are stacked with thin iron sheets. Thus, the iron sheets or iron laminations have to coincide with the flux plane. In linear machines, this can sometimes imply a difficulty in the production process.

In a Transverse Flux Machines (TFM), the force produced and the flux plane are perpendicular to each other. Therefore, in the novel linear TFM the stator is similar to the stator of any conventional rotating machine. This has an important advantage in the manufacturing process of the machine.

The TFM machines are characterized by high specific torque density (force density), high magnetic flux leakage, poor displacement power factor, and complicated manufacturing procedures. However, the complicated manufacturing process is often related to the rotating machines. In this work, a major emphasis has been put to design a linear generator that is easy to manufacture and thereby making it possible to achieve a cost-efficient solution for the generator.

1.2 Thesis outline

Chapter 2 presents different topologies of Hybrid Electrical Vehicles. The drawbacks and advantages for different topologies are discussed.

Chapter 3 gives a more detailed description of the Free Piston Energy Converter (FPEC). The challenges and advantages of the FPEC system together with their drawbacks are discussed. Other similar projects are analyzed and presented.

Chapter 4 describes different Transverse Flux Machines (TFM) topologies. Basic differences between the conventional electrical machine and the TFM machine are explained. Some peculiar features of the TFM machines are discussed and explained.

Chapter 5 gives a detailed description of the novel topology. Aspects on different magnet and winding layouts are given. Based on this discussion one concept is chosen for the prototype dimensioning.

Chapter 6 presents an analytical model of the novel topology. A basic model and an improved model for the calculation of flux is given. Calculation of cogging force is also given.

Chapter 7 describes the Finite Element Method and the software that is used in the analysis. Results from the 3D-FEM simulations are presented and analyzed.

Chapter 8 presents the manufacturing process of the prototype. A different manufacturing method that has been used is explained. This is the major advantage and challenge of the novel topology.

Chapter 9 presents the measurement results. It also discusses some deviations from the analytical and simulated results.

Chapter 10 presents the conclusions of the project and also gives some directives for future work.

1.3 Publications

1. A. Cosic and C. Sadarangani and F. Carlsson *A novel concept of a Transverse Flux Linear Free-Piston Generator* Linear Drives for Industry Applications, Kobe-Awaji, Japan, 2005, 318–321.

2. A. Cosic and C. Sadarangani and D. Svechkarenko *A prototype design of a novel transverse flux machine for the free piston energy converter* In. Proc. Nordic Workshop on Power and Industrial Electronics, Lund Sweden, June 2006.

3. A. Cosic and C. Sadarangani and M. Leksell *Cogging torque calculations for a novel concept of a Transverse Flux Linear Free-Piston Generator* Linear Drives for Industry Applications (LDIA2007), Lille, France, 2007.

4. A. Cosic and C. Sadarangani and M. Leksell *3D analysis of a novel Transverse Flux machine for a free piston energy converter* ICEM 2008. 18th International Conference on Electrical Machines, 2008.

5. A. Cosic and C. Sadarangani and J. Timmerman *Design and Manufacturing of a Linear Transverse Flux Permanent Magnet Machines* Industry Applications Society Annual Meeting, 2008.

The author has also published some other papers

1. A. Cosic, J. Lindbäck, W. M. Arshad, M. Leksell, P. Thelin, E. Nordlund *Application of a free-piston generator in a series hybrid vehicle* Linear Drives for Industry Applications, Birmingham, England, 2003.

2. W. M. Arshad, J. Lindbäck, A. Cosic, P. Thelin, M. Leksell *Manufacturing Defects in a Linear Transverse Flux Machine* Linear Drives for Industry Applications, Birmingham, England, 2003.

3. D. Svechkarenko, A. Cosic, J. Soulard, C. Sadarangani *Transverse Flux Machines for Sustainable Development - Road Transportation and Power Generation* Power Electronics and Drives Systems (PEDS), 2005.

Chapter 2

Different drive trains

This chapter will focus on different drive trains topologies. It will give the definition of a Hybrid Vehicle. Furthermore the benefits versus drawbacks for the different topologies, will be discussed.

2.1 Conventional combustion engine vehicle

Most vehicles today are equipped with an Internal Combustion Engine (ICE) running either on gasoline or diesel. In a conventional vehicle the ICE has a direct connection with the wheels. In order to increase the speed range a gearbox is placed between the engine and the wheel shaft. The gearbox brings along a clutch for a smoother transition.

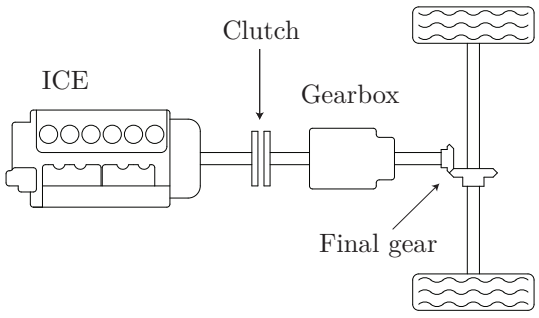

Figure 2.1: *Conventional drive train with ICE, clutch, gearbox and final gear.*

As the load changes the working point of the ICE must change as well, because of the direct connection to the wheels. This means that the ICE operates at numerous different load points with varying efficiency as a result. The maximum efficiency region of an ICE is very narrow, and

to which extent the ICE will operate in this region depends strongly on the drive cycle as well as on the driver.

2.2 Hybrid vehicles

The idea of combining the ICE with an electric motor is not new. Already in 1905 there was a patent that described how the acceleration of the ICE can be boosted by an electrical machine [1]. A definition of "hybrid vehicle" was given by UN in 2003 as follows:

"A hybrid vehicle" is a vehicle with at least two different energy converters and two different energy storage systems (on-board the vehicle) for the purpose of vehicle propulsion. [2].

Roughly, different hybrid concepts can be subdivided into Series Hybrid Electric Vehicle (SHEV), Parallel Hybrid Electric Vehicle (PHEV) or a combination of those i.e. Series Parallel Hybrid Electric Vehicle (SPHEV). However, there are also some other abbreviations for different types of Hybrid vehicles mostly used by industry. These are Full Hybrid (FH), Mild Hybrid and Power Assist Hybrid or Micro Hybrid. These latter abbreviations are an attempt to describe all different kinds of hybrid vehicles.

The definition of the series hybrid and parallel hybrid was proposed by the Technical Committee 69 (Electric Road Vehicles) of the International Electrotechnical Commission [3]

"A series hybrid" is an HEV in which only one energy converter can provide propulsion power.

"A parallel hybrid" is an HEV in which more than one energy converter can provide propulsion power.

The technical progress of the hybrid vehicle has been boosted by various factors. One is the increasing price of oil due to the increase in demand and the limited reservoirs. This has resulted in the development of more fuel-economical cars. Petroleum driven cars have a potential of decreasing their fuel consumption through hybridization. However, compared with cars equipped with the diesel engine they will still have roughly the same efficiency. In Europe the amount of sold diesel cars per year is about 50% of the total number, which is in contrast to the US where the equivalent amount is about 2% or less. It might therefore take a longer time before hybrid cars become a majority in Europe.

Another factor pushing the development of hybrid cars is the government regulations. As the climate change becomes increasingly important exhaust gases such as CO_2 and NO_x just to mention a couple, are expected to meet tougher regulations.

Competition between the Electrical Vehicle and the petroleum driven car already existed at the end of 19^{th} century. As a matter of fact Electrical Vehicles were in the majority on the streets. However, as the combustion engines became more efficient together with better accessibility of petroleum, the range limitation of the electric vehicle became soon evident. Towards the end of 1930's almost no electric cars were sold and so they fell into oblivion until recent years.

Conventional vehicles equipped with the ICE are around 100 years old, therefore this technique can be regarded as mature and almost fully developed. Hybridization of the conventional vehicle implies a more complex system. In many cases this also means a more expensive solution, which in the end consumers have to pay for. The final factor, and probably one that is most difficult to predict, is whether the consumers wants to pay extra for the hybrid vehicle. Nevertheless, in recent years it seems that the consumers willingness to buy a hybrid car has increased together with the awareness for environmental issues.

2.2.1 Full Hybrid

A full hybrid is a vehicle that can utilize all hybrids features. It can run as a purely electric vehicle, as a conventional vehicle or as a combination of these. It also features regenerative braking i.e. the kinetic energy of the vehicle can be extracted and stored in the battery. It offers many different control strategies which can be adopted for different load conditions.

There is also benefit from the downsized combustion engine. In the conventional vehicle all power to the wheels must come from the combustion engine. In order to allow good acceleration characteristics the engine must be sized accordingly. In many cases this leads to a very big combustion engine with a lower energy-efficient vehicle as a result.

In a hybrid vehicle the combustion engine needs only to provide power for a certain constant speed and some battery charge capability. All transient power, during acceleration and steep climb, can be provided by the electrical machine. This implies that the hybrid vehicle can be made very energy-efficient, especially in urban areas where start and stop of the vehicle often occur.

Sometimes in a HEV, although it posses an electrical machine that can provide some additional torque, the size of the ICE is still considerable or not adequately downsized. Thereby, the vehicle can have better acceleration performance compared with conventional vehicles. These hybrids are then refered to as Power Hybrids [1].

Series-Parallel Hybrid Electric Vehicle

The series parallel hybrid vehicle, see Figure 2.2 for the general layout, is one with the most flexibility. It can run as a pure electrical vehicle, or as a conventional vehicle alone or as a combination of those. It is equipped with two electrical machines. One is used to provide additional power to the wheel shaft and for regeneration of the kinetic energy. The other is used as a generator where the power from the ICE is converted into electrical energy and stored in the battery or some other energy storage device. The

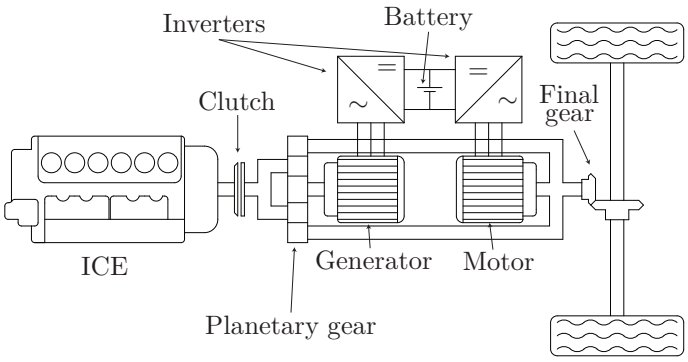

Figure 2.2: *Series-Parallel Hybrid Electric vehicle.*

planetary gear is one of the key component of this configuration. It can be seen as more or less necessary, which makes this configuration somewhat complicated and more costly [4]. The planetary gear is connected to the generator, ICE and the drive shaft and controls the direction of the power flow.

Series Hybrid Electric Vehicle

In a series hybrid vehicle, see Figure 2.3, the ICE does not have any mechanical connection to the drive shaft. All energy is converted to electric energy before it reaches the drive shaft. This configuration is therefore suitable for other energy sources besides the conventional ICE-Generator configuration such as the fuel cells or the Free Piston Energy Converter (FPEC).

Like in other hybrid combinations the ICE does not have to provide all the traction power necessary for the acceleration and the steep climb thus it can be downsized. In fact, because the ICE does not have any mechanical connection with the drive shaft what so ever, it can be optimized even further to operate only at the most efficient point. Thereby, the efficiency of the ICE can be kept at the optimum. Furthermore, the location of

the ICE does not necessarily needs to be close to the wheels. It can be placed in a more suitable place as only electrical connections are required [5]. In order to operate the vehicle in the best possible way the size of the

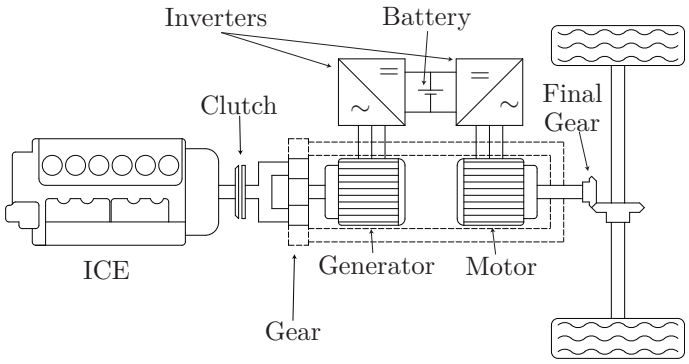

Figure 2.3: *Series Hybrid Electric vehicle.*

battery is of great importance [6]. Small battery capacity requires that the the ICE works over a wider power range and follows the load power more strictly, while a bigger battery allows for more independent and more optimal control of the ICE.

Parallel Hybrid Electric Vehicle

A parallel hybrid topology may be obtained from the Series-Parallel hybrid topology by removing one electrical machine, see Figure 2.4 for the general layout. The remaining electrical machine is then used both as a generator and as a motor. It is used as a motor to provide additional torque when there is a need i.e. during acceleration or a steep climb. It is used as a generator for charging the energy storage component during deceleration and braking, and when necessary.

The parallel topology differs from the series-parallel as the electrical machine is used only as a motor or as a generator at a time. Thus the vehicle can not obtain the maximum torque and charge the energy storage at the same time. In addition, the ICE can not operate at an optimal operating point as the electrical machine only delivers torque and can not change the speed.

4QT

The 4QT (Four Quadrant Transducer), see Figure 2.5 for a general layout, is a full hybrid that optimizes the torque control of the combustion engine by electric rather than by mechanical means. A special electric machine

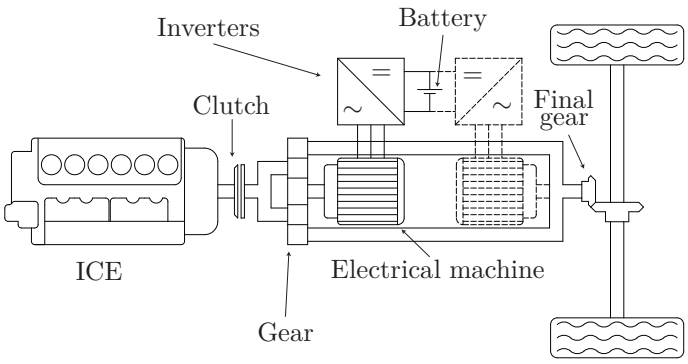

Figure 2.4: *Parallel Hybrid Electric vehicle.*

has been developed for this propose. The electrical machine is actually two electric machines combined into one unit. In order to access the electrical connections of the inner electric machine a slip ring arrangement is required. Depending on the size of the vehicle different types of the machines have

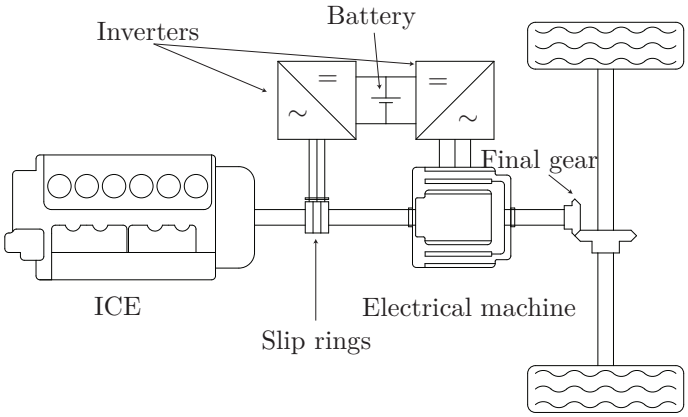

Figure 2.5: *4QT system with the slip rings.*

been studied and developed. A radial-radial machine configuration (Figure 2.5) has been developed for the use in a 12-ton distribution truck [6]. For a smaller vehicle an axial flux machine configuration has been studied and developed [7]. The biggest disadvantage of these machines are the slip rings that require maintenance [1].

2.2.2 Mild Hybrid

A characteristic feature for the mild hybrid, see Figure 2.6 for a general layout, is that the electrical machine is placed between the combustion engine and the gearbox/transmission. The rotor of the electrical machine is connected to the shaft of the combustion engine. Sometimes the rotor actually replaces the flywheel of the combustion engine. As there is no gear between the electrical machine and the combustion engine one can not rotate one without rotating the other. The pure electric mode is therefore very much limited. However, regenerative braking is still possible together with the start an stop capability that can be utilized in urban areas. Sometimes these mild hybrid are also referred as Integrated Starter Generator (ISG) [6]

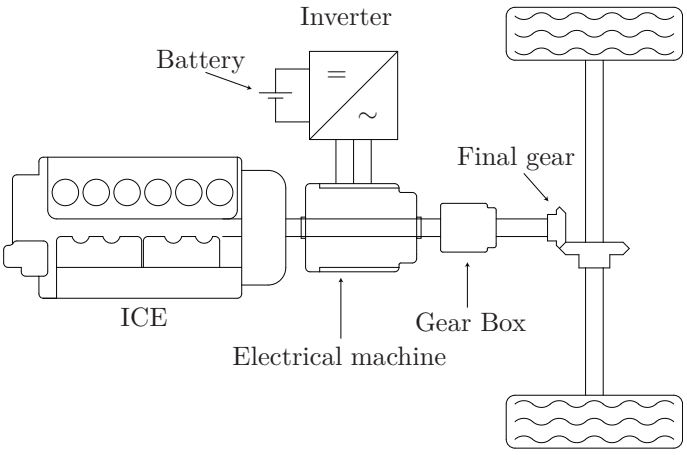

Figure 2.6: *Mild Hybrid (sometimes referred as Integrator Starter Generator).*

2.2.3 Power Assist Hybrid or Micro Hybrid

As previously stated, the different abbreviations attempt to describe to what degree the vehicle is powered by an electric machine compared with the total capacity of the vehicle. Micro, as the name indicates, is the lowest grade of the hybridization and contributes to about 5% to 10% of the fuel economy benefit [8].

Micro hybrids are usually conventional vehicles, powered by either gasoline or diesel engine, where the 12V belt driven starter motor and the alternator have been replaced by a specially designed belt driven ISG [1]. The micro hybrid can not be propelled by the electrical machine alone, instead the benefit of the fuel consumption is gained from the start and stop

capability. It can also, to some extent, collect the regenerative energy during the braking and store that into the energy storage (batteries or super capacitor).

2.2.4 Electric Vehicles

The electric vehicle has been around for a century. Until 1918 the electric vehicle sold reasonably well [9]. However, as the ICE continued to improve their efficiency the number of electric vehicles slowly decreased and by the end of 1933 their numbers were negligible [10]. Unlike the Hybrid Electric Vehicle the Electric Vehicle does not have any energy generating device. Instead, the space is occupied by some energy storage device like batteries. The advantage of the EVs compared to the HEVs is the zero emission and independency from the petroleum based energy supply [11]. The disadvantage is short operating range and long recharging time.

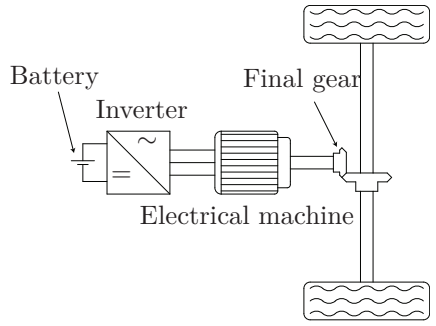

Figure 2.7: *Electric Vehicle (Plug in Hybrid).*

Recently plug-in hybrids have been discussed, see Figure 2.7 for the general layout. The plug-in hybrid does not necessarily only have the electric energy storage but it can also be equipped with ICE and a generator. This is mainly to increase the operating range of the vehicle. However, the main idea is that the vehicle should use the energy from the energy storage device.

2.3 Conclusions

Despite the fact that cars equipped with only ICE will not disappear completely from the market over the next decades, their numbers are expected to diminish. It is because the amount of the oil is limited and the market is looking for more efficient vehicles, only without compromising their per-

formance. In that sense the HEV seems to be a natural step for the further development of these vehicles.

In the nearest future the parallel hybrid is probably the best solution, as this technology requires the minimum adaptation of the infrastructure. However, they will probably be replaced by the series hybrid vehicle where the electrical energy can be generated from different power units. The plug-in hybrids are one solution of the series hybrid vehicle. This solution is also very interesting due to the fact that the infrastructure for recharging of the vehicle is more or less already developed. However, their success is strictly related to the development of the batteries.

Chapter 3

Free Piston Energy Converter (FPEC)

This section will give a short description of the Free Piston Engine concept. It will discuss different layout possibilities and select one which is most suitable for the Free Piston Energy Converter application. Furthermore, some aspects on the advantages and disadvantages of the FPEC concept will be compared to the more conventional solutions available in the market. In addition a short description of similar projects around the world will be given together with a brief discussion of different types of electrical machines that have been investigated.

3.1 Free Piston Engine

The free piston engine has existed for several decades. In fact the very first internal combustion engine was of the free piston type, operating on a two stroke cycle [12]. The engine that worked on gunpowder was built by a Dutch physicist Christian Huygens in 1673.

Modern free piston engines are often accredited to Pescara and his patent from 1928 [13]. The patent was applied for a single piston gas compressor with spark ignition. Later on, he developed different types of machines both spark ignited and compression ignited.

The free piston engines were developed by GM and Ford to be used as gasifiers in cars propelled by gas turbines. However, they never reached a commercial stage and ended up only as prototypes.

3.1.1 Different Concepts

Regardless of the application, the free piston engine is composed of three fundamental components: a combustion chamber, a rebounding device and a load [5] as illustrated in Figure 3.1. The combustion chamber, produces a force acting on the cylinder head, the rebounding device acts as an energy

storage i.e. a spring, while the load is an energy consuming device. All these parts are merged into one unit by a free piston.

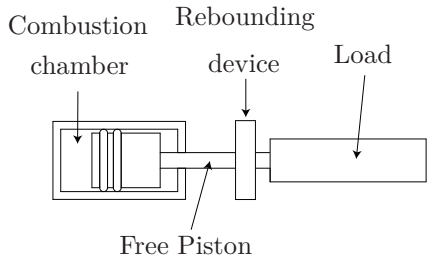

Figure 3.1: *Fundamental components of a free piston device.*

The free piston engine can be arranged in different ways. They are usually classified according the layout of the piston arrangement: single-piston, dual-piston and opposed-piston. Figure 3.2 gives a schematic view of the different free piston layouts. All of them have certain strengths an weaknesses. However, the most suitable arrangement for the FPEC application is the dual-piston layout [14]. The advantage of this layout compared to the other two is that only one linear machine is required, and it allows two power bursts for one complete mechanical cycle. Furthermore, it will result in a more compact solution in comparison with the other two.

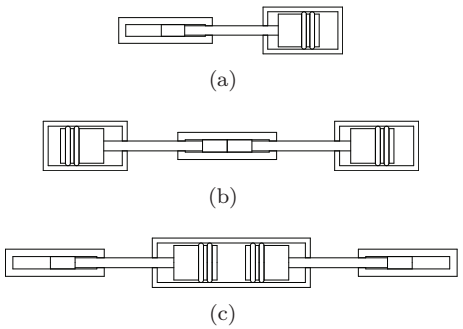

Figure 3.2: *Schematic view of different free piston engine layouts, 3.2(a) One piston, 3.2(b) Dual piston 3.2(c) Opposed piston layout.*

3.2 Free Piston Energy Converter (FPEC)

The FPEC is of dual-piston layout with a linear electrical machine, which is one of the key components in the system. The rebounding device creates an alternating compression in the cylinders where the linear electrical machine serves as a load. A part of the kinetic energy of the piston is converted into electrical energy by the electrical machine. A schematic view of the FPEC is shown in Figure 3.3.

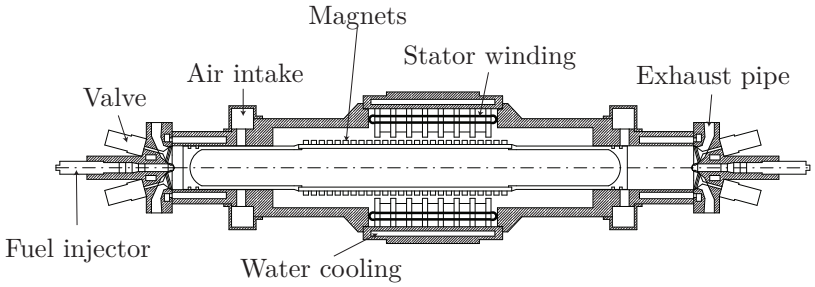

Figure 3.3: *Schematic view of the Free Piston Energy Converter (FPEC).*

3.2.1 Integrated design

There are several advantages with the FPEC compared to the conventional combustion-engine-rotating electrical machine configuration. One of the most evident advantages is probably the total size, as the electrical machine is integrated into the FPEC. Furthermore, the system becomes more robust owing to its mechanical simplicity. Due to the absence of the crankshaft the system will have less friction, less wear and also it will require less lubrication. A big potential of the system is the possibility of modular design. This in the end will result in a fewer standard components, higher reliability and lower price.

3.2.2 Electrical machine

In [14] different types of electrical machines have been investigated in order to find the most suitable one that could meet the tough requirements.

The machines have been compared taking into consideration different aspects both with regard to mechanical stability, maintenance and force production. The Achilles heel of the DC machine is the brushes that requires maintenance. From the mechanical stability and robustness point of view, the switch reluctance and the asynchronous machines are to be

preferred. However, they were not able to meet the specific weight requirement, especially the requirement on the mover mass.

It has been concluded that the only type of the machine that could meet the required weight on the mover, was the Permanent Magnet (PM) machine. Furthermore, the best candidate among these, to meet the overall requirements, was the Transverse Flux Machine (TFM).

3.2.3 Mechanical losses

The free piston engine does not contain a crankshaft and it will move in correspondence to the forces acting on the piston. The crankshaft related losses are about 20% of the overall friction losses in a conventional ICE [14]. Thus, by omitting the crankshaft the efficiency of the free piston engine is also increased. Another benefit related with the removal of the crankshaft is the lower weight of the moving parts.

3.2.4 Dynamics

The dynamics of the FPEC have been studied in details in [5], and to some extent in [14, 15]. In a conventional crank engine the dynamics of the piston is more or less determined by the constant rotational speed of the crankshaft. The compression ratio in the cylinder is predetermined by the length of the crankshaft and thereby the cylinders top position. In order to minimize pulsations the flywheel is attached to the shaft.

In the free piston on the other hand the position of the piston is solely controlled by the electrical machine and the pressure in the opposite cylinders. This gives a wider dynamic range of the engine behavior. The FPEC can respond more rapidly to the transient demands as the acceleration of the piston can be almost 9 times higher compared to the crank engines. Due to the faster response the machine can be started within 1 to 2 strokes only.

The power from the FPEC will pulsate with the reciprocating motion of the piston. In order to even out the power an energy storage device such as a battery or a super capacitor can be used. This can be compared to the flywheel in the crankshaft engines.

3.2.5 Combustion related benefits

Conventional vehicles are operating either with spark ignition or compression combustion. A car running on gasoline is usually spark ignited where the fuel is mixed together with the air before it is injected into the cylinder. A car running on diesel is usually ignited by the compression itself. The air alone is injected and compressed to high temperatures before the fuel is injected. As the fuel mixes with air it ignites spontaneously.

In both the techniques described above the combustion process occurs at high temperature and generates a large amount of NOx gases as a result. In order to reduce the NOx emissions, new combustion engines using the Homogenous Compression Combustion Ignition (HCCI) concept are currently under development by several companies. In most HCCI designs the high usage of EGR (Exhaust Gas Recirculation) has the tendency to lower combustion temperatures below the temperature where NOx gases are produced. Meanwhile, the efficiency of the combustion engine is still kept at a high level. This combustion technique together with the variable compression ratio of the FPEC makes a perfect combination.

In HCCI the ignition of the combustion takes place like in diesel combustion engines as a result of an application of high pressure. Unlike in the diesel combustion engines the fuel in HCCI is injected relatively early in the stroke. The fuel is then mixed with air during the compression to a nearly homogenous mixture. The combustion process starts then throughout the mixture almost simultaneously when the right pressure and temperature are reached.

The FPEC with HCCI offers a higher efficiency alternative compared to the spark-ignited machines and a lower NOx emission alternative compared to the conventional compression-ignited machines.

3.3 Challenges and application

One of the biggest challenges in the FPEC concept is the control of the unit. Although the absence of a crankshaft offers many advantages it complicates the control system considerably. The system itself is unstable and there are several possible failure scenarios.

Controlling the piston by the electrical machine only, is really a question of the size of the machine together with the electrical energy storage [16]. In order to increase the frequency of the piston the weight of the piston is critical and therefore it has to be kept as low as possible. On the other hand, the rating of the electrical machine is to some extent dependant on the weight of the translator, where the increased weight of the magnets increases the rating of the machine. As can be noted, the first requirement is in contradiction to the second. Therefore, in an optimal design the electrical machine can only partially control the velocity of the piston.

By removing the crankshaft the possibility of a simple control system is also dismissed. Controlling the position of the piston and the position of the valves has to be done independently. Today, many car manufactures are focusing their research on removing the crankshaft dependency of the valves which will increase the efficiency of the ICE. Thus the independent control of the valves does not necessarily have to be a big problem or a disadvantage.

3.3.1 Possible Applications

The FPEC is mainly intended to be used in a hybrid vehicle application. Because it has no rotating part all energy from the fuel is converted to electric energy before it reaches the wheels. It is therefore mostly suitable for the SHEV architecture, which was described in the previous chapter.

Another possible solution is the usage of the FPEC concept as an auxiliary power unit, like for example in boats or trucks to provide electrical energy, when the primary power unit is shut down. Its modularity and compactness makes it highly suitable for such an application.

Further, the FPEC unit can also serve as a stand-alone generator. Due to its lower NOx emissions and high overall efficiency it could be an alternative environmentally friendly solution to today's more conventional stand alone generators. Furthermore, the FPEC unit does not need to be optimized for one type of fuel, which offers the possibility for use of other types of fuels as well. This makes it ideal for farmers who has access to different type of fuels that can be produced locally, such as rapseed-diesel and methane gas. Figure 3.4 shows the prototype unit of the FPEC concept.

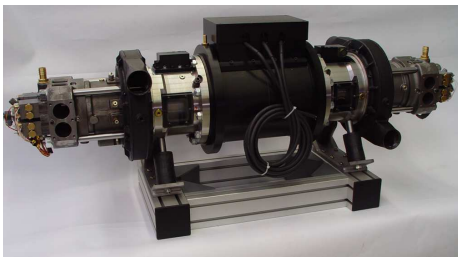

Figure 3.4: *The prototype of the FPEC concept.*

3.4 Similar projects

Similar projects are ongoing around the world. West Virginia university has made a study on what is referred to as a linear engine-alternator. Two prototypes have been built where one of them is shown in Figure 3.5.

According to the author's knowledge, very little has been published on the electrical machine. In [17] the basic principle of the linear electrical machine is described. The electrical machine is built around standard magnets or magnets that were available at the university. Due to the limited budget expensive custom-made magnets have not been used. An output of 2.8 kW with a translator mass of 2.8 kg with diesel combustion has been reported.

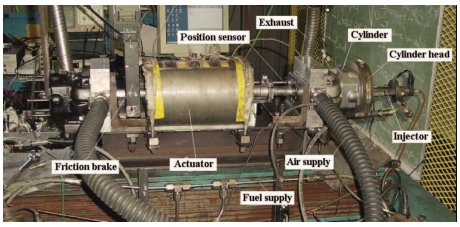

Figure 3.5: *The second-generation linear engine at WVU*

Another system referred to as FP3 or Free Piston Power Pack has been suggested by Pempek Systems Pty. Ltd. in Australia [18], se Figure 3.6.

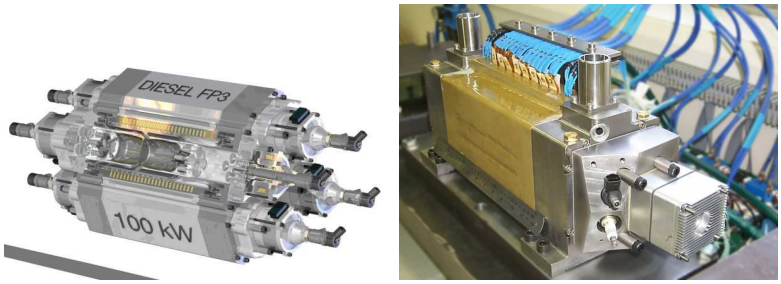

(a) (b)

Figure 3.6: *3.6(a)Cross sectional view of FP3 [19], 3.6(b) Prototype [19].*

The electrical machine is of the buried magnet type design as illustrated in figure 3.7. An interesting detail in the design of the FP3 is that the compressor required for scavenging is integrated into the translator.

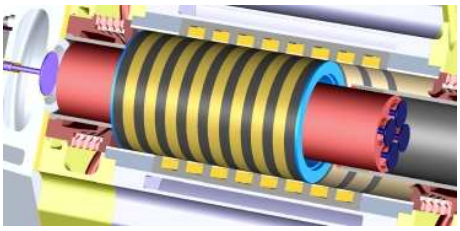

Figure 3.7: *Buried magnet permanent magnet electrical machine in FP3*

A Linear Combustion Engine project at the Czech Technical University in cooperation with the Josef Bozek Research Center of Engine and Automotive Engineering was started in 2000 and has resulted in two different prototypes and several publications [20].

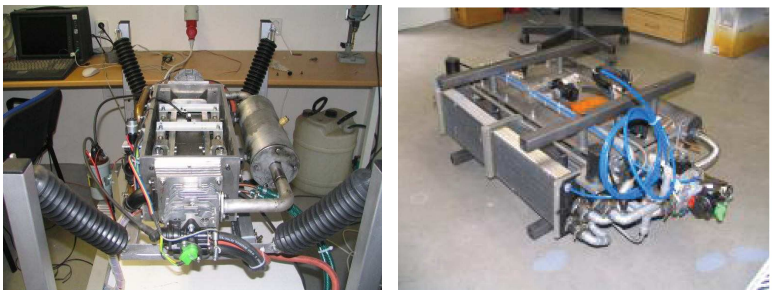

(a) (b)

Figure 3.8: *3.8(a)First prototype of LCE with 1 kW electrical machine, 3.8(b) Second prototype LCE2 with 5kW electrical machine.*

In the first prototype the electrical machine is rated at 1 kW and in the second prototype the rating of the electrical machine was increased. The total output of the first prototype was about 650W while the output of the second prototype is assumed to be in the range of 5kW [20]. Figure 3.8(a) shows the first prototype and Figure 3.8(b) shows the second prototype that were built in the LCE project.

3.5 Conclusions

This section has described some basic characteristics of a Free Piston Engine.

Several similar projects have been ongoing around the world. Although the electrical machine is one of the key components very little is said about it in these projects.

The big challenge of the FPEC concept is the control strategy and ability to control the system as the system is in itself unstable. There are several possible failure scenarios which has to be considered carefully and correct precautions have to be taken in order to avoid a catastrophic damage of the system.

Chapter 4

TFM

This chapter will discuss the Transverse Flux Machine in general. It will describe the most common types of machine configurations, the working principle and some other aspects of the TFM. Furthermore it will discuss the benefits and the drawbacks of the TFM compared with the more conventional design.

4.1 Historical background

The concept of the Transverse Flux Machine is mentioned already in 1895 by W. M. Morday, who applied for the first patent in the same year [21]. However, they were not developed further since no relative advantages were claimed. During the 1970s Prof. E. R. Laithwaite et al. published some papers on a linear TFM for application in railway motored vehicles [22, 23] which gave new life to the concept. However, it was first after a publication by Weh in the middle 80s [24] that the development of different types of transverse flux machines attained a broad attention. Today, several different topologies have been developed and studied in detail. For the rotary transverse flux machine probably the most known works are from RWTH Aachen, TU Braunschweig and the University of Newcastle Upon Tyne.

4.2 TFM characteristics

The main difference between a TFM and a conventional machine is that the force vector produced in a TFM is perpendicular to the magnetic flux lines whereas in a conventional machine this vector is parallel to the magnetic flux lines. TFMs are known for their high power density, where at least in theory, the power rating of the machine can be increased by increasing the number of poles. Assuming iron as ideal and the flux leakage as negligible,

one can explain the secret behind this peculiar feature by calculating the force using the virtual work method.

$$F = \frac{\partial W_m}{\partial z}(\Lambda, z) \tag{4.1}$$

As the leakage flux is considered to be negligible most of the magnetic energy will be stored in the air gap just under the stator teeth. The force is calculated according to Eq. (4.1) where Λ is the total flux linkage and z is the direction of motion. Looking at the equation it can be seen that the force produced in the machine is proportional to the rate of change of energy and inversely proportional to the a small step taken in the direction of motion. Within the framework of the assumptions above, it can be realized that the rate of change of energy will increase as the pole number increases. Here it is further assumed that the length of the machine is the same i.e. the length of the pole becomes shorter with the increasing number of poles. As the rate of change of energy is increased for the same small step the force in the machine will increase.

This is probably not the most intuitive way to explain the peculiar feature of the TFM. Another approach is to look at the induced voltage. In a conventional machine design both the current loading and the magnetic loading are competing for the same space. Thus, the effect of increasing the number of poles in a conventional machine, for example doubling the number of poles, will approximately have the following effect on the voltage:

- Number of turns per coil will be halved then the voltage will be halved $e = n \cdot \frac{d\phi}{dt}$.
- The flux will be halved thus the voltage will be halved once again.
- The number of coils will be doubled and thus the voltage will be doubled.
- The frequency will be doubled as the speed is preserved and the voltage will be doubled once again.

From the analysis above it can be noted that the voltage induced in the winding will be the same as before and thus the VA rating of the machine will not change. In a TFM, however, the current loading and the magnetic loading lie in different planes. The axial length of the pole sets the magnetic loading whereas the lateral width sets the current loading [14]. Increasing the number of poles (decreasing the pole pitch) will not affect the current loading in the machine. Hence, the VA rating of the machine will increase.

Figure 4.1 shows a section of a TFM similar to the Weh configuration. The difference between the machines is that the number of poles in the lower machine is doubled compared to the upper one. As can be noted the pole pitch has been reduced to half of the previous value. The length of

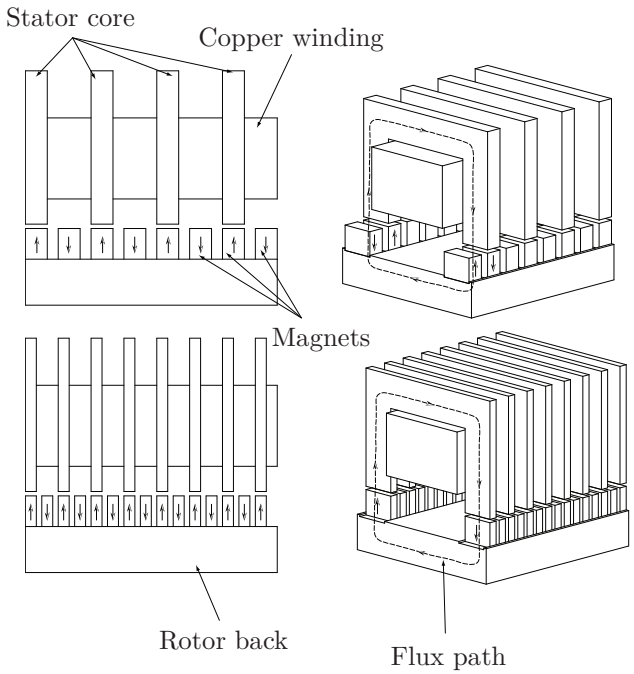

Figure 4.1: *Increasing VA by increasing of the pole number in the machine.*

stator stack as well as the length of the magnets is also half of the previous value. This clearly shows that the magnetic loading in the machine has not changed. The amount of the flux that encircles the winding is still the same, while the current loading is maintained. However, the rate of change of the flux is doubled which results in the doubling the induced EMF. Thus, decreasing the pole pitch in the machine by half, for the same amount of iron, copper and current the VA rating in the machine can be doubled.

The EMF in a TFM machine can be written according to:

$$EMF = k_f \cdot n \cdot \phi \cdot \frac{v}{2 \cdot \tau_p} \tag{4.2}$$

where k_f is the waveform factor , n is the number of turns ϕ is the flux encircling the winding, v is the speed of the mover and τ_p is the pole pitch.

4.2.1 Power factor

A common feature shared by many different TFM topologies is the low power factor. Values in the range of 0.35-0.55 are typical [25]. As the rating of the drive inverter is inversely proportional to the power factor the increase of the power rating of the inverter will be substantial. This of

course is a drawback for a TFM. Furthermore, according to [25] the space for the improvement is very limited, and a low working factor is something inherited in the TFM topology.

The problem with the power factor in a TFM is strongly dependent on the leakage flux. In [22] values of about 50% magnet leakage flux and about 70% armature flux leakage have been reported.

This can be explained by looking at the induced voltage equation. In theory, the leakage of the machine is assumed negligible. In practice, however, if the length of the machine is preserved the same, increasing number of poles will reduce the length of the pole. As a consequence of this there will be a higher leakage flux i.e. poor utilization of the magnets. In addition, increasing the number of poles will also increase the operating frequency in the machine and thereby also the magnitude of the reactance.

4.2.2 End windings

An often referred advantage for the rotating TFMs is the absence of an end winding. Thus no extra space is required for these. However, in a conventional TFM only 50% of the winding is active at any particular time. As the winding between two stator stacks is surrounded by air, and not by iron, the cooling of the machine will be aggravated. Furthermore, these parts of the winding contribute to increased weight, leakage and copper losses in the machine and should therefore be treated as end windings [14]. In a linear TFM there is an additional end winding portion, similar to those in a conventional rotating machine, that is required to encircle the stator teeth.

It can also be mentioned the inactive part of the winding that is in air may also cause some braking torque. The leakage flux that encircles the portion of the winding will interact with the flux from the magnets just beneath. The flux orientation from the winding is the same as it is in the stator, however, the flux orientation of the magnets is in the opposite direction compared with the torque/force producing magnets under the stator teeth. Therefore their interaction may cause a braking torque. This is strongly dependent on the ratio of the magnet width to pole pitch. Furthermore, it will depend on the ratio of the width of the stator teeth (in the axial direction) and the pole pitch.

4.3 Different topologies

TFM offers a considerable amount of the different topologies both in terms of stator and rotor configurations. Henneberger et al [26] discusses different type of windings: Gramme-, Drum-, Pole- and Ring-windings. In chase of an optimum design a lot of different topologies have been developed. Some

of them have also been manufactured and tested. Just to mention some, there are the Southampton prototype of two phase rotary machine [27], low leakage linear one phase machine [14], claw pole transverse flux machine [28], three phase rotary machine [26]. The Newcastle prototype utilizes the concentrated flux configuration [29].

The simplest among the TFM configurations is the Surface Mounted Transversal Flux Machine (SMTFM). A layout of a SMTFM is presented in Figure 4.2. This configuration is described by Weh [30]. From Figure 4.2

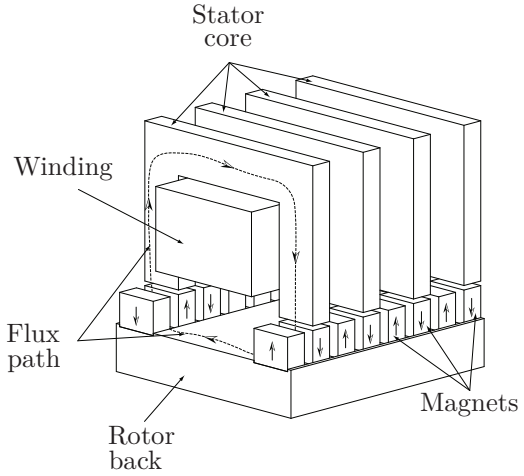

Figure 4.2: *The Surface Mounted Transversal Flux Machine [30]*

it can be seen that this configuration utilizes only every other magnet i.e. 50 % of the available air gap area. In order to have an optimal performance, a major challenge in the design of a TFM is to simultaneously utilize all available magnets. One way to get around this problem is to use both sides of the magnets as illustrated in in Figure 4.3. Another stator with the teeth facing the inactive magnets is placed under the mover in a SMTFM, in this way all magnets are used simultaneously. This configuration is called the Double Sided TFM. The DSTFM is in many ways better compared to the SSTFM. Some advantages are higher VA rating for the same volume and relatively small pole pitches are possible [24]. However, the drawback is that the machine tends to be difficult to construct as the active rotor parts have to be supported in a cantilevered arrangement [22].

There are also other solutions to this problem. Two are shown in Figure 4.4 and and two other (Z-TFM and Low Leakage TFM) will be discussed in more detail later in this chapter.

As can be noted from Figure 4.4 the idea with this type of topology is to modify the stator core, twist it, and thereby guide the flux in such a way that all magnets are utilized at the same time. As can be noted from

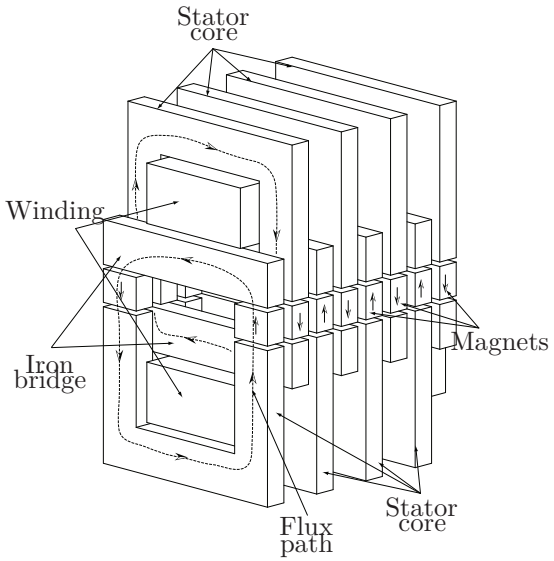

Figure 4.3: *The Surface Mounted Double Side Transversal Flux Machine [30].*

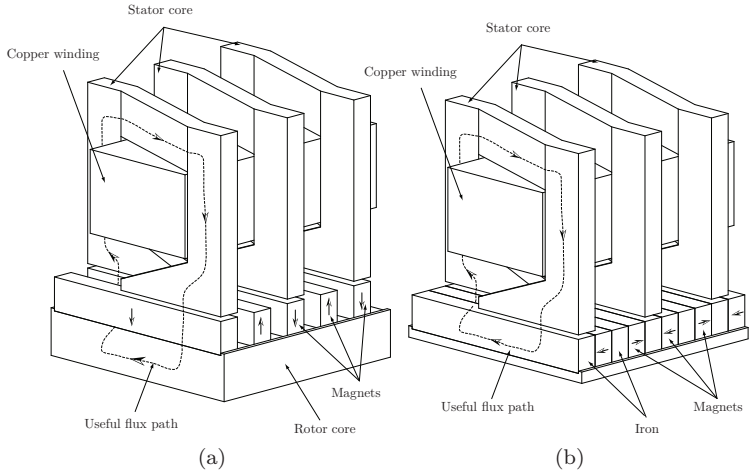

Figure 4.4: *TFM twisted topology a) surface mounted and b) concentrated design.*

the figure, only half of the available pole area faces the stator tooth at the same time. This is done in order to decrease the leakage of the armature flux between the twisted stator teeth. The disadvantage of this is that the stator teeth tips tend to saturate resulting in a lower magnet flux linkage.

The magnets on the rotor/translator can be arranged either as a surface mounted or as a buried magnet design.

Another major challenge in the design of a TFM is the minimization of the leakage flux from the adjacent poles. As can be seen from Figure 4.2 the magnets, which see no iron parts in the stator, will instead attract a leakage flux from the adjacent iron parts. In order to overcome the problem with leakage flux the suggested solution is to insert the so called short circuit bridges which is proposed by Weh at al and Henneberger et al [24, 26]. Henneberger also suggests that these return iron paths should be made in a special triangular shape. This is done to avoid the large stray flux between the U-shaped ('Stator core' see Figure 4.5) and I-shaped stator yokes ('Iron bridge' see Figure 4.5) respectively. It is also stated that the output of the machine can be increased essentially by introduction of the I-shaped return flux path for the inactive magnets. This can be seen in Figure 4.5. However, the presence of bridges does not necessarily imply

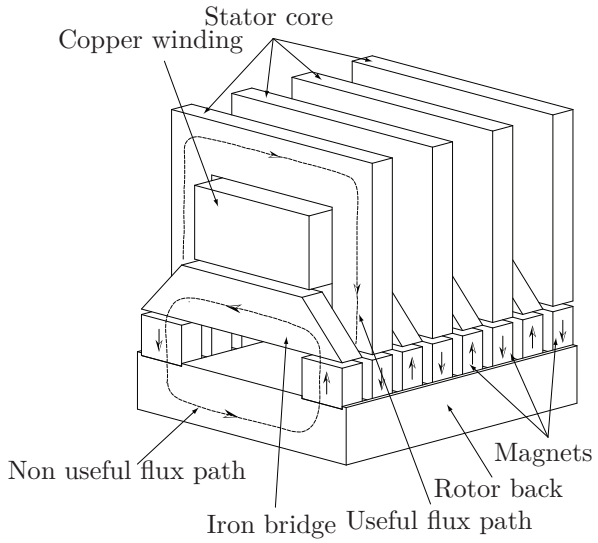

Figure 4.5: *Surface Mounted Transversal Flux Machine with triangular shaped bridges.*

a better machine performance. Although the utilization of magnet flux is improved, by allowing non torque-productive magnet flux to complete its path without linking the stator winding in an adverse manner, the presence of bridges also reduces the area devoted to the copper winding. This means that the machines with bridges need to operate at a higher current density in order to achieve the same performance. Harris et al [31], comparing different machine topologies, realized that the machines with bridges have

to operate at about 18% higher current density compared to machines without bridges.

Another possibility to decrease the leakage flux between the active and inactive poles is to isolate the poles on the mover. This can be seen in Figure 4.6. As can be noted the space between two adjacent poles on the

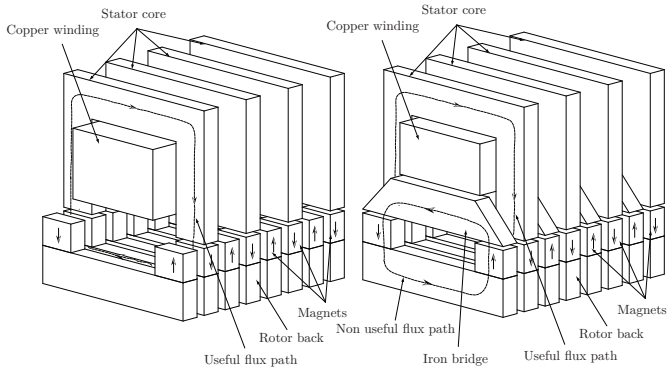

Figure 4.6: *3D-view of isolated poles on the mover, 4.6(a) without bridges and 4.6(b) with bridges.*

mover is not occupied by magnetic material. This arrangement will have two effects. The first, and the prime intention of this, is to prevent a low reluctance path between the adjacent poles so as to minimize the flux escaping from the stator tooth flowing to the magnet in between the stack and then via the mover back to the magnet under the stator tooth. This will affect the useful magnet flux both for the concept with and without the bridges. Furthermore, the configuration with the iron bridges will be more efficient as the adjacent poles will become more isolated. However, the drawback of this configuration is that the mover will be more complicated to build and mechanically more unstable.

Henneberger et al [26] discuss topologies, with weight optimization in mind, where a part of the iron in the mover can be done away with, see Figure 4.7. Looking at the flux path the iron on the mover between the 'positive-' and 'negative oriented' magnets is not required to guide any flux. This part of magnetic material can therefore be replaced with some other nonmagnetic material and thereby reduce the weight of the mover. Another advantage according to [26] are reduced iron losses.

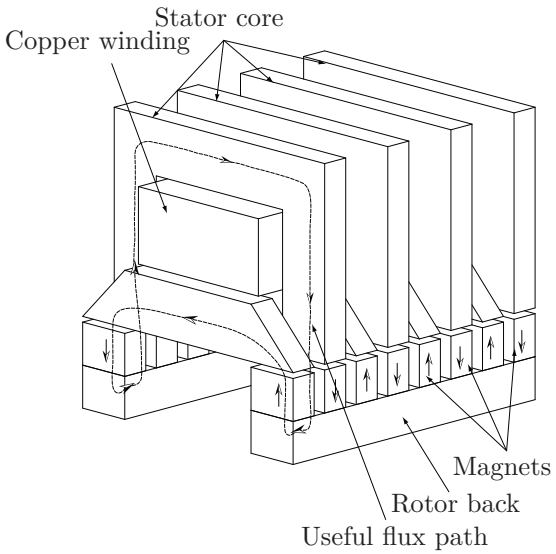

Figure 4.7: *Surface Mounted Transversal Flux Machine with modified mover.*

4.3.1 Z-TFM topology

As mentioned, many different TFM concepts utilize only each second magnet available on the mover. In order to have a better performance of a TFM it is desirable that all magnets contribute to the flux linkage. This will certainly increase the power density of the machine and also introduce some other advantages. One concept that utilizes all magnets simultaneously is the so called Z-TFM. It was named after its inventor Prof. Svante von Zweygbergk, and called the Zweygbergk's TFM (Z-TFM). Figure 4.8 illustrates the Z-TFM concept.

As can be seen from Figure 4.8 all magnets are active and contribute to the flux linkage. This is achieved by introducing a certain complexity in the stator where the flux from intermediate poles, of opposite polarity, is guided in a way that it encircles the winding in the same direction. Theoretically, simultaneous utilization of all magnets will almost double the induced voltage and thereby also the power rating of the machine [32]. Furthermore increased number of the iron parts in the stator will reduce the effective length of the end winding. Other advantages with the topology are reduced magnet flux leakage, improved thermal behavior of the machine and reduced flux fringing.

In an a normal TFM the inactive magnet will face only air (if there is no iron bridge to short circuit the flux path) therefore these magnets will attract the flux from the adjacent poles under the stator teeth. This will decrease the useful flux in the stator back and thereby the induced EMF.

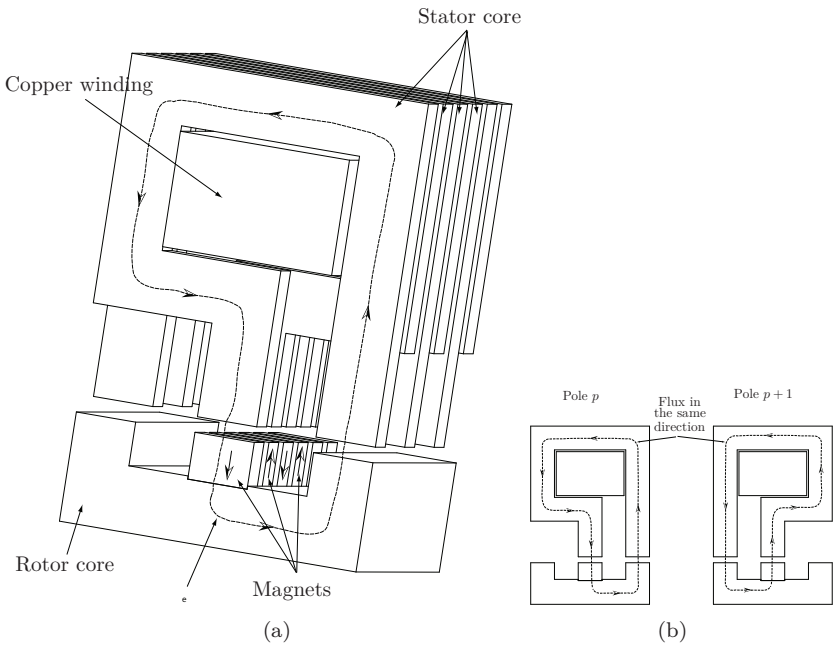

Figure 4.8: *4.8(a) 3D view of Z-TFM ., 4.8(b) Cross sectional view of the Z-TFM for pole p and p+1.*

By introducing an extra iron stack in the stator, the cooling capability of the machine is enhanced. The length of the winding facing the air is lowered and the heat generated in this part of the winding is easily cooled away through the iron parts.

However, all benefits from the introduction of the extra iron stack in the stator looses significance because of the poor force production. In [32] it is reported that the 3D FEM simulated value of the force produced in a 10 kW machine was only about 10 % of the force calculated analytically. A closer investigation showed a very high 3D leakage effect of the armature reaction flux between the adjacent stator stacks. Almost no armature reaction flux entered the air gap which caused a huge loss in the torque production. Insertion of the extra stator stack introduces an overlapping iron area carrying opposite oriented fluxes. The reluctance between the adjacent stator stacks across the overlapping areas was much smaller, due to the short space between the poles, compared to the reluctance in the air gap. Hence, this resulted in high armature flux leakage ($\sim 90\%$) . In order to decrease high pole to pole leakage flux a larger space between the poles is necessary. This on the other hand,for the same machine dimensions, will lower the induced EMF due to the lower magnet area available. It was

concluded in [32] that the Z-TFM will have a larger diameter compared to the ordinary TFM for the same machine rating.

4.3.2 Some Low Leakage topologies studied in the FPEC project

According to the preliminary investigations on the mechanical stiffness preformed by Innas BV [33], the flat design was abounded due to the heavy translator. In order to obtain sufficient stiffness in the translator so that it can manage high forces from the combustion process, necessary laths were added to the flat design. Thus, the mass of the translator increased to unacceptable levels. However, the tubular construction was promising [33] and the flat construction was thus omitted. Figure 4.9 presents a schematic view of the flat TFM design that was investigated. The ideas of the low

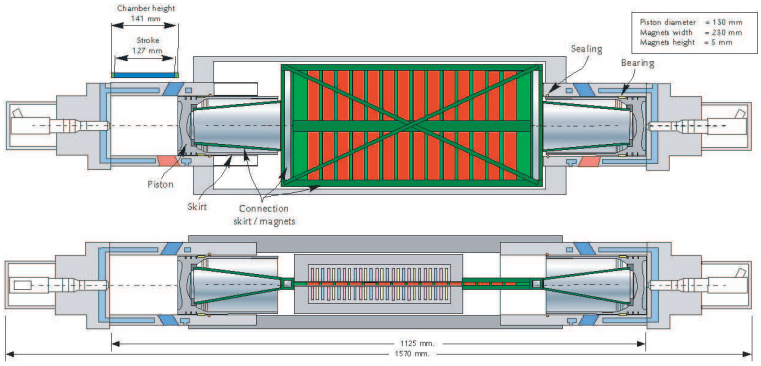

Figure 4.9: *Scheme of the FPEC flat design construction with a short stator.*

leakage flux concentration design were transferred to a more suitable, from the mechanical point of view, tubular construction. Considering the available piston diameters on the market the outer diameter of the translator was chosen. Any other special design piston for the prototype would mean an additional and unnecessary cost for the project. Thus, only available piston diameters were taken into consideration.

Once the diameter was decided the number of parameter variables was reduced. However, it is important to note that the design of the TFM machine was not subordinate to this translator diameter. It was simply selected to minimize the work required on mechanical design and mechanical stiffness of the translator which was ongoing at the time of this decision.

Single phase machine

The single phase machine is represented in Figure 4.10(a). As can be seen from the figure the single phase machine consists of several poles. The pole length is one of the optimization parameters.

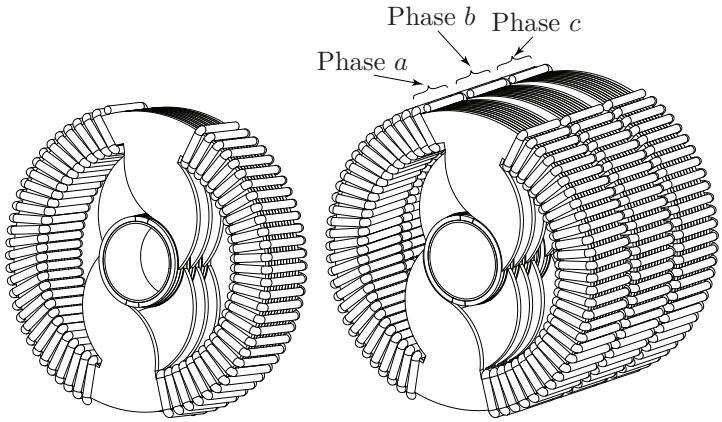

Figure 4.10: *4.10(a) Layout of the single phase machine, 4.10(b)Layout of the three phase machine.*

Complete three phase machine

The total three phase machine is stacked together as three single-phase machines. The layout of the three phase machine is presented in Figure 4.10(b).

As can be understood from the figure the space between two phases needs to be large enough to accommodate two coil ends. This is one drawback of the three phase design as the place available for the active poles in the machine as well as the force developed is reduced. One way to increase the force developed is to increase the number of poles. However, as the total length of the translator is restricted, this will imply shorter length of a pole and may cause some mechanical problems during the manufacturing process.

Flux path for the flux from the magnets

The magnet flux in the air gap originates from four different magnets. Two of the magnets are magnetized in the axial direction and the other two are magnetized in the circumferential direction. The flux path for the flux originating from the circumferentially oriented magnets is shown in Figure

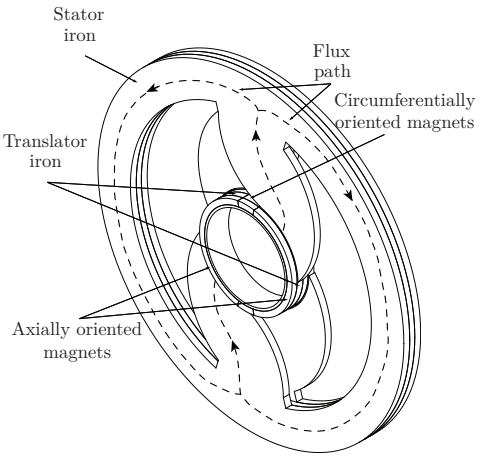

Figure 4.11: *Flux path for the circumferentially oriented magnets.*

4.11. The flux is first gathered in an iron piece on the translator before it enters the air gap and the stator tooth. When the flux from the stator tooth enters the stator back it divides itself in two equal parts. Half of the flux will flow through each side of the machine, going from one side of the stator back to the other. The reluctance that is seen by the flux is the same on both sides. Finally the flux is gathered in the stator tooth on the opposite side and goes via the air gap back to the translator.

The flux path originating from the axially oriented magnets is a bit more complicated. This path is shown in Figure 4.12. As can be seen from Figure 4.12(a) the flux is gathered in the iron piece on the translator before it enters the air gap. The flux then enters the stator tooth and continues to the stator back. In the stator back the flux will flow in the axial direction towards the adjacent pole. From there the flux continues to the opposite side of the machine following two paths as described earlier. The flux will finally enter the stator tooth and the air gap in the neighboring pole and close around itself on the backside of the magnet. Some additional iron losses in the machine will certainly be introduced due to the fact that some of the flux is going in the axial direction. An alternative path for the magnet flux, from the axially oriented magnets, is showed in Figure 4.12(b). In this case the flux will be prevented from flowing in the axial direction. Instead the flux in the stator back will flow around to the other side of the stator in the same pole. Here it may be assumed that the iron part without any tooth is replaced by air. The flux will then be gathered in the stator tooth and via air gap enter the translator iron. Once it is in the translator the flux will flow through the axially oriented magnet on the opposite side.

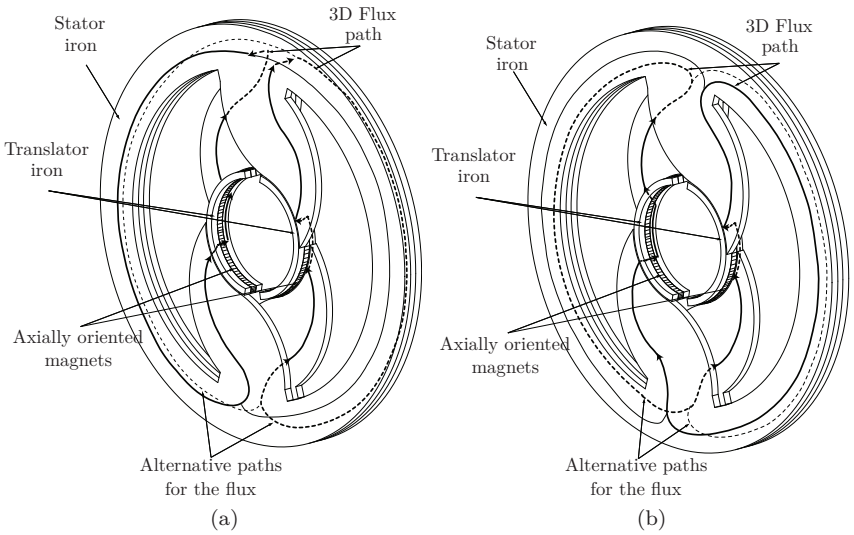

Figure 4.12: *4.12(a) Flux path for the flux originating from the axially oriented magnets, 4.12(b) Alternative flux path for the flux originating from the axially oriented magnets.*

This magnet is magnetized axially in the opposite direction, compared to the originating magnet. The flux goes then via the air gap to the adjacent stator tooth and around in the stator back before it is gathered in the adjacent stator tooth on the opposite side. When the flux enters the air gap and the translator iron on the back side of the originating iron, the flux path is then completed. The reluctance of this path needs however to be compare to the reluctance of the air in the axial direction. Probably some flux would still, even without iron peace, penetrate the iron in the axial direction, which would result in additional iron losses, but now to a lower extent.

According to [14], replacing the iron piece with the air resulted in approximately a 17 % force loss per pole in the machine. Although the iron piece introduces higher iron losses, the loss in the force from its absence is unacceptable.

4.3.3 Simulation results

3D simulation were performed in order to evaluate the preliminary analytical results. The 3D-FEM model is shown in the Figure 4.13. Due to the symmetry in the machine only 2 pole lengths of the machine have been simulated. Simulation results showed high saturation in the stator teeth and the iron pieces on the mover. The results are shown in the Figure 4.14.

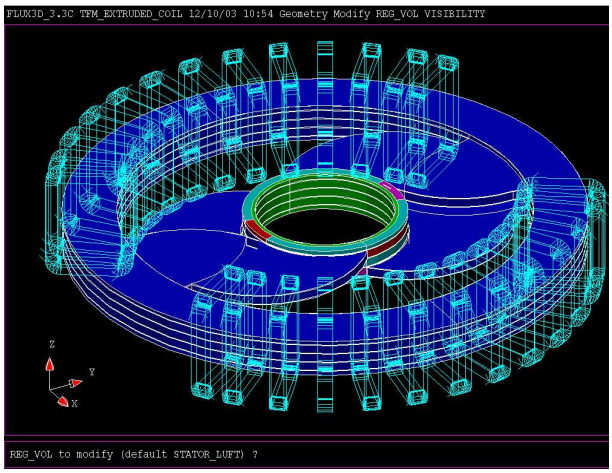

Figure 4.13: *3D simulation model of a low leakage topology TFM with a tubular cross section of the mover.*

In an attempt to avoid problems with the saturation in the stator teeth

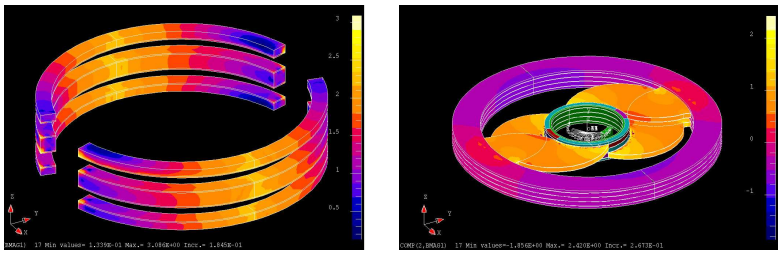

(a) (b)

Figure 4.14: *Saturation in the machine a) in the iron pieces and b) in the stator teeth.*

the stator tooth tip was increased. This is shown in Figure 4.15(a). The reason behind the tooth tip saturation is that the tooth only covers half of the total pole area available. This is done in order to avoid 'tooth to tooth' leakage as is the case in the Z-TFM topology. All the flux originating from the lower half of the pole will try to enter the tooth at the very beginning i.e. in the tooth tip or in other words, where the reluctance path is at its lowest. Avoiding the problem with saturation in the translator was done by varying the length of the iron pieces. As the length of the pole is predefined varying the length of the magnet will automatically result in varying length of the iron pieces. A simple way to avoid saturation is to

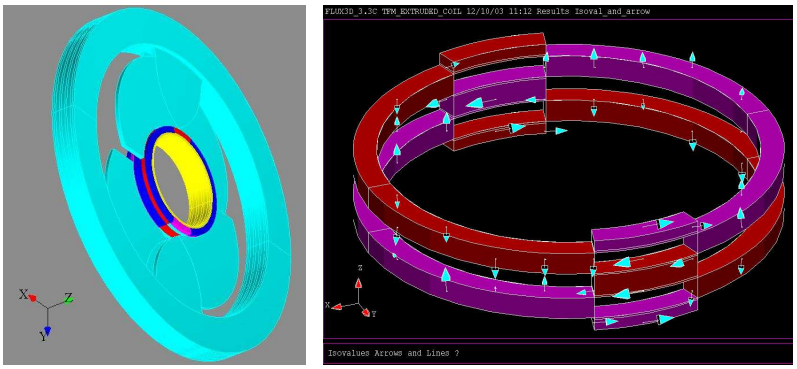

(a) (b)

Figure 4.15: *Concentrated magnet pole on the mover a) iron pieces and b) magnets.*

increase the length of the iron pieces. At the same time, this also results in a lower flux as the volume of the magnetic material will be lower. This indicates that there is an optimum where the problem with saturation of the iron pieces and the available flux from the magnets can be reached. However, the maximum force obtained from the simulations was 1.5 kN at a power factor 0.42. These results were unsatisfactory and a new solution was needed to be investigated.

4.4 Conclusions

The TFM machine is a very interesting concept as the power rating of the machine can be increased by simply increasing the number of poles. However, the high leakage flux and the low power factor that have been reported in different studies seem to be its main drawback.

The problems with the leakage flux were to some extent improved in the low leakage topology. However, some preliminary investigations on the low leakage topology showed unsatisfactory results regarding the force production. Although the prototype machine was design to meet even tougher electromagnetical requirements, it failed on mechanical instability. Once the design ideas were tested on a more mechanically stable tubular cross section design of the translator it could not meet the electromagnetical requirements instead.

In order to meet the requirements, both mechanical and electromagnetical new ideas emerged. The focus with the novel topology that will be presented in the next chapter was put not only on the electromagnetical

requirements but also on the mechanical stability and the simplicity of the manufacturing process.

Chapter 5

Novel Topology

This chapter describes in detail the novel TFM machine design. It discusses different topologies of the novel design. Also some basic analytical expressions are derived.

5.1 Introduction

For a linear electrical machine with a tubular cross section, the concept of the Transverse Flux Machine is highly appropriate. As the flux plane is in the transverse plane in relation to the motion of the mover, iron laminations similar to those in a conventional induction or synchronous machine, can be used. This offers a huge advantage in the manufacturing process in comparison to the more conventional machine design, where the flux plane and the motion of the mover are in the same direction in relation to each other. This implies that the lamination of stator core has to be in the same plane as well, if the iron losses should be kept to a minimum. As it is difficult to laminate the iron across the whole surface of a circle, usually the stator is made up of small segments as illustrated in Figure 5.1. The number of iron laminations will then become very large which will increase the manufacturing cost.

Another disadvantage that comes with the segmentation of the stator is that the area available for the flux in the stator back gets smaller. The stator must then have a large diameter to compensate for this loss in area i.e. the thickness of the stator back has to be increased.

5.2 General description

Figure 5.2 below shows cross-sectional and axial views of the novel TFM, respectively. Figure 5.2(a) shows a cut in the radial direction which is perpendicular i.e in the transverse plane to the motion of the mover. Figure

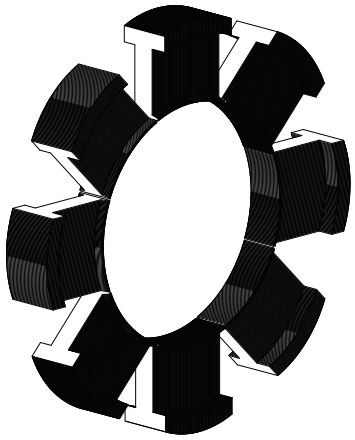

Figure 5.1: *An example of iron lamination of a conventional machine design with a tubular cross section.*

5.2(b) shows the upper half of two lamination stacks. As can be seen in

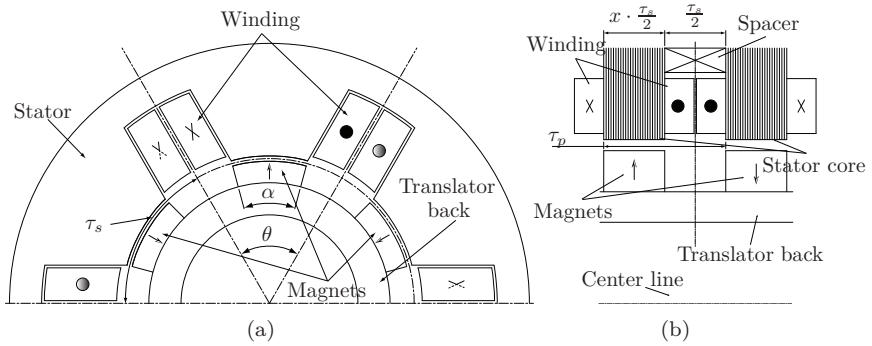

Figure 5.2: *5.2(a) Cross-sectional view,5.2(b) Axial view of the novel TFM .*

Figure 5.2(b) above, the space between the two stacks is partially filled with the end windings of the two coils belonging to e.g. phase 'a' together with a spacer, which helps to keep the distance between the stacks. Also shown in the figure are the placement of a concentrated coil belonging to phase 'a' and wound around a tooth of a lamination stack of length $x \cdot \frac{\tau_s}{2}$. The permanent magnets in the tubular mover are assumed to be of the same length as the lamination stack and of the same width as the width of the tooth, which in this analysis is assumed to be $\frac{\tau_s}{2}$. The slot width and the distance between the stacks is also $\frac{\tau_s}{2}$.

5.2.1 Calculation of the force density for the novel design

To simplify the analysis, the slot width is assumed to be equal to the tooth width which is $\frac{\tau_s}{2}$. The total number of stacks n_{stack} is then given by the following equation

$$n_{stack} = \frac{\ell_s}{(x+1)\cdot\frac{\tau_s}{2}} \tag{5.1}$$

where ℓ_s is the length of the stator and x is a percentage of the total distance between the stacks. The induced voltage in one phase can be written as

$$e = n\cdot\frac{\mathrm{d}\phi}{\mathrm{d}t} \tag{5.2}$$

Further analysis will be performed for different values of x. This value can be chosen freely and as will be evident it influences the operating frequency of the machine.

For $x \geq 1$

Only the fundamental flux density in the air gap is considered. The flux seen by the winding and as a function of the translator position can be written according to following equation

$$\phi(z) = \hat{\phi}\cdot\cos\left(\frac{2\cdot\pi}{(x+1)\cdot\frac{\tau_s}{2}\cdot 2}\cdot z\right) \tag{5.3}$$

where z is the the translator position in the axial direction.

The peak flux occurs when the magnets are positioned just under the stator teeth. The peak flux density can be calculated by the following equation

$$\hat{\phi} = \frac{2}{\pi}\cdot\hat{B}_\delta\cdot\frac{\tau_s}{2}\cdot\left[(x+1)\cdot\frac{\tau_s}{2}\right] \tag{5.4}$$

The voltage induced in one stator tooth of one stator stack can be calculated using Eq. (5.2).

$$E_{tooth} = n_s\cdot\frac{\mathrm{d}\phi\,(z)}{\mathrm{d}t} = n_s\cdot\frac{\mathrm{d}\phi\,(z)}{\mathrm{d}z}\cdot\frac{\mathrm{d}z}{\mathrm{d}t} \tag{5.5}$$

where n_s is the number of turns in one coil (here it is assumed that there are two coils in one slot) and $\frac{\mathrm{d}z}{\mathrm{d}t} = v$ represents the speed of the translator. Putting Eq. (5.3) and Eq. (5.4) into Eq. (5.5) an expression for the peak value of the voltage in one stator tooth is obtained.

$$\hat{E}_{tooth} = \frac{2\cdot\pi}{(x+1)\cdot\tau_s}\cdot\frac{2}{\pi}\cdot\hat{B}_\delta\cdot\frac{\tau_s}{2}\cdot\left[(x+1)\cdot\frac{\tau_s}{2}\right]\cdot v\cdot n_s \tag{5.6}$$

After some modification Eq. (5.6) above can be simplified to following

$$E_{tooth} = \frac{1}{\sqrt{2}} \cdot \hat{B}_{\delta} \cdot \tau_s \cdot v \cdot n_s \tag{5.7}$$

The total voltage in one phase is the sum of all the tooth voltages in the machine and is given by the following equation

$$E_{phase} = n_{stack} \cdot E_{tooth} \cdot \frac{q_s}{3} \tag{5.8}$$

where q_s represents the number of slots in the machine.

Inserting Eq. (5.1) and Eq. (5.7) into Eq. (5.8) and after some modification the final equation for the phase voltage in one phase is given by

$$E_{phase} = \frac{\sqrt{2} \cdot \ell_s}{x+1} \cdot \hat{B}_{\delta} \cdot \frac{q_s}{3} \cdot v \cdot n_s \tag{5.9}$$

From Eq. (5.9) above it can be noted that the voltage in one phase of the machine is directly proportional to the length of the machine, peak flux density and the number of slots. The length of the machine will automatically result in more flux linking the winding. This is also valid for the peak flux density as higher the value of flux density the higher will be the value of the flux linking the winding. Furthermore, the induced voltage is also proportional to the number of slots which in fact means that the number of coils increases. However, as the area available for the copper does not change, an increase in number of coils implies a reduced number of turns in each coil. Therefore, the total number of turns in one phase as well as the phase voltage induced, will not be affected.

It can also be noted that the induced voltage is inversely proportional to the value of the variable x. If x increases the flux linking the winding will be higher due to the increased area of the magnet. However, due to the constant speed of the translator, it will result in reduced frequency and thereby also the induced voltage.

For further analysis it is important to define the current loading. It is a physical description of how much current there exist per unit length. In a conventional machine design this is given as the total current in a slot divided by the length of the slot pitch in the air gap [34].

$$S_{\delta} = \frac{n_{slot} \cdot I_{phase}}{\tau_s} \tag{5.10}$$

For the transverse flux machine this can be derived in a similar way. Figure 5.3 shows the axial cross section of the machine for the value of $x \geq 1$.

If the principal of determining the current loading is applied to the TFM the value of the current should be integrated in the axial direction

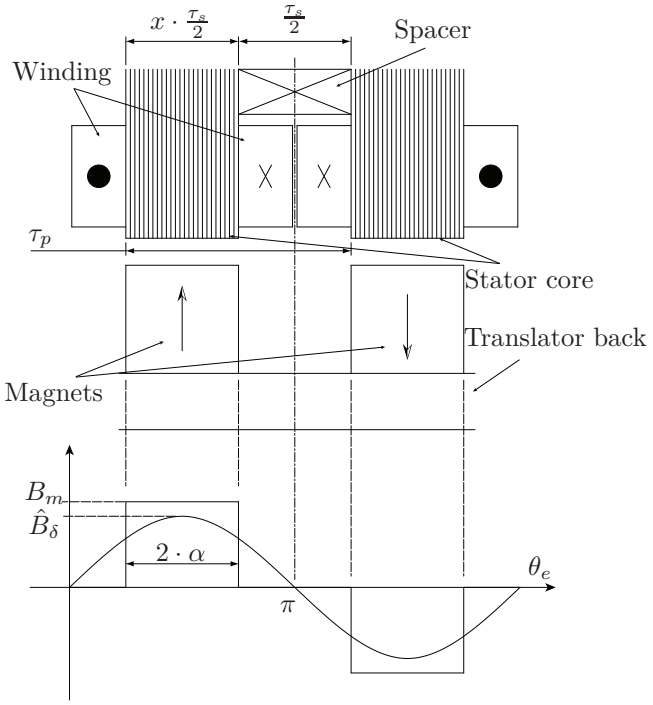

Figure 5.3: *Axial view of the novel TFM for* $x \geq 1$.

and divided by a certain length. Looking at Figure 5.3 it can be noted that the total current integrated between the two stator stacks will be $2 \cdot n_s \cdot I_{phase}$. This value should then be divided by the the length of one pole pitch. The value of the current is valid for $q_s = 3$. However if the number of slots increases then the total current integrated within one pole pitch should be modified in accordance. The final equation for the current loading is then given by the following equation.

$$S_\delta = \frac{2 \cdot n_s \cdot I_{phase}}{(x+1) \cdot \frac{\tau_s}{2}} \cdot \frac{q_s}{3} = \frac{4 \cdot n_s \cdot I_{phase}}{(x+1) \cdot \tau_s} \cdot \frac{q_s}{3} \tag{5.11}$$

For $x < 1$

Using x lower than 1 makes it possible to increase the frequency in the machine by inserting an extra magnet. This is shown in Figure 5.4. As can be noted from Figure 5.4, in order to keep the voltage vectors in the same direction, the winding in the machine must be modified. Instead of having currents between the stacks in the same direction, they must be in opposite direction. It can also be noted that the length of the pole pitch

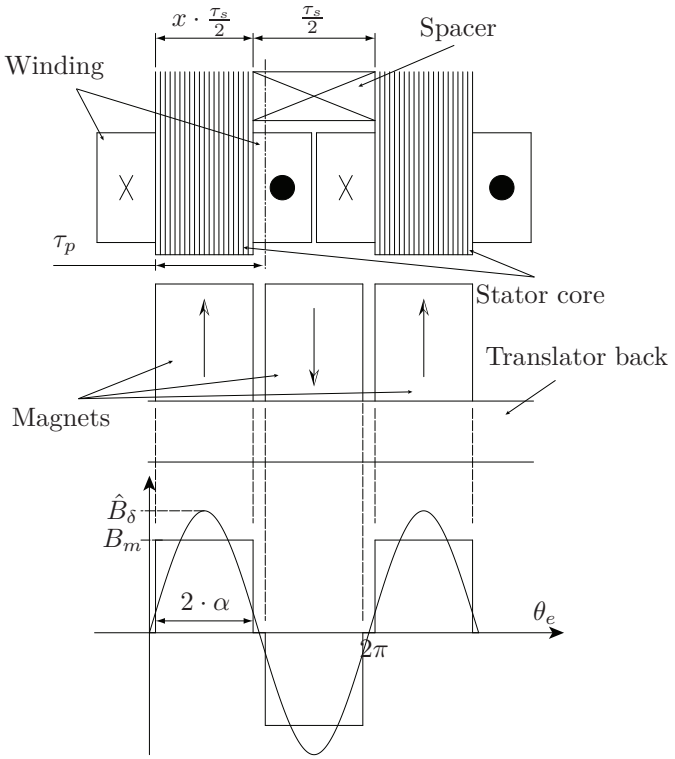

Figure 5.4: *Axial view of the novel TFM for $x < 1$.*

has been reduced, not only because of a lower value of x but also because of the presence of the extra magnet which will reduce the pole pitch to half.

Due to the presence of an extra magnet the distribution of the flux density and the current loading has to be redefined. The equation of the flux as a function of the translator positions is now written

$$\phi(z) = \hat{\phi} \cdot \cos\left(\frac{2 \cdot \pi}{(x+1) \cdot \frac{\tau_s}{2}} \cdot z\right) \tag{5.12}$$

The voltage induced in one stator tooth of one stator stack is then given by

$$\hat{E}_{tooth} = \frac{4 \cdot \pi}{(x+1) \cdot \tau_s} \cdot \frac{2}{\pi} \cdot \hat{B}_\delta \cdot \frac{\tau_s}{2} \cdot \left[(x+1) \cdot \frac{\tau_s}{4}\right] \cdot \frac{\mathrm{d}z}{\mathrm{d}t} \cdot n_s \tag{5.13}$$

As stated previously, $\frac{\mathrm{d}z}{\mathrm{d}t} = v$ represents the speed of the translator. After some elaboration the induced phase voltage can be written as

$$E_{phase} = \frac{\sqrt{2} \cdot \ell_s}{x+1} \cdot \hat{B}_\delta \cdot \frac{q_s}{3} \cdot v \cdot n_s \tag{5.14}$$

From Eq. (5.9) and Eq. (5.14) it can be noticed that the voltage for the case with the extra magnet is derived using the same expression as with the case without. However, for the case when '$x > 1$', $\hat{B}_\delta$ will be much lower than for the case when '$x < 1$' as the pole pitch is halved when an extra magnet is added.

In order to determined the current loading the same procedure as applied previously can be done. However, it is evident that by integrating the total current between two stator stack the result will be 0. As the pole pitch is now only half the value as in the case when '$x > 1$', only one coil needs to be considered. Thus:

$$S_\delta = \frac{n_s \cdot I_{phase}}{(x+1) \cdot \frac{\tau_s}{2} \cdot \frac{1}{2}} \cdot \frac{q_s}{3} = \frac{4 \cdot n_s \cdot I_{phase}}{(x+1) \cdot \tau_s} \cdot \frac{q_s}{3} \tag{5.15}$$

From Eq. (5.11) and Eq. (5.15) it is evident that the current loading in both cases are exactly the same.

Force density

In further analysis only the case with an extra magnet will be considered. Assuming that the induced voltage and the current lies in phase, the power in the machine can be written as

$$P = 3 \cdot E_{phase} \cdot I_{phase} \tag{5.16}$$

From Eq. (5.11) and Eq. (5.15) the current is given by following equation

$$I_{phase} = \frac{3}{q_s} \cdot \frac{\tau_s \cdot (x+1)}{4 \cdot n_s} \cdot S_\delta \tag{5.17}$$

The force density of the machine is given by

$$F_d = \frac{F}{air\ gap\ area} = \frac{P}{v \cdot air\ gap\ area} \tag{5.18}$$

Inserting Eq. (5.16), Eq. (5.14) and Eq. (5.17) into Eq. (5.18), which after some modification can be written as

$$F_d = \frac{3 \cdot \sqrt{2}}{4 \cdot q_s} \cdot \hat{B}_\delta \cdot S_\delta \tag{5.19}$$

The value of the slot pitch is given by following equation

$$\tau_s = \frac{\pi \cdot D_g}{q_s} \tag{5.20}$$

where D_g is the inner diameter of the stator.

From Eq. (5.19) it can be noted that the machines force density is inversely proportional to the number of slots in the machine.

However, increasing the number of slot has a positive effect on the weight of the machine as the stator and the translator backs can be made thinner. The optimum value of q_s has to be a compromise between these performance values. There are also some other aspects that have to be taken into account, like the forces in the radial direction that can cause some vibrations etc.

As explained earlier, the peak flux density in the air gap will be higher in the design with the extra magnet inserted. This becomes more clear looking at the equation below.

$$\hat{B}_\delta = \frac{4}{\pi} \cdot B_m \cdot \sin(\alpha) \tag{5.21}$$

where B_m is the actual flux density in the air gap originating from the magnets.

As can be seen from the Eq. (5.21) the value of the peak flux density of the fundamental wave is proportional to the sinus of the electrical angle α. As this value is much higher for the design with one extra magnet it is also evident that the total flux linking the winding will be higher. This in turn, will result in a higher voltage and higher force production. However, it should be mentioned that the leakage in the machine is not considered during this analysis.

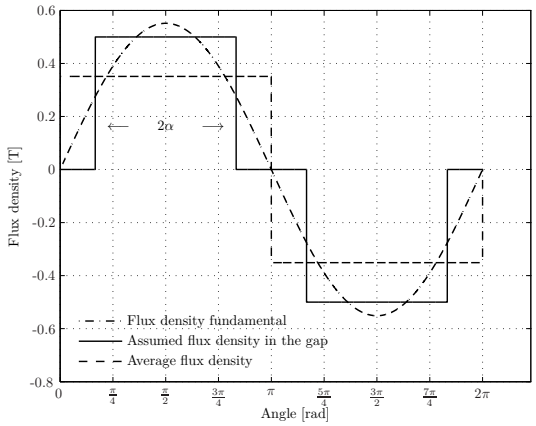

Figure 5.5: *Flux densities in the air gap.*

B_m can be obtained from the following expression

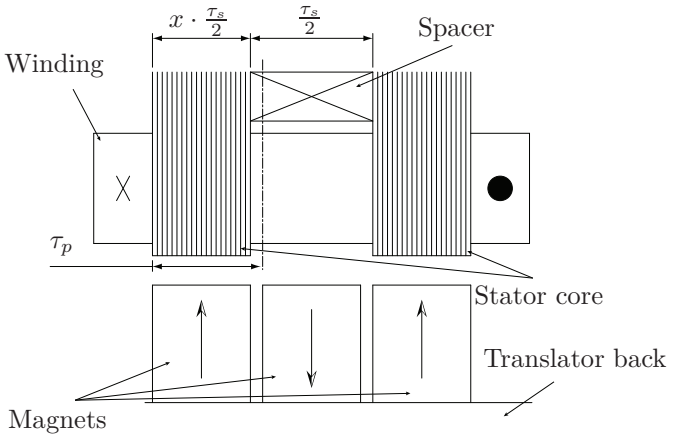

Figure 5.6: *Axial view of the novel TFM for $x < 1$ with global winding.*

$$B_m = B_{rm} \cdot \left[\frac{1}{1 + \mu_{rm} \cdot \frac{\delta_e}{h_m}} \right] \tag{5.22}$$

where B_{rm} is the remanent flux density of the magnets, δ_e is the height of the air gap and h_m is the height of the magnets.

Another possibility offered by the design with an extra magnet is the use of a global winding. Instead of placing the winding around each tooth, the winding can be wound around all the teeth in the direction of motion (axial direction) at the same time, like in a more conventional machine design with concentrated windings. This could offer some more simplicity in the manufacturing process. Figure 5.6 shows a cross sectional view in the axial direction of such a winding. This will be discussed in more details in the following chapters.

Regarding the current loading it should be pointed out that there are also some other definitions available in the literature. In [26] and [35] this definition is given by the following equation

$$\hat{S}_\delta = \sqrt{2} \cdot \frac{n_1 \cdot I_a}{2 \cdot \tau_p} \tag{5.23}$$

where n_1 is the total number of winding in one phase, I_a is the phase current and τ_p is the length of the pole pitch.

Comparing Eq. (5.23) with Eq. (5.15) it can be seen that there is a factor 2 difference between the two equations. According to the authors opinion the value defined in this thesis is a more stringent method to define the current loading.

5.2.2 Winding design

The novel concept offers a great number of different configurations, both in terms of the stator and the mover designs. This is of course a big advantage for a machine designer who can optimize the machine for a certain application with regard to specific power, power density etc. A certain choice of winding configuration in the stator will effect the magnet arrangement on the mover and vice versa. In the novel TFM design, the

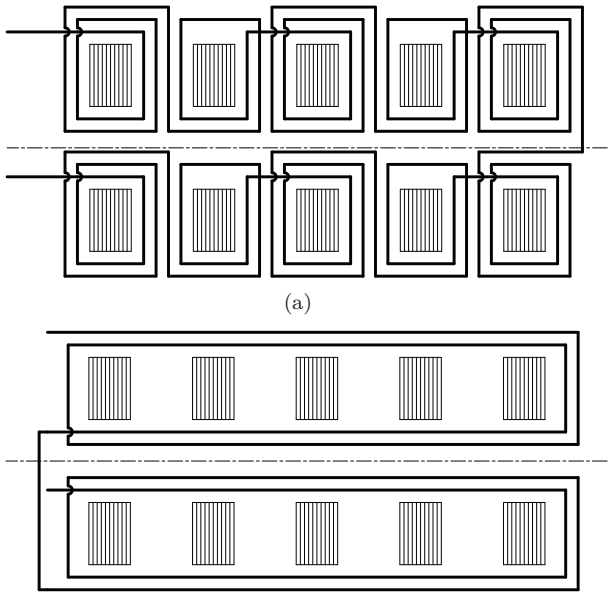

Figure 5.7: *Examples of different winding designs a) local winding design and b) global winding design.*

stator winding can be arranged in different ways. However, there are only two basic winding designs which are denoted as local and global winding respectively, see Figure 5.7. A slight modification of these two winding arrangements is possible which will then have an effect on the magnet arrangement on the mover. The local winding is wound so that the winding encloses each stack tooth separately. The global winding is more or less a concentrated winding design similar to those in the conventional rotary machines. The winding is then wound around the complete length of the machine.

Local winding design

The local winding design offers a lot of different arrangements. The number of actual turns around each stack does not necessarily have to be the same. At the design stage the number of turns around each stack can be chosen freely. One reason for doing this could be that the machine is required to have cooling ducts as in large synchronous machines. Simply by lowering the number of turns around some chosen stack, some space can be released, to enable the introduction of cooling ducts.

This can be done without compromising the functionality or without introducing an asymmetry in the machine. It is also possible to choose different teeth in different phases so as to distribute the cooling effect more evenly along the entire machine. It is however important that the effective number of turns in each phase are the same. In a global winding a cooling duct is inherent in the design so there is no need to consider this at the design stage. However, the space between two stator stack will be occupied by an inactive part of the winding, similar to the end windings in conventional machines. If there is a special need for achieving a better cooling of the machine with a local winding the number of turns around each stack can be varied, see Figure 5.8. The effective number of turns will be given by the following:

$$n_{s_{effective}} = \sum_{i=1}^{\frac{q_s}{3}} \sum_{j=1}^{n_{stack}} n_{ij} \tag{5.24}$$

where n_{ij} represents the number of turns around each stator tooth stack of the machine.

There is a big challenge in the local winding design, as the number of poles can not be chosen freely. The TFM is well known for its high torque/force density. As mentioned, at least in theory, by increasing the number of poles the torque/force can be increased proportionally assuming that the leakage flux in the machine is unchanged. The stator iron and the copper winding do not compete for the same space as in conventional machines. Thus, the number of poles can be chosen freely without affecting the magnetic or electric loading of the machine. Simply by decreasing the length of the pole, a higher number of poles can be achieved for a certain machine length.

However, in the local winding design the number of poles or stator stacks is determined by the electric loading. Once the copper area needed in one slot is determined, the minimum amount of stator stacks is almost automatically given. This is because the same amount of copper has to go around each stator tooth stack. The length of the space between two stator stacks has to be sufficient to allow the end windings of each tooth stack to fit. Actually, the space between two stator stacks will be occupied by two end windings. The conclusion that can be drawn from the discussion above

is that the iron laminations and the copper windings in the local winding design are actually competing for the same space.

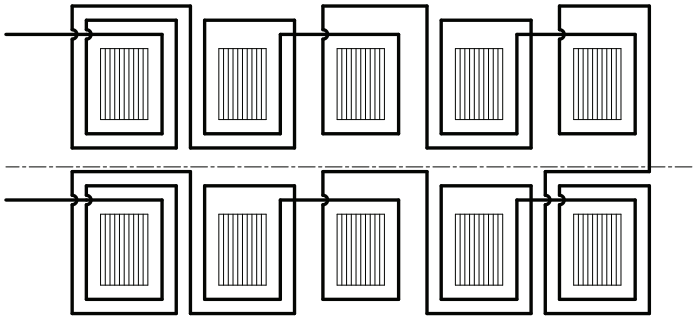

Figure 5.8: *Local winding design with different amount of turns around each tooth.*

Although it may seem that there are not so many other parameters that can be varied in order to regain the peculiar feature of the TFM, there actually are. It is simply achieved by increasing the number of slots in the machine, thereby making it possible to increase the number of poles.

When the number of slots in the machine is increased each slot will contain a lower amount of turns if the electric loading is not to be changed. Due to the lower amount of turns around each stator tooth stack, the space between two stator stacks can be shortened. This means that the number of poles in the machine can be increased for a given length. In theory by increasing the number of slots, the number of poles can also be increased proportionally and thereby also the force produced. Again, the force production is increased assuming that leakage flux is unchanged.

Another positive effect is that the thickness of the stator core back and mover core back will decrease with increasing number of slots, as the width of the magnets decreases correspondingly. This is also possible to achieve with the global winding design. However, in practice like in many other cases, increasing the number of slots has some drawbacks. It will contribute to the complexity of the machine, which in the end will result in higher manufacturing costs.

Many aspects that have been discussed so far have pointed out the disadvantages of the local winding design. The question then arises is there any real advantage with the local winding design? There is however a big advantage as all the magnets on the mover can be used simultaneously. As the winding around each tooth stator stack can be placed in any direction, it is possible to arrange the voltage vectors to act along in the same direction. Thus all magnets will simultaneously contribute to the torque/force production. As described in the previous chapter, usually only half of the

magnets available on the mover are used simultaneously. In order to utilize all magnets at the same time a more complex geometry has to be used. It is either done by rearranging the stator iron in a more complex form as it is done in the Zweygbergk's TFM [36] or in a more complex mover design with a buried magnet design as in the low leakage topology by Arshad [14]. Here, the suggestion is a more complex winding design while both the stator iron and magnet arrangement are kept the same.

Another aspect that can be considered are the copper losses. It is a bit difficult to compare the actual copper losses in the local- and the global winding designs. This will also effect the magnetic loading of the machine. As all magnets can be used at the same time in the local winding design, it is not clear how much copper is needed in order to achieve the same force. If, however, machines with the same length are compared and with the same amount of stacks in the stator, then the length of the copper winding will definitely be longer in the local winding design. Thus the copper losses will also be higher. This is because the total length of the end winding will now be much longer.

Global winding design

The global winding design is more or less a conventional concentrated winding design. For a rotating electrical machine design a TFM has an advantage due to the absence of the end winding. However, in a linear TFM this is actually a drawback compared to the conventional linear electrical machine with a tubular cross section which has negligible end windings.

There are two alternative ways to place the windings; either around each tooth or around each second tooth i.e. one layer and two layer winding respectively, as illustrated in Figure 5.9.

Mostly, concentrated winding designs are used in small Brush Less Direct Current (BLDC) motors, but are sometimes also used in Alternate Current (AC) servo motors. Because of their short end windings and simple structure they are suitable for high volume automated manufacturing process [7]. The concentrated winding is not often used in large machines where the requirements of smooth torque production and low losses are very rigorous [7].

In a conventional machine design with concentrated windings, the number of poles and the number of slots in the machines has to be chosen carefully, otherwise there is a risk that the designed machine might suffer from a very low winding factor or a high torque ripple [37]. In order to overcome the problem with the winding factor a solution with irregular teeth distribution was proposed [38].

The winding factor is the quotient between the vectorial and absolute sums of the fundamental of the MMF of the windings. It can easily be calculated from the phasors for each winding element in the winding.

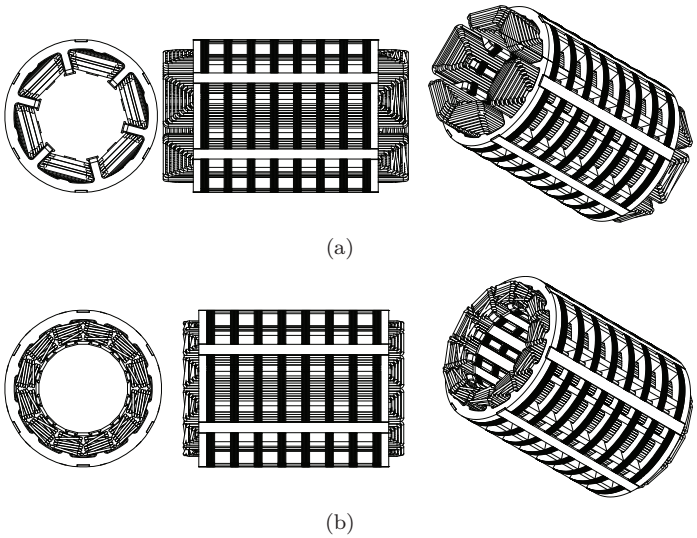

Figure 5.9: *Different types of global winding design a)One layer design b) Two layer design.*

In a TFM, it is difficult to relate the MMF produced by a concentrated winding to that of a concentrated winding in a conventional machines. Thus, the winding factor of the concentrated winding in a TFM is always one as the magnets are normally arranged so that the flux linkage will be at the maximum when the magnets are present just under the teeth i.e. in the d-direction. The concentrated winding design in the novel TFM will therefore be refereed as the global winding design.

From the production point of view the one layer global winding is preferable to the two layer winding design. It is because the number of coils will then be halved.

However, the drawback with the one layer winding is longer end windings. Another drawback is a higher saturation of the tooth in the middle of the winding. This is because the total armature flux will be concentrated to this tooth which will lead to a higher saturation of the tooth and eventually also to loss of force production. This, however, can be avoided to some extent by introducing irregular teeth distribution.

5.3 Mover design

This section will describe some magnet arrangements that are commonly used today in permanent magnet machines.

Buried magnets

The buried magnet design did not turn out to be an appropriate solution for the novel linear TFM. It is because adjacent poles on the translator will short circuit each other and thus almost no flux will enter the stator.

As mentioned, the power rating of the machine can be increased by increasing the number of poles. Keeping the length of the machine constant, increasing the pole number will result in shorter pole length. Here mechanical constraints have been taken into consideration as well. As can be seen

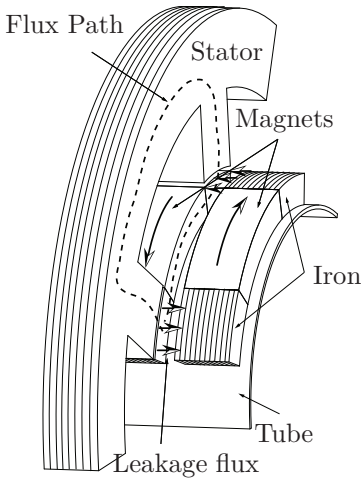

Figure 5.10: *Axial leakage flux for the buried magnet design.*

from Figure 5.10, the space between two adjacent poles is of high importance. Assuming iron as ideal, the ratio between the air gap reluctance and the reluctance of the space between two poles will determine the amount of flux that enters the stator. This ration can be increased by increasing the space between the two poles. However, the active area of the magnet is then decreased, assuming that the length of the machine must be kept constant. Thus, there will also be a certain loss in the thrust force. The buried magnet design is therefore omitted from the further analysis and only surface magnet design will be considered here.

Halbach magnet arrangement

A Halbach magnet array is an attractive solution considering an optimum weight of the translator. It was first introduced by Halbach for use in particle accelerator optical elements and advanced synchrotron light sources [39, 40]. In this geometry, the magnetization vector in the array has both gap normal and gap-tangential periodic components [41].

The idea is that the magnetization vector should rotate as a function of distance along the array so as to maximally aid the desired field distribution. If the vectors are rotated continuously, the field on one side of the array will be zero. The field strength on the other side of the array will therefore be doubled, compared to the sinusoidal variation of purely vertical magnetized magnet [41]. This means that the iron back can be removed and thereby the weight of the mover can be reduced. Different arrangements of Halbach array are shown in Figure 5.11.

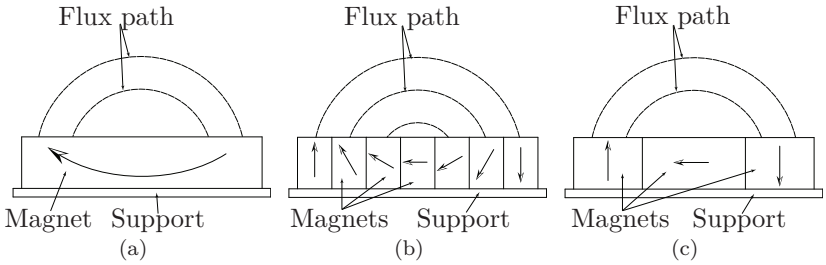

Figure 5.11: *Different arrangements of Halbach array a) ideal Halbach magnetization b) segmented Halbach array c) semi Halbach array.*

Ideally the vectors should rotate continuously as illustrated in Figure 5.11(a). In practice, however, it is not possible to construct such a magnetic material. Furthermore, it is not possible to achieve a magnetization of this material in a such pattern, even if it could be constructed. Instead this is achieved by dividing the magnet into small segments, where each segment is then magnetized in a desired axis as shown in Figure 5.11(b). By proper choice of the block magnetic axes, a close approximation of the ideal case can be achieved.

Usually in order to minimize the cost fewer block of the magnets are used. In [41] it is shown that approximately 90 % of the fundamental field, of the ideal array in which the rotation is continuous, is possible to achieve with a semi Halbach array as illustrated in Figure 5.11(c).

Surface mounted magnets

The surface mounted magnet is the most common way to arrange the magnets on the mover, see Figure 5.12 for a typical layout. The magnetization of the magnets is very simple, thus the price of the magnets can be kept low. In order to have a high flux density in the air gap there is a need for an iron back. Therefore the weight of the translator tends to be somewhat higher compared to the two alternatives above. The thickness of the iron back depends strongly on the number of slots in the machines. In a conventional machine design the thickness of the iron back is reversely proportional to

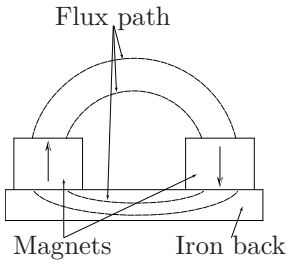

Figure 5.12: *Typical layout of a surface mounted magnet design.*

the number of poles. In a TFM, however, the pole number varies in the transverse plane compared to the flux variation and therefore it will not affect the mover back thickness. In the novel TFM the thickness of the mover back will be reduced by increasing the number of slots. Ideally, the thickness of the mover iron back can be reduced to very small values and the weight of the mover can be kept very low. However, with increased number of slots the space between the magnets in different phases will be smaller and therefore the leakage flux in the machine will increase as well. Another aspect is the mechanical constrain as the size of the magnets will decrease with increasing number of slots and therefore the machine will be more difficult to build.

For the prototype manufactured the number of slots have been maximized to 12.

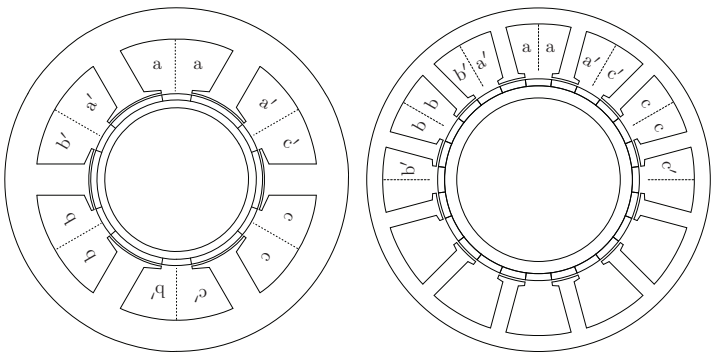

Figure 5.13: *Cross-sectional view of the novel TFM a) $q_s = 6$ and b) $q_s = 12$ slots.*

5.3.1 Three phase design

Several different TFM configurations have been developed so far. However, most of these geometries are basically only a single phase design, which can be transformed into a three phase design with almost no or very low magnetic coupling between the phases [22]. In the novel topology the phase shift, for a three phase design, is achieved by simply displacing the magnets by 120 electrical degrees in the direction of motion, i.e. in the axial direction.

Separate phases

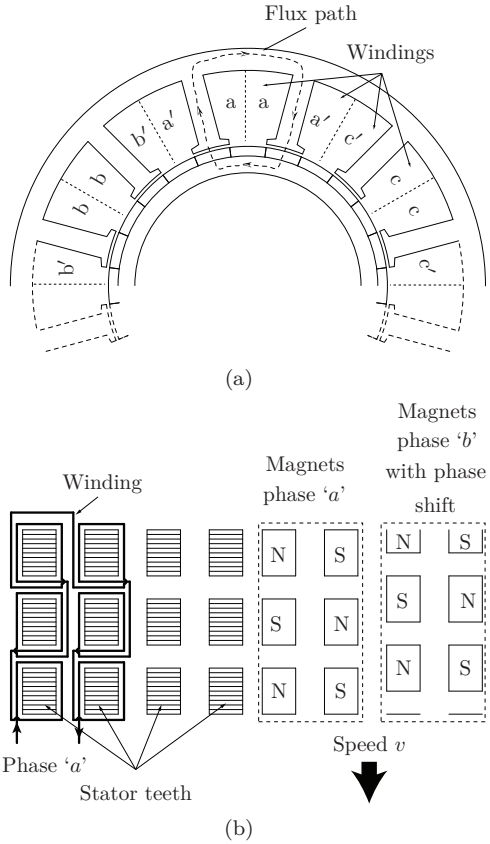

Figure 5.14: *5.14(a) Cross sectional view showing the placement of the windings and the flux path for phase a, 5.14(b) Radial and axial view of the stator coil (local winding) and the placement of the magnets on the mover.*

The simplest design is to keep the flux paths of the three phases separated from each other, as shown in Figure 5.14. The design shown in the figure assures a flux path in the transverse direction at all instances of time. However, the stator and mover yokes will take the complete flux from the stator teeth, thus the core thickness must be at least the width of the tooth. Another alternative is to mix the flux paths of the three phases.

Mix flux paths

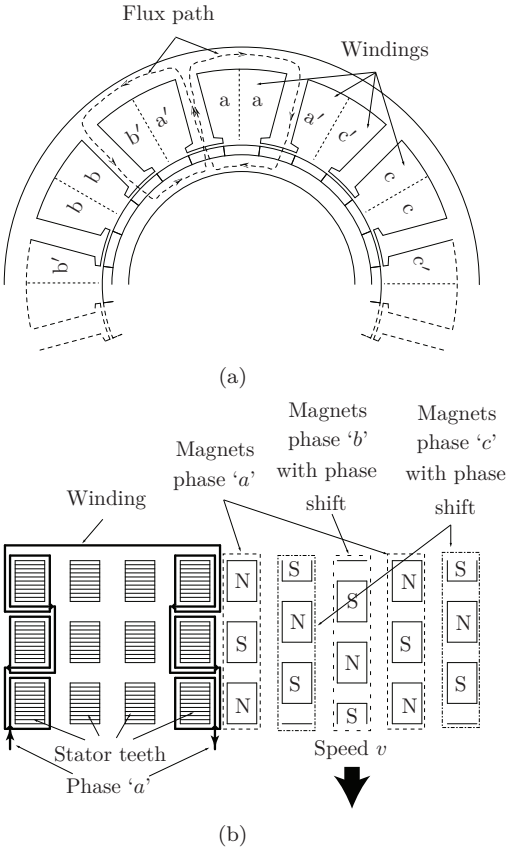

Figure 5.15: *5.15(a) Cross sectional view showing the placement of the windings and the flux path for phase 'a'. 5.15(b) Radial and axial view of the stator coil (local winding) and the placement of the magnets on the mover.*

Another method is to mix the flux paths of the three phases, see Figure 5.15. It is however, important to assure that the total 'N-pole' and 'S-

pole' area 2x3 slots are equal in order to assure that the flux paths can be completed through a low reluctance path through the iron.

The arrangement shown in figure above will probably give a smaller core thickness. There are many possibilities to mix the flux paths.

Chapter 6

Analytical model

This chapter presents an analytical model of the novel TFM. First, a very simple analytical model of the TFM was developed. Not surprising, the results from this model did not agree very well with measurements. Therefore, a new improved model is developed. In this model an attempt to cover the true picture of the actual flux paths in the machine is made.

6.1 Introduction

In an electrical machine there are many geometrical parameters. Most of the parameters can be varied in order to obtain an optimal machine design. However, usually only a few are varied while the rest are kept constant. The constant parameters are either determined by the requirements that the machine has to fulfill or simply by some mechanical tolerances that set the limits.

Table 6.1 represent the FPEC requirements that the electrical machine has to fulfill. As can be seen, the stroke length in the FPEC is set to 127.5 mm. However, only 90% of the stroke length will be used for power generation. This requirement is given as the '*operating length*' of the machine, which indirectly will also have an effect on the translator length.

The magnetic air gap length given in Table 6.1 is the distance between the magnets and the stator teeth. The actual mechanical air gap length will be lower due to the bandaging material.

The nominal and the maximal force in Table 6.1 are determined from efficiency requirements of the combustion process. These forces are defined in different ways for the combustion process and for the electrical machine. The maximal force produced in an electrical machine will only be available for a short period of time, usually about a few seconds, otherwise the damage caused by the heat can be severe. In contrast, the maximal force in the combustion process is where the combustion machine can operate

Table 6.1: *Specifications for the electrical machine*

Parameter	Requirement
Translator outer diameter D_{to}	110 mm
Stroke length ℓ_{stroke}	127.5 mm
Operating length for maximal force	110 mm
Operating length for nominal operation	115 mm
Total length of the stator ℓ_s	<220 mm
Total length of the translator ℓ_t	<330 mm
Air gap length δ	1.25 mm
Nominal force	2.7 kN
Nominal frequency	32 Hz
Nominal average velocity	10.5 $\frac{\text{m}}{\text{s}}$
Maximal operating force	4.0 kN
Maximal frequency	39 Hz
Maximal average velocity	12.2 $\frac{\text{m}}{\text{s}}$
Efficiency	> 90 %
Specific power	>1 $\frac{\text{kW}}{\text{kg}}$
Translator mass	< 6 kg

continuously, however, with a lower efficiency. The nominal force refers to the operation point of the combustion machine where it has the highest efficiency. As a consequence the electrical machine has to be designed for continuous operation at the maximum force of the combustion machine.

6.2 Design procedure

Before an analytical design procedure of an electrical machine can be initiated there is a need for identification and definition of certain machine parameters together with the material constants.

One of the first and one of the most important tasks during a design procedure is the identification of the magnetic circuit and calculation of the magnet height. In this simplified design procedure, prior to the calculation of the magnet height the required flux density in the air gap is defined. The height of the magnets ℓ_m is then given by Eq. (6.1).

$$\ell_m = \frac{\mu_m \cdot \delta_e}{\frac{4}{\pi} \cdot \frac{B_{rm} \cdot \sin(\alpha)}{\hat{B}_\delta} - 1} \tag{6.1}$$

where δ_e is the equivalent air gap length, μ_m is the relative permeability of the magnet and B_{rm}, $\hat{B}_\delta$ and α are as explained previously in section 5.2.1 in Chapter 5. The equivalent air gap length is calculated by adding

another 50% to the actual air gap length i.e. $\delta_e = 1.5 \cdot \delta$. This is done in order to account for the leakage flux in the air gap. This factor can be compared with the Carter factor in conventional machines. However, unlike the Carter factor that is derived from the magnetic flux path in the air gap, this factor may be seen as a qualified guess. As will be shown later the assumption of 50% increase of the air gap was not enough. Hence, the leakage in the machine was underestimated.

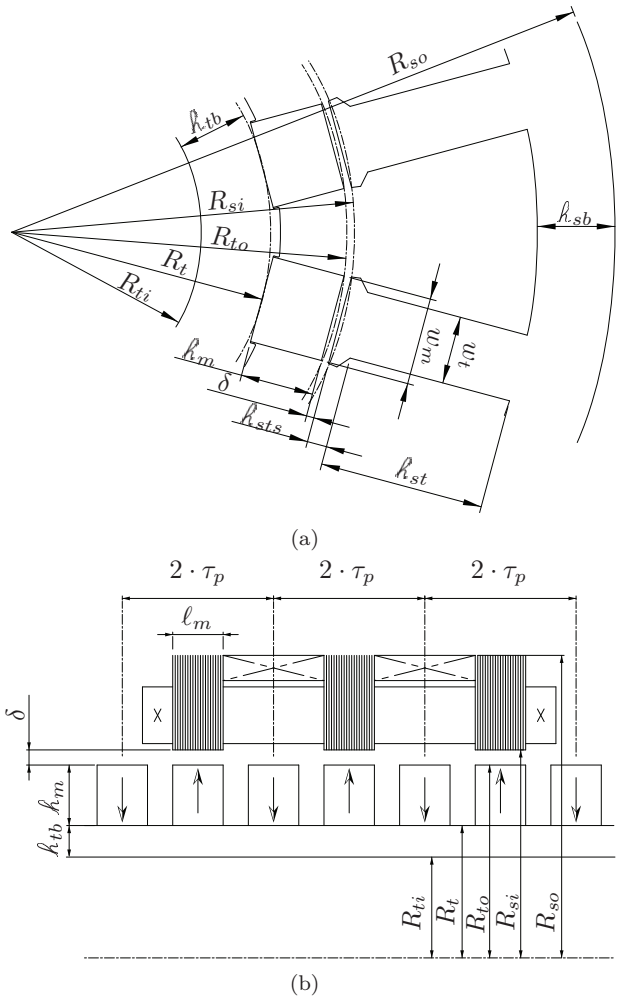

Figure 6.1: *Dimensioning details of the machine.*

The height of the translator back h_{tb} is calculated with the following

equation

$$\hbar_{tb} = \frac{2 \cdot \hat{B}_\delta \cdot D_{to}}{B_{ty} \cdot q_s} \tag{6.2}$$

where D_{to} is the outer diameter of the translator and B_{ty} is the flux density in the translator yoke.

The width of the stator tooth w_t can be written according to the following equation

$$w_t = \frac{2 \cdot \hat{B}_\delta \cdot D_{to}}{B_{st} \cdot q_s} \tag{6.3}$$

where B_{st} is the flux density in the stator tooth.

The height of the stator back h_{sb} can be written according to following equation

$$\hbar_{sb} = \frac{2 \cdot \hat{B}_\delta \cdot D_{to}}{B_{sy} \cdot q_s} \tag{6.4}$$

where B_{sy} is the flux density in the stator yoke.

In order to calculate the current required, the voltage induced in the machine has to be known. The procedure to calculate the voltage was described in section 5.2.1 and is given by Eq. (5.9). The minimum current required is then given by

$$I_{phase} = \frac{P}{3 \cdot E_{phase} \cdot \eta \cdot \cos(\varphi)} \tag{6.5}$$

where the power developed by the machine is $P = F \cdot v$, i.e. force required by the machine multiplied by the average velocity of the translator. The assumed efficiency in the machine is $\eta = 0.9$ and the assumed power factor is $\cos(\varphi) = 0.8$. The value of η and $\cos(\varphi)$ may be seen as initial guesses, which are corrected later once the rest of the design parameters in the machine are determined.

The insulated copper area required by one coil group is given by

$$A_{ins} = \frac{n_s \cdot I_{phase}}{k_{fill} \cdot J} \tag{6.6}$$

Once the width of the tooth and the copper area required are calculated the next step is to calculate the height of the slot. The dashed area 'A', which is shown in Figure 6.2, can be calculated as

$$A = \frac{\alpha_{tooth}}{4} \cdot \hbar_{st}^2 \tag{6.7}$$

The total area of the slot then is

$$A_{slot} = \frac{\theta - \alpha_{tooth}}{2} \cdot \left[\left(R_{scu} + \hbar_{st} \right)^2 - R_{scu}^2 \right] + 2 \cdot \frac{\alpha_{tooth}}{4} \cdot \hbar_{st}^2 \tag{6.8}$$

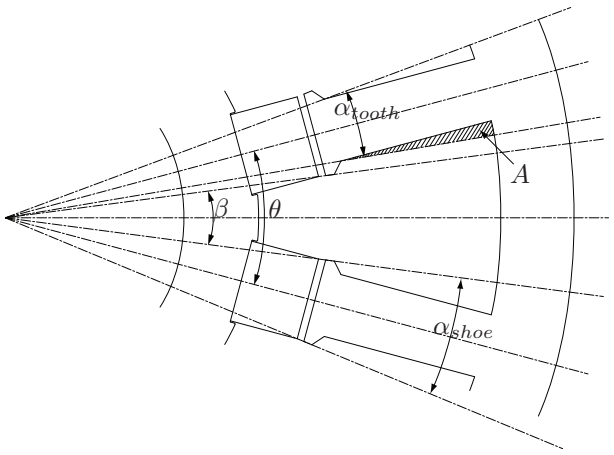

Figure 6.2: *Slot area calculation.*

where R_{scu} is calculated from $R_{scu} = R_{si} + h_{sts} + h_{stst}$, where h_{stst} is the height of the stator-tooth-shoe-tip which was chosen to be half the value of the h_{sts} (height of the stator-tooth-shoe). This value is added in order to account for the thickness of slot insulation material. R_{si} and h_{sts} are defined according to Figure 6.1.

By solving Eq. (6.8), the following expression for the slot height is obtained:

$$h_{st} = \frac{1}{\theta} \cdot \left[R_{scu} \cdot (\alpha_{tooth} - \theta) + \sqrt{R_{scu}^2 \cdot (\theta - \alpha_{tooth}) + 4 \cdot A_{ins} \cdot \theta} \right] \quad (6.9)$$

Here it should be noticed that the insulated copper area A_{ins} occupies only half of the total slot area A_{slot}.

The number of stacks in the machine is given by Eq. (5.1) in the previous chapter. However, this equation is given for a local winding design where the slot pitch τ_s and the pole pitch τ_p are interdependent. Therefore, in order to better suit the global winding design where the values of τ_s and τ_p can be chosen independently Eq. (5.1) should be somewhat modified. Without considering the length of the end winding, the number of stacks is given by

$$n_{stack} = INT \left[\frac{\ell_s + 2 \cdot \tau_p - \ell_m}{2 \cdot \tau_p} \right] \quad (6.10)$$

where ℓ_s and ℓ_m are the length of the machine and the length of the magnet in the axial direction ,respectively, and τ_p is the length of the pole pitch.

The area of a conductor A_{cuc} is as

$$A_{cuc} = \frac{I_{phase}}{J} \tag{6.11}$$

where J is the current density in the conductor. For machines with forced air cooling values in the range of $4 - 6\ \frac{\mathrm{A}}{\mathrm{mm}^2}$ have been reported [14]. However, in water-cooled machines this value can be easily increased to $6 - 8\ \frac{\mathrm{A}}{\mathrm{mm}^2}$. This type of cooling is also used in FPEC.

The radius of the conductor is given by

$$R_{cu} = \sqrt{\frac{A_{cuc}}{\pi}} \tag{6.12}$$

6.3 Electrical Parameters

This section discusses the electrical parameters of the machine. Once the dimensions of the machine are determined the electrical parameters in the machine, such as inductances and resistances, can be calculated.

6.3.1 Inductance

The self inductance in a linear media can be written as [42]:

$$L_{self} = \frac{\Lambda}{I} \tag{6.13}$$

where Λ is the total flux linkage and I is the current in the coil. If there exists a nonlinearity in the material the equation above can be written in a more general form:

$$L_{self} = \frac{d\Lambda}{dI} \tag{6.14}$$

Usually, most electrical machines are designed to operate at the knee of the nonlinear region of the iron material. This enables superposition of the inductances calculated separately for different sections of the machine.

Main inductance

The total inductance in the machine is the sum of the main inductance and the leakage inductance. Furthermore, the leakage inductance can be separated into four different components, as will be explained later.

The main inductance is calculated according to

$$L_{main} = \frac{q_s}{3} \cdot n_{stack} \cdot n_s^2 \cdot \frac{\mu_0 \cdot \mu_{rm} \cdot \ell_m \cdot w_m}{\delta \cdot \mu_{rm} + \hbar_m} \tag{6.15}$$

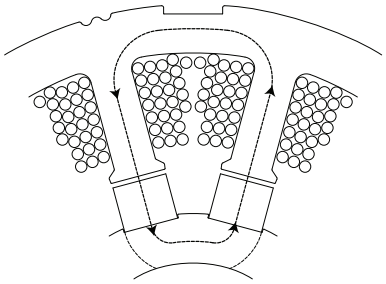

Figure 6.3: *Flux path for the main inductance.*

where μ_0 and μ_{rm} are permeability of the vacuum and relative permeability of the magnet respectively. w_m is the width of the magnet in the circumferential direction. The flux path of the main inductance is illustrated in Figure 6.3.

Slot leakage inductance

The flux encircling the winding does not only go through the air gap. Some part of the flux closes its path through the slot and slot openings. This flux is the origin of the so-called slot leakage inductance. Figure 6.4 illustrates the flux path through the slot and the slot opening. A simple way

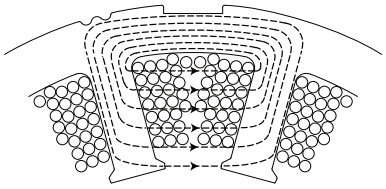

Figure 6.4: *Flux path for the slot leakage inductance.*

to calculate the slot leakage inductance is to calculate the magnetic field strength in the slot by applying Ampere's circuital law and then calculating the energy stored in the slot [34]. The slot leakage inductance is then obtained by solving

$$W = \frac{1}{2} \cdot L_{slot} \cdot I_{phase}^2 \tag{6.16}$$

In the method described above the permeability of iron is assumed to be infinite and skin effect is neglected.

The slot leakage inductance is then given by Eq. (6.17).

$$L_{slot} = 2 \cdot \frac{q_s}{3} \cdot n_{stack} \cdot n_s^2 \cdot \mu_0 \cdot \lambda \cdot \ell_m \tag{6.17}$$

where λ is the specific permeance coefficient. In [34] this coefficient is given for the different slot shapes, which are illustrated in Figure 6.5.

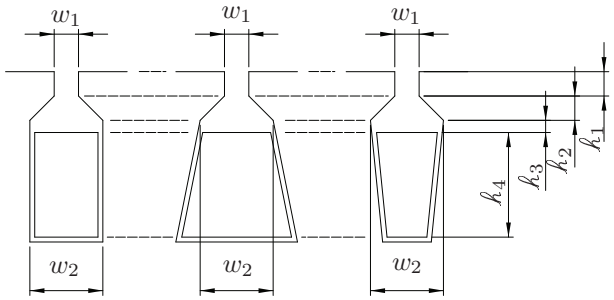

Figure 6.5: *Slot shapes with specified dimensions.*

λ is given by Eq. (6.18).

$$\lambda = \frac{h_4}{3 \cdot w_2} + \frac{h_3}{w_2} + \frac{h_1}{w_1} + \frac{h_2}{w_2 - w_1} \cdot \ln\left(\frac{w_2}{w_1}\right) \tag{6.18}$$

where coefficients w_1 and w_2 are calculated as follows

$$w_1 = 2 \cdot R_{si} \cdot \sin\left(\frac{\theta - \alpha_{shoe}}{2}\right); \tag{6.19}$$

and

$$w_2 = 2 \cdot (R_{si} + h_{sts}) \cdot \sin\left(\frac{\theta - \alpha_{tooth}}{2}\right); \tag{6.20}$$

From Figure 6.1(a) and Figure 6.5 the coefficients $h_1 - h_4$ can be identified as $h_1 = h_{stst}$, $h_2 = h_{sts} - h_{stst}$, $h_3 = h_{stst}$ and $h_4 = h_{st}$.

Air gap leakage inductance

The origin of the air gap leakage inductance is the part of the flux that encircles the winding outside the slot opening, but does not enter the translator back. The calculation of the air gap leakage inductance is done in a similar way as the calculation of the main inductance. Figure 6.6 shows the flux path of the inductance, which is calculated by Eq. (6.21).

$$L_{leak} = 2 \cdot n_{stack} \cdot \frac{q_s}{3} \cdot \frac{n_s^2 \cdot \mu_0 \cdot \ell_m \cdot (\delta + h_m)}{(R_{si} + 0.5 \cdot (\delta + h_m)) \cdot (\theta - \alpha_{shoe})} \tag{6.21}$$

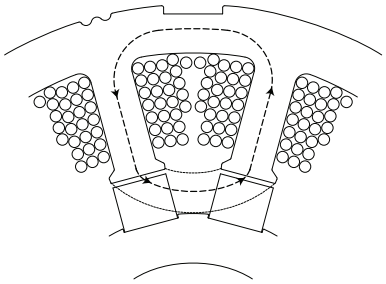

Figure 6.6: *Flux path for the leakage inductance between two stator teeth.*

Between-stack inductance

One component of the leakage inductance in the machine that is usually not present in a conventional machine, except for large synchronous machines, is the between-stack inductance. In order to calculate the inductance the conductors are treated as an infinitely long cylinder with a surface current I. Assuming a conductor of a length ℓ and a radius R_c the inductance of the coil with the number of conductors n each carrying a current I can be written as [43]:

$$L_{line} = \frac{\mu_0 \cdot \ell \cdot n^2}{2 \cdot \pi} \cdot \ln\left(\frac{r}{R_c}\right) \tag{6.22}$$

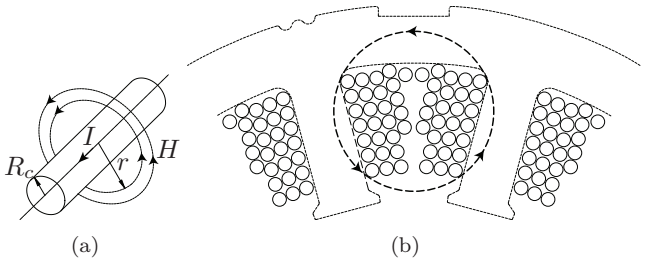

Figure 6.7: *Between-stack inductance, a) magnetic field about a cylindrical conductor b) winding in the machine treated as a circular conductor.*

The parameters r and R_c in Eq. (6.22) can be identified as $R_c = \sqrt{\frac{A_{ins}}{\pi}}$ and $r = w_t + R_c$, see Figure 6.7, where w_t is the width of the stator tooth. The leakage inductance between two stator stacks is given by

$$L_{stack} = 2 \cdot \frac{q_s}{3} \cdot (\ell_s - n_{stack} \cdot \ell_m) \cdot \mu_0 \cdot n_s^2 \cdot \ln\left(1 + \frac{w_t \cdot \sqrt{\pi}}{\sqrt{A_{ins}}}\right) \tag{6.23}$$

where the length of a winding in Eq. (6.22) can be identified as $\ell = (\ell_s - n_{stack} \cdot \ell_m)$.

End-winding inductance

The last inductance to be calculated is the end-winding inductance. Like in the case of the leakage inductance between two stator stacks the equation for the end winding inductance is derived assuming conductor in the coil as circular and infinitely long. Furthermore, it has been assumed that the end winding is a semi circle with the radii of R_{ew}, see Figure 6.8. According to [43] the end-leakage inductance is given by Eq. (6.24).

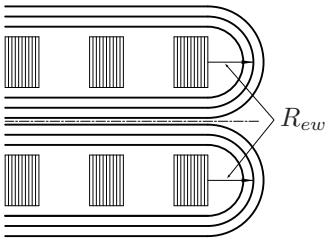

Figure 6.8: *Radius of the end winding in the machine.*

$$L_{end} = 2 \cdot \frac{q_s}{3} \cdot \mu_0 \cdot n_s^2 \cdot 2 \cdot R_{ew} \cdot \ln\left(\frac{2 \cdot R_{ew} \cdot \sqrt{\pi}}{\sqrt{A_{slot}}}\right) \tag{6.24}$$

where the radius R_{ew} is given by Eq. (6.25).

$$R_{ew} = \frac{1}{2} \cdot (w_t + w_s) \tag{6.25}$$

where w_s is the width of the slot at 2/3 height of the slot an is given by

$$w_s = 2 \cdot \left(R_{scu} + \frac{2}{3} \cdot \hbar_{st}\right) \cdot \sin\left(\frac{\theta - \alpha_{tooth}}{4}\right) \tag{6.26}$$

Total inductance

The total inductance is the sum of all inductances described previously and is given by

$$L_{tot} = L_{main} + L_{end} + L_{stack} + L_{slot} + L_{leak} \tag{6.27}$$

6.3.2 Resistance

The resistance of the winding is temperature dependent. As the temperature increases the resistivity of the material will also increase. The relationship between the temperature and the resistivity of copper is given by

$$\rho_{cu} = 1.72 \cdot 10^{-8} \cdot \left(1 + 3.9 \cdot 10^{-3} \left(T_{winding} - 20\right)\right) \tag{6.28}$$

where $T_{winding}$ is the temperature of the winding given in ℃. The phase resistance of the winding is then given by

$$R_{phase} = \frac{q_s}{3} \cdot \rho_{cu} \cdot \left(\frac{n_s \cdot (2 \cdot \ell_s + 2 \cdot \ell_{end})}{A_{cuc}}\right) \tag{6.29}$$

where ℓ_{end} is the length of the end winding. As in the case of the end leakage inductance calculations, the end winding is assumed to be a semicircle. The length of the end winding is then given by

$$\ell_{end} = \pi \cdot R_{ew} \tag{6.30}$$

6.4 Prototype design

Based on the design procedure described above the prototype of a novel linear TFM was designed and manufactured. As the machine is merely a proof-of-concept the tough requirement on the translator weight, for the FPEC application, was relaxed. However, some of the requirements were preserved, like the length of the machine and the outer diameter of the translator etc. Table 6.2 summarizes the requirements for the prototype machine design. Based on the requirements in Table 6.2 the prototype machine was designed. Besides the figures present in table 6.2, there are also some other design variables that must be specified prior to the start of the design procedure. These will be specified later in this section.

Although Eq. (5.19) shows that the force density of the machine reduces with increased number of slots the number of slots for the prototype was chosen to $q_s = 12$. This is done in order to avoid the unbalanced forces that can arise in the machine. Figure 6.9 shows forces in a machine with $q_s = 6$ and $q_s = 12$ slots.

As can be seen from Figure 6.9(a) in the 6 slots machine design, once the stator teeth are aligned with the magnets in phase 'a', stator teeth belonging to the phases 'b' and 'c' on the opposite side will be covered only by half the magnet area. This will lead to an unbalanced force that will attract the translator to one side of the stator. Eventually, this unbalance in the radial force may cause a severe damage to the machine. However, the radial forces are easily eliminated by doubling number of slots, which

Table 6.2: *Specifications for the prototype*

Parameter	Requirement
Translator outer diameter	$D_{to} = 110$ mm
Stroke length	$\ell_{stroke} = 110$ mm
Active length of the stator	$\ell_s \leq 220$ mm
Total length of the translator	$\ell_t \leq 330$ mm
Air gap length	$\delta = 1.25$ mm
Stator tooth flux	$B_{st} = 1.4$ T
Stator yoke flux	$B_{sy} = 1.4$ T
Translator yoke flux	$B_{ty} = 1.3$ T
Fundamental flux density in the air gap	$\hat{B}_\delta = 0.85$ T
Nominal average velocity	11 $\frac{\text{m}}{\text{s}}$
Induced voltage	$E_{phase} = 220$ V
Operating force	2.0 kN
Efficiency	> 90 %
Fill factor for the winding	$k_{fill} = 0.5$
Current density	$J = 8$ $\frac{\text{A}}{\text{mm}^2}$

is illustrated in Figure 6.9(b). As can be seen, the magnets belonging to the phase 'a' exist on opposite sides which results in zero resultant radial force. Therefore, it was decided that the prototype should be designed with $q_s = 12$ slots.

In Chapter 5, while deriving the machine equations, it was assumed that the magnets and the stator teeth have the same width in the circumferential direction. This assumption is made only to simplify the analysis. In reality, there is no restriction on how wide the magnets can be and they can cover the whole circumference of the translator. The question is only how much of the additional flux contribution is useful flux and how much is leakage flux in relation to the additional magnet material required to produce this flux.

In the prototype, in order to avoid leakage flux in the circumferential direction between two magnets belonging to the same phase, the width of the magnets was set to 45 electrical degrees. In the axial direction the ratio between the magnet length ℓ_m and the pole length ℓ_{pole} was set to $\frac{2}{3}$. The total height of the stator tooth shoe is set to $h_{sts} = 3$ mm, while the height of the stator tooth shoe tip is set to $h_{stst} = 1.5$ mm. The fill factor for the winding k_{fill} is assumed to be 50% of the total slot area available.

Based on the specification and the chosen values above the prototype machine was designed. The performance data for the machine is presented in Table 6.3. During the design procedure the fundamental component of the flux density was considered in the transverse plane of the machine only,

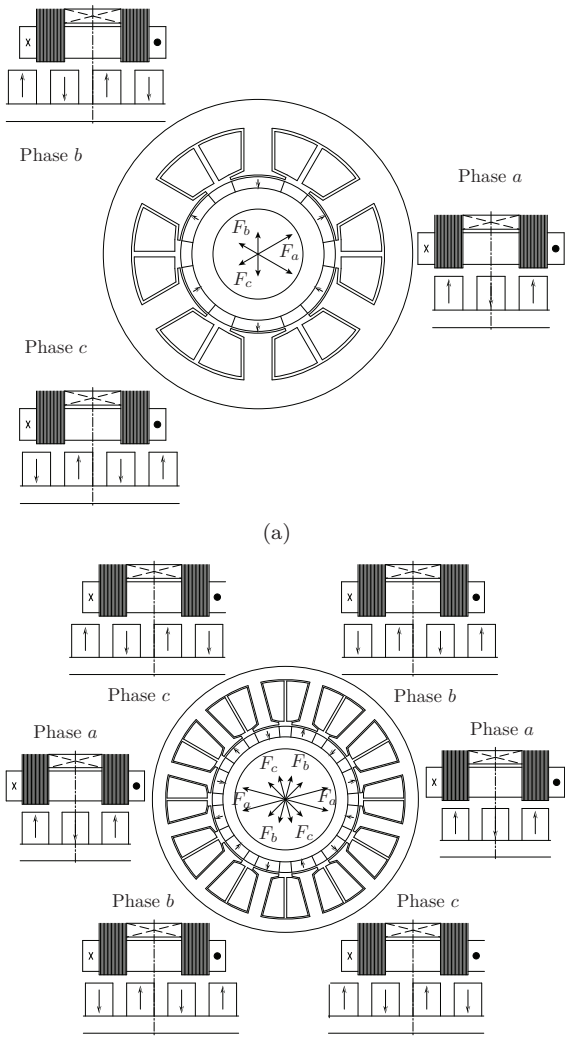

Figure 6.9: *Cross-sectional view of the novel TFM a) $q_s = 6$ and b) $q_s = 12$ slots.*

which resulted in a larger magnet height.

Table 6.3: *Performance figures of the prototype design.*

Parameter	Requirement
Force produced	2.542 N
Efficiency	91.52%
Phase resistance	0.2292 Ω
Phase inductance	2.0154 mH
Magnet height	12.055 mm
Phase current	46.44 A
Outer diameter of the stator	198.25 mm
Number of stacks	8
Number of poles on the translator	22

6.5 Improved analytical model

The analytical results, based on the simplified model presented in the previous sections, resulted in a quite large disagreement with the results observed from the Finite Element analysis. The induced voltage and the force produced in the machine indicated a difference in the results that was more than 50% compared with each other. Obviously, there is a need of an analytical model that can predict the results more correctly.

The flux paths in a TFM are truly three dimensional. Therefore, one of the most important tasks is to identify the true flux paths in a correct way. Thus, the goal of the improved model is to develop an analytical tool that will predict the induced voltage and the force produced more accurately.

During the translator motion the reluctance model will change in accordance with the position of the magnets relative to the stator teeth. It will also depend on the ratio between the pole length and the length of the magnets. There are several different ways to configure the machine parameters, where the length of the magnets, length of the stator stack and length of the pole can be chosen freely. A certain given combination of the variables will influence not only the modeling of the reluctance network, but also the number of network models that are required to describe the translator motion. In the prototype, three different reluctance models are identified and used, as illustrated in Figure 6.10.

6.5.1 Magnet flux

The main leakage in the machine is in the axial direction. The inactive magnets will attract the magnetic flux from the useful flux that is in the stator tooth, thereby reducing the force and the EMF produced in the machine. The discrepancy between the results from the 2D-FEM analysis

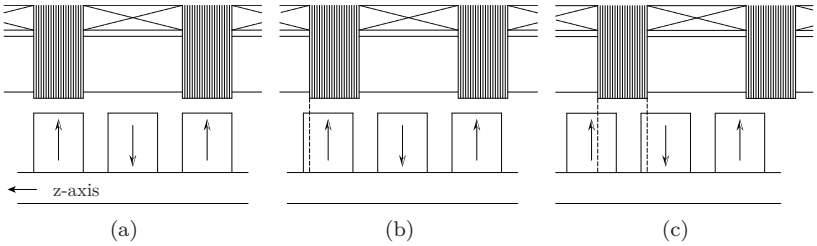

Figure 6.10: *Three different reluctance models identified as the translator moves along the z-axis a) Reluctance model I, b) Reluctance model II and c) Reluctance model III.*

and simple analytical model showed the need of a more accurate analytical model. It became necessary to extend the simple 2D reluctance model in the third dimension as shown in Figure 6.11. There are some differences in

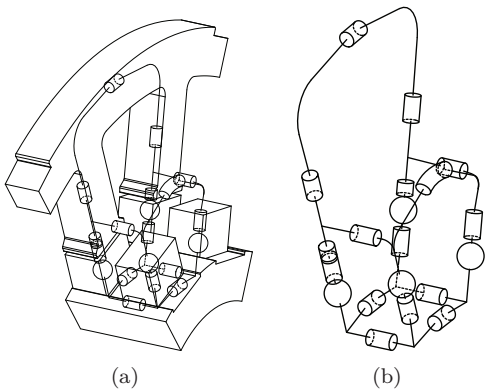

Figure 6.11: *3D view of the two pole arrangement with one stator stack a) modeling of different reluctances in the machine b) reluctance model extracted.*

the simulated model, analytical model and the prototype. Similar to the pressure fingers in big synchronous machines, the linear TFM has spacers between the stacks. In the prototype, the spacers are made of a non magnetic steel, which in theory should have magnetic properties of air, i.e. $\mu_r = 1$. However, due to the machining process the material was heated and as a result it slightly lost its nonmagnetic properties i.e. became magnetic. Although the increase in the relative permeability is relatively small, it will certainly increase the leakage flux compared to the analytical and FEM results, where only air is used.

First reluctance model

As illustrated in Figure 6.12 the first reluctance model represents the magnets aligned with the teeth, i.e. d-direction. Due to the symmetry, it is enough to consider only one pole length in the analysis.

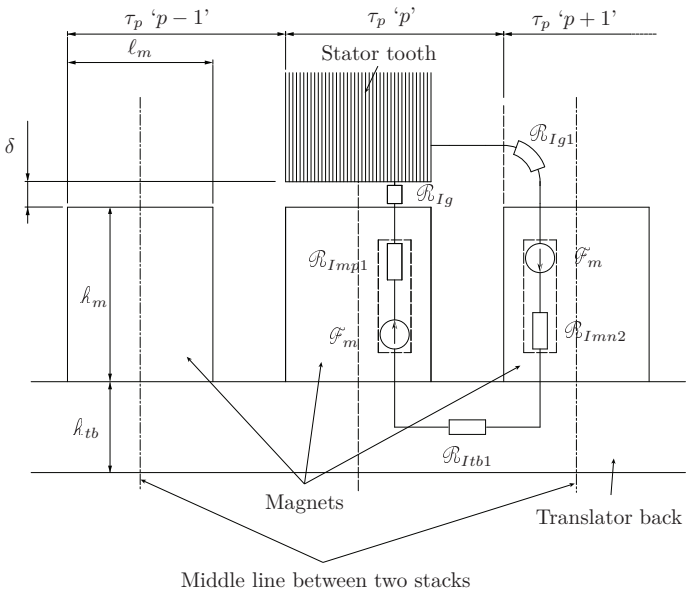

Figure 6.12: *Axial view, translator positioned in d-direction.*

According to [44] the equivalent MMF-source in the magnet can be written as in

$$\mathscr{F}_m = h_m \cdot H_c \tag{6.31}$$

where the relation between the residual magnet coercivity and magnet residual magnetization is $\mu_m = \frac{B_{rm}}{H_c}$.

The inner reluctance of the positive oriented magnet under the stator tooth is given by

$$\mathscr{R}_{Imp1} = \frac{h_m}{\mu_0 \cdot \mu_{rm} \cdot w_m \cdot \frac{\ell_m}{2}} \tag{6.32}$$

Due to the symmetry the reluctance of the other magnets are equal to the first magnet oriented in the positive direction and therefore $\mathscr{R}_{Imn1} = \mathscr{R}_{Imn2} = \mathscr{R}_{Imp2} = \mathscr{R}_{Imp1}$. The subscripts '$mp$' and '$mn$' represent the magnets oriented in positive and negative directions respectively.

The reluctances for the translator back are given by following, see Figure 6.12 and Figure 6.13.

$$\mathcal{R}_{Itb1} = \frac{\tau_p - \frac{\ell_m}{2}}{\mu_0 \cdot \mu_{ri} \cdot w_m \cdot h_{tb}} \tag{6.33}$$

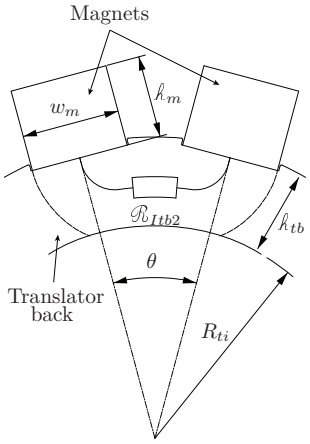

Figure 6.13: *Cross sectional view, calculation of the reluctance in the translator back.*

$$\mathcal{R}_{Itb2} = \frac{\theta \cdot \left(R_{ti} + \frac{h_{tb}}{2}\right)}{\mu_0 \cdot \mu_{ri} \cdot \ell_m \cdot h_{tb}} \tag{6.34}$$

The stator back and the stator tooth reluctances can be derived as follows.

The stator tooth reluctance consists of two parts: $\mathcal{R}_{Istt}$ which represent the main part of the tooth and $\mathcal{R}_{Ists}$ which represents the stator tooth shoe, see Figure 6.15. The total reluctance of the stator tooth is then written as $\mathcal{R}_{Ist} = \mathcal{R}_{Istt} + \mathcal{R}_{Ists}$ where reluctances $\mathcal{R}_{Istt}$ and $\mathcal{R}_{Ists}$ are given by Eq. (6.35) and Eq. (6.36) respectively.

$$\mathcal{R}_{Istt} = \frac{h_{st} + \frac{h_{sb}}{2}}{\mu_0 \cdot \mu_{ri} \cdot w_t \cdot \frac{\ell_m}{2}} \tag{6.35}$$

$$\mathcal{R}_{Ists} = \frac{h_{sts}}{\mu_0 \cdot \mu_{ri} \cdot w_m \cdot \frac{\ell_m}{2}} \tag{6.36}$$

The reluctance of the stator back is given by Eq. (6.37).

$$\mathcal{R}_{Isb} = \frac{\theta \cdot \left(R_{so} - \frac{h_{sb}}{2}\right)}{\mu_0 \cdot \mu_{ri} \cdot h_{sb} \cdot \frac{\ell_m}{2}} \tag{6.37}$$

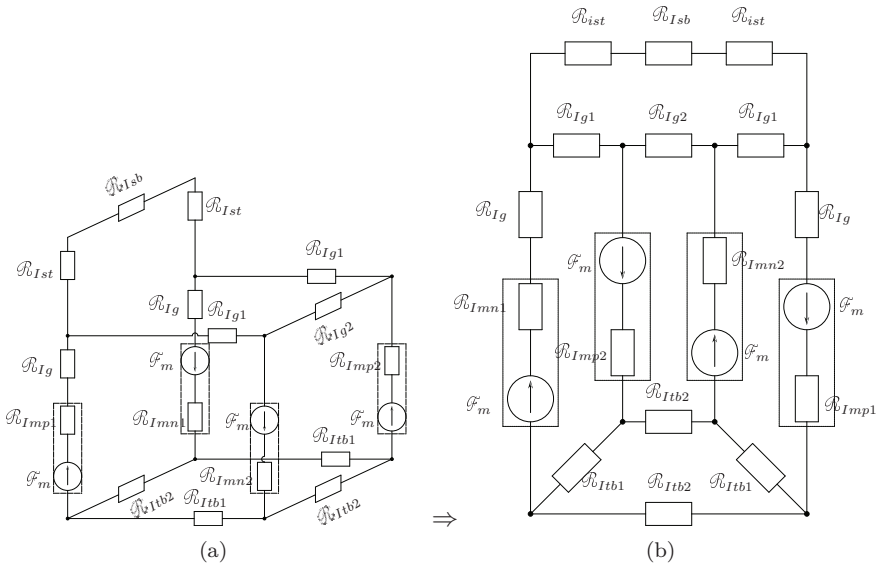

Figure 6.14: *First reluctance network used in the analysis of the magnet flux a) 3D-view and b) simplified 3D-network into a grid.*

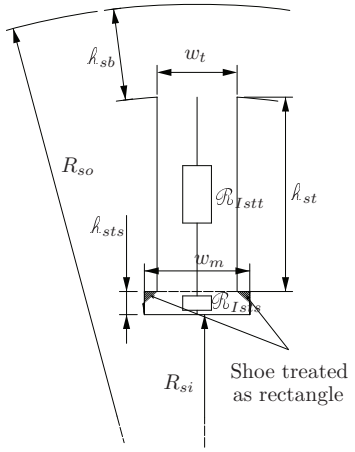

Figure 6.15: *Cross sectional view, calculation of the reluctance in the stator tooth.*

There are three different air gap reluctances denoted by subscript 'g'. The first reluctance is under the stator tooth which is seen by the active magnets in pole 'p'. This reluctance is given by

$$\mathcal{R}_{Ig} = \frac{\delta}{\mu_0 \cdot \frac{\ell_m}{2} \cdot w_m} \tag{6.38}$$

The remaining two reluctances are mostly seen by the inactive magnets, belonging to adjacent pole '$p+1$'. '*Inactive*', in this context, implies that these magnets face only air. One of the reluctances lies in the circumferential direction between the magnets. This reluctance is denoted as $\mathcal{R}_{Ig2}$ in Figure 6.14. The cross section of the translator together with the magnets is illustrated in Figure 6.16.

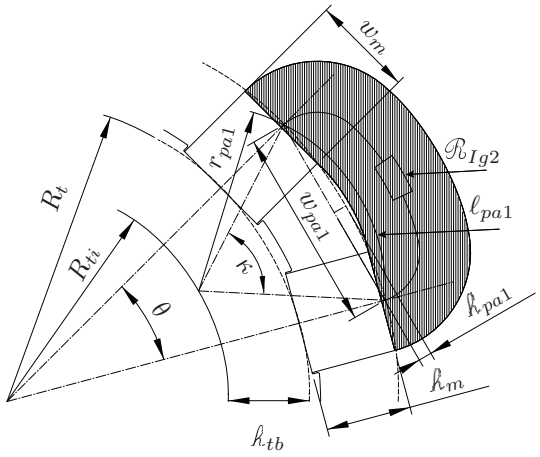

Figure 6.16: *Cross sectional view of a part of the translator.*

$$\begin{cases} w_{pa1} = 2 \cdot R_{to} \cdot \sin\left(\frac{\theta}{2}\right) \\ h_{pa1} = R_{to} \cdot \left(1 - \cos\left(\frac{\theta}{2}\right)\right) \\ \kappa = 2 \cdot \arctan\left[\frac{\frac{w_{pa1}}{2}}{h_m + h_{tb} - h_{pa1}}\right] \\ r_{pa1} = \sqrt{\left(\frac{w_{pa1}}{2}\right)^2 + \left(h_m + h_{tb} - h_{pa1}\right)^2} \\ \ell_{pa1} = r_{pa1} \cdot \kappa \end{cases} \tag{6.39}$$

The air gap reluctance in the circumferential direction is given by

$$\mathcal{R}_{Ig2} = \frac{\ell_{pa1}}{\mu_0 \cdot w_m \cdot \frac{\ell_m}{2}} \tag{6.40}$$

The other one is the reluctance between the stator tooth in pole 'p' and the magnets in adjacent pole '$p+1$'. This reluctance lies in the axial plane of the machine, and is strongly associated with the leakage flux in the machine. Furthermore, as indicated in Figure 6.17 this reluctance is

divided into three different parts. The first part is the reluctance of the air gap in the machine. The second part of the reluctance assumes that the flux follows a circular path with the origo at the cross section of two lines: 'Line 1' (along the height of the inner diameter of the stator) and 'Line 2' (from the corner of the magnet belonging to the pole '$p+1$'), see Figure 6.17. The last part is the space between the stator tooth and an extension of the line drawn from the corner of the magnet in the pole '$p+1$'. The total reluctance is then $\mathscr{R}_{Ig1} = \mathscr{R}_{Ig11} + \mathscr{R}_{Ig12} + \mathscr{R}_{Ig13}$, where the three reluctances described above are given in equations 6.41, 6.42 and 6.43.

$$\mathscr{R}_{Ig11} = \frac{\delta}{\mu_0 \cdot w_m \cdot \frac{\ell_m}{2}} \tag{6.41}$$

$$\mathscr{R}_{Ig12} = \frac{\pi \cdot \ell_m}{4 \cdot \mu_0 \cdot w_m \cdot \frac{\ell_m}{2}} \tag{6.42}$$

$$\mathscr{R}_{Ig13} = \frac{\tau_p - \ell_m}{\mu_0 \cdot w_m \frac{\ell_m}{2}} \tag{6.43}$$

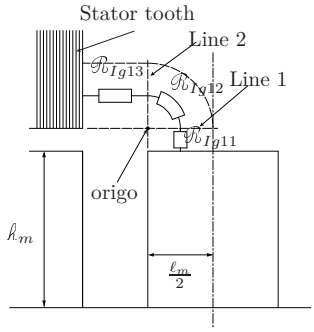

Figure 6.17: *Axial view, calculation of the reluctance $\mathscr{R}_{Ig1}$, between the stator tooth and the magnet in pole '$p+1$'.*

As only half of the geometry is considered due to the symmetry, the total flux in the stator back is twice the calculated value from the circuit.

Second reluctance model

Figure 6.11 shows the magnets in pole 'p' aligned with the stator tooth, i.e. the translator is in the d-axis. Once the translator starts to move and the magnets, in pole 'p', start to leave the stator tooth a second more complex model is used. The axial view of the model is illustrated in Figure 6.18.

Due to the symmetry only two poles are considered and modeled.

As the figure shows, a few additional leakage paths have been added. The magnets in pole 'p' have been divided into two parts. The first one,

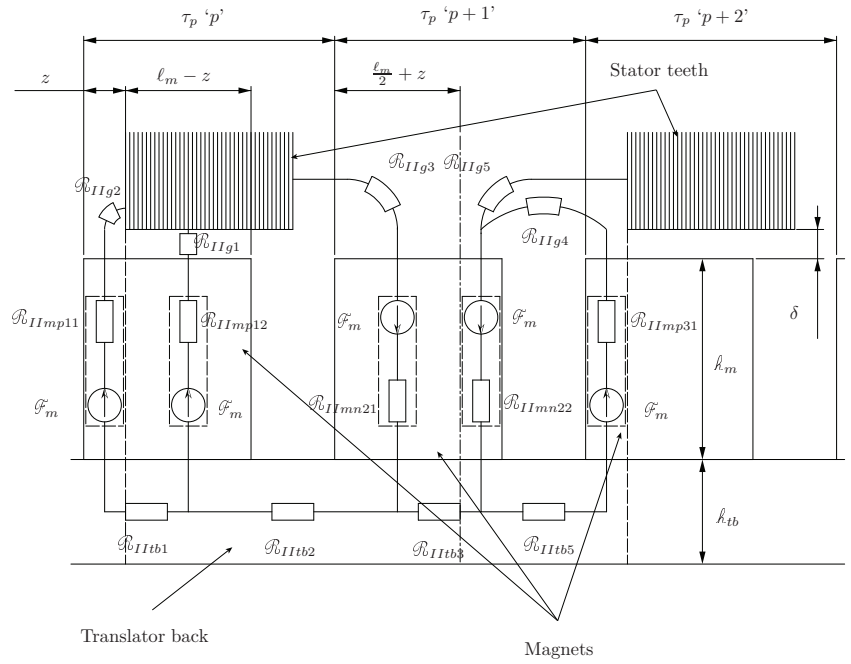

Figure 6.18: *Axial view of the machine used for the 2-D reluctance network development* $z \leq (\ell_{pole} - \ell_m)$.

which is still under the stator tooth, and the second one which is just outside the stator tooth. Furthermore, the magnet in pole '$p + 1$' is also divided into two parts. The magnet is divided by the middle line between two stator stacks. The first part is closer to the stator tooth in pole 'p' and the second is closer to the stator tooth in pole '$p + 2$'. This means that the first part of the magnet would influence the flux in pole 'p' while the second part would have some influence on the flux in pole '$p + 2$'.

The reluctance in the translator back, between poles 'p' and '$p + 1$', is given by Eq. (6.44) and Eq. (6.45). Eq. (6.44) represents the reluctance between two parts of the magnet in pole 'p'.

$$\mathcal{R}_{IItb1} = \frac{\ell_m + h_{tb}}{2 \cdot \mu_0 \cdot \mu_{ri} \cdot h_{tb} \cdot w_m} \tag{6.44}$$

$$\mathcal{R}_{IItb2} = \frac{3 \cdot \ell_{pole} - 2 \cdot \ell_m + 2 \cdot h_{tb}}{2 \cdot \mu_0 \cdot \mu_{ri} \cdot h_{tb} \cdot w_m} \tag{6.45}$$

Due to the symmetry the reluctance between two parts of the magnet in pole $p + 1$ is the same as given in Eq. (6.44), $(\mathcal{R}_{IItb3} = \mathcal{R}_{IItb1})$.

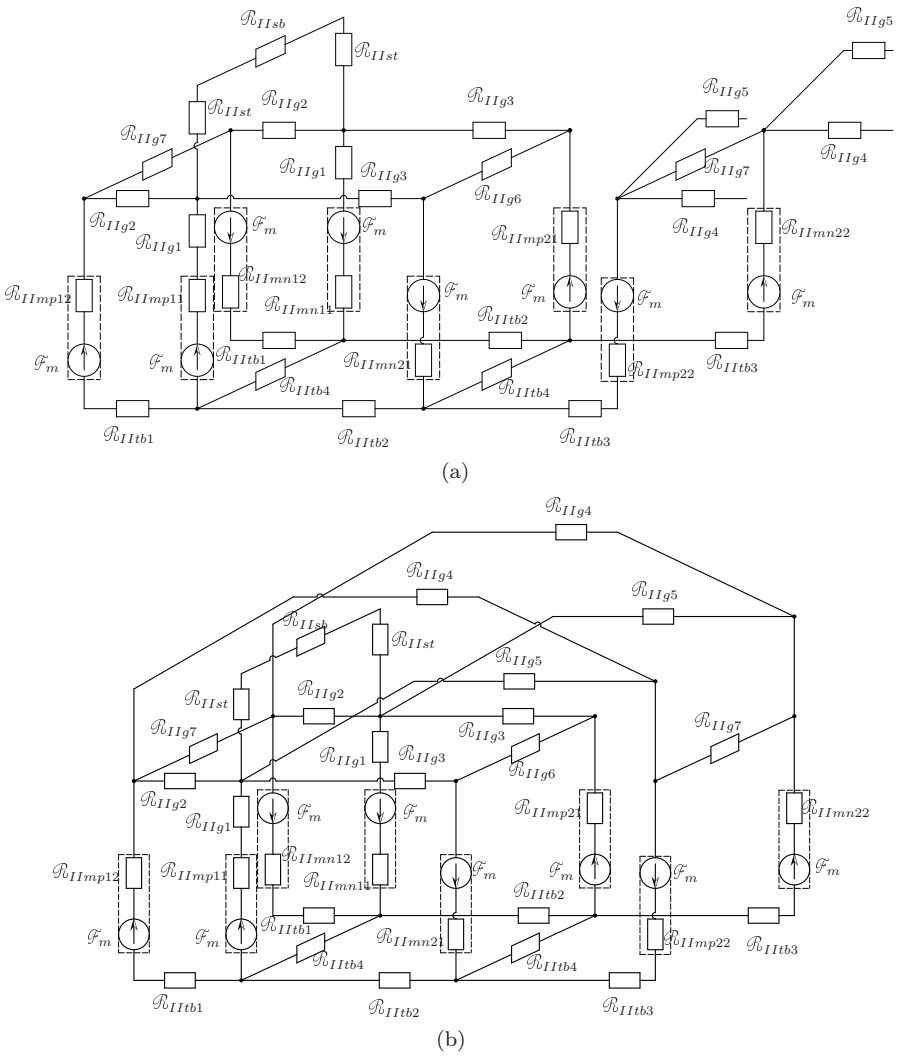

Figure 6.19: *3D-reluctance network for $z > (\ell_{pole} - \ell_m)$ a) original b) modified due to the presence of symmetry.*

Like in the previous model, the subscripts '*mp*' and '*mn*' represent the magnets oriented in positive and negative directions respectively. Furthermore, the magnets are divided into two parts: '1' and '2' added to the subscripts. Internal reluctances of the magnets are given by Eq. (6.48), Eq. (6.49), Eq. (6.46) and Eq. (6.47) respectively.

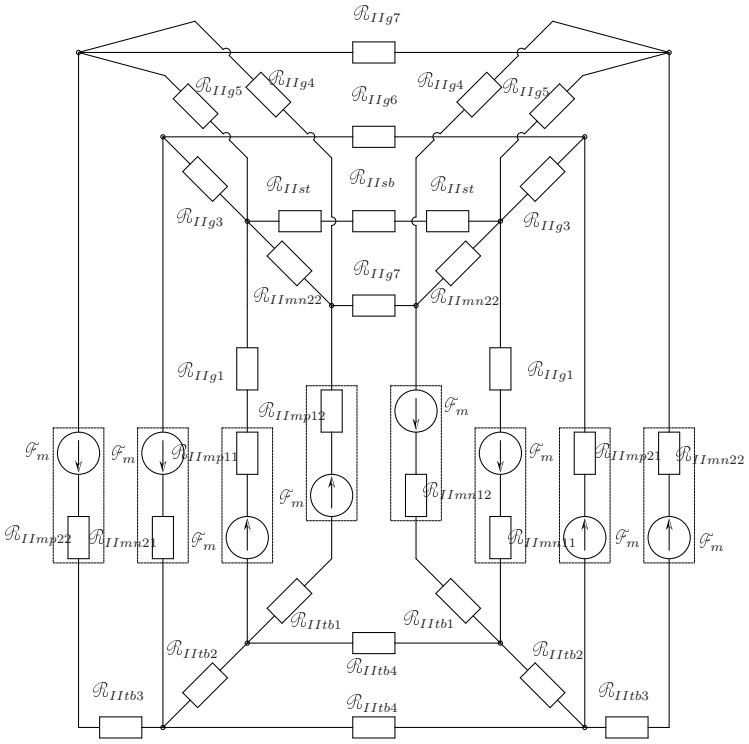

Figure 6.20: *Second reluctance network for $z > (\ell_{pole} - \ell_m)$ simplified into a grid.*

$$\mathcal{R}_{IImp11} = \frac{k_m}{\mu_0 \cdot \mu_m \cdot w_m \cdot z} \tag{6.46}$$

$$\mathcal{R}_{IImp12} = \frac{k_m}{\mu_0 \cdot \mu_m \cdot w_m \cdot (\ell_m - z)} \tag{6.47}$$

$$\mathcal{R}_{IImn21} = \frac{k_m}{\mu_0 \cdot \mu_m \cdot w_m \cdot (\tau_p - \ell_m + z)} \tag{6.48}$$

$$\mathcal{R}_{IImn22} = \frac{k_m}{\mu_0 \cdot \mu_m \cdot w_m \cdot (\tau_p - \ell_m - z)} \tag{6.49}$$

The internal reluctances of the magnets, in poles 'p' and '$p+1$', on the opposite side are the same as the reluctances written in the equations above and are given by $\mathcal{R}_{IImn11} = \mathcal{R}_{IImp11}$, $\mathcal{R}_{IImn12} = \mathcal{R}_{IImp12}$, $\mathcal{R}_{IImp21} = \mathcal{R}_{IImn21}$ and $\mathcal{R}_{IImp22} = \mathcal{R}_{IImn22}$.

The air gap reluctance in pole 'p', seen by the part of the magnet just outside the stator tooth is the sum of two reluctances given by Eq. (6.50) and Eq. (6.51), see Figure 6.21.

$$\mathcal{R}_{IIg11} = \frac{\pi}{4 \cdot \mu_0 \cdot w_m} \tag{6.50}$$

$$\mathcal{R}_{IIg12} = \frac{\delta}{\mu_0 \cdot z \cdot w_m} \tag{6.51}$$

The part of the magnet that is still under the stator tooth faces the air gap reluctance given by

$$\mathcal{R}_{IIg2} = \frac{\delta}{\mu_0 \cdot (\ell_m - z) \cdot w_m} \tag{6.52}$$

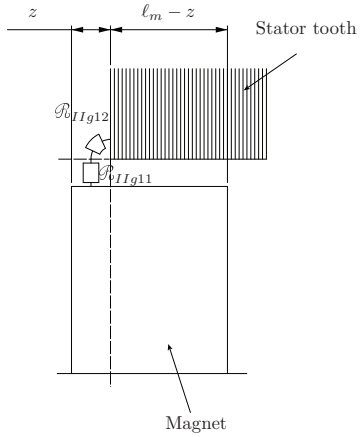

Figure 6.21: *The part of the magnet in pole p outside the stator tooth. Air gap reluctance is made up of two parts.*

Similarly, the air gap reluctance, seen by the first part of the magnet in pole '$p+1$' is the sum of the three reluctances $\mathcal{R}_{IIg3} = \mathcal{R}_{IIg31} + \mathcal{R}_{IIg32} + \mathcal{R}_{IIg33}$. These three reluctances are given by Eq. (6.53), Eq. (6.54) and Eq. (6.55) respectively. These reluctances are illustrated in Figure 6.22.

$$\mathcal{R}_{IIg31} = \frac{\ell_m - 2 \cdot z}{\mu_0 \cdot w_m \cdot (\ell_m + 2 \cdot z)} \tag{6.53}$$

$$\mathcal{R}_{IIg32} = \frac{\pi \cdot (\ell_m + 2 \cdot z)}{4 \cdot \mu_0 \cdot w_m \cdot (\ell_m + 2 \cdot z)} \tag{6.54}$$

$$\mathcal{R}_{IIg33} = \frac{2 \cdot \delta}{\mu_0 \cdot w_m \cdot (\ell_m + 2 \cdot z)} \tag{6.55}$$

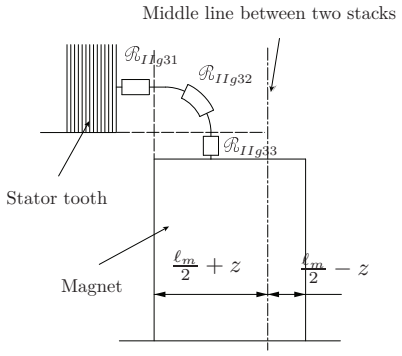

Figure 6.22: *The part of the magnet in pole 'p+1' outside the stator tooth. Air gap reluctance consists of three parts.*

The second part of the magnet, in pole '$p + 1$', will see two different air gap reluctances. The first is the air gap reluctance between the magnet in pole '$p + 1$' and the magnet in pole '$p + 2$'. The second is between the magnet in pole '$p+1$' and the stator tooth in pole '$p+2$'. This is illustrated in Figure 6.23.

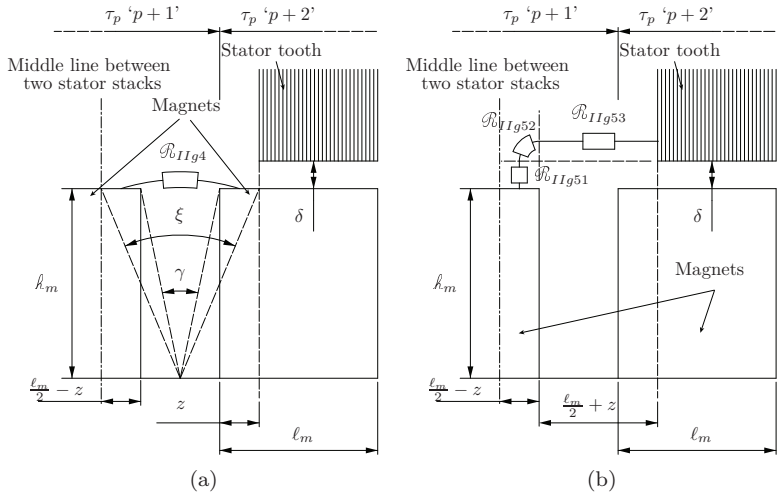

Figure 6.23: *Axial view of the machine a) Air gap reluctance between magnets in pole 'p + 1' and 'p + 2' and b) Air gap reluctance between the magnet in pole 'p + 1' and stator tooth in pole 'p + 2'*

In an attempt to calculate the air gap reluctance between the magnets an approximate length of the flux tube is calculated at first. This length

is calculated as a product of a radius, given by Eq. (6.56), and an angle, given by Eq. (6.57).

$$r_{pa2} = \sqrt{\left(\frac{1}{2} \cdot (\tau_p - \ell_m + z)\right)^2 + \hbar_m^2} \tag{6.56}$$

$$\xi = 2 \cdot \arcsin\left[\frac{\tau_p - \ell_m + z}{2 \cdot \sqrt{\left(\frac{1}{4} \cdot (\tau_p - \ell_m + z)\right)^2 + \hbar_m^2}}\right] \tag{6.57}$$

The air gap reluctance between the magnets (pole '$p+1$' and '$p+2$') is given by

$$\mathscr{R}_{IIg4} = \frac{\xi \cdot r_{pa2}}{\mu_0 \cdot w_m \cdot z} \tag{6.58}$$

The air gap reluctance between the magnet in pole '$p+1$' and the stator tooth in pole '$p+2$' is the sum of reluctances given by equations Eq. (6.59), Eq. (6.60) and Eq. (6.61), $\mathscr{R}_{IIg5} = \mathscr{R}_{IIg51} + \mathscr{R}_{IIg52} + \mathscr{R}_{IIg53}$.

$$\mathscr{R}_{IIg51} = \frac{2 \cdot \delta}{\mu_0 \cdot w_m \left(\ell_m - 2 \cdot z\right)} \tag{6.59}$$

$$\mathscr{R}_{IIg52} = \frac{\pi}{4 \cdot \mu_0 \cdot w_m} \tag{6.60}$$

$$\mathscr{R}_{IIg53} = \frac{2 \cdot (\tau_p - \ell_m + z)}{\mu_0 \cdot w_m \left(\ell_m - 2 \cdot z\right)} \tag{6.61}$$

The reluctance between the inactive magnets, i.e. the reluctance between the positive and negative oriented magnet in pole '$p+1$' will be derived from the following. This reluctance is in the circumferential direction. The cross section of the translator together with the magnets is illustrated in Figure 6.16. The air gap reluctance is given by

$$\mathscr{R}_{IIg6} = \frac{\ell_{pa1}}{\mu_0 \cdot w_m \cdot \left(\frac{\ell_m}{2} + z\right)} \tag{6.62}$$

The translator back reluctance in the circumferential direction is calculated as in the case of the first reluctance model. The only difference is that another cross sectional width of the reluctance path is taken. The iron reluctance in the translator back is given by

$$\mathscr{R}_{IItb4} = \frac{\hbar_{tb} + \theta \cdot \left(R_{ti} + \frac{\hbar_{tb}}{2}\right)}{\mu_0 \cdot \mu_{ri} \cdot w_m \cdot \hbar_{tb}} \tag{6.63}$$

The iron reluctance in the stator teeth and the stator back are given by equation below.

$$\mathcal{R}_{IIsb} = \frac{\theta \cdot \left(R_{so} - \frac{h_{sb}}{2}\right)}{\mu_0 \cdot \mu_{ri} \cdot h_{sb} \cdot \ell_m} \tag{6.64}$$

In the same way as in the first reluctance model, the stator tooth reluctance is divided into two parts: the main part of the tooth and the stator tooth shoe. The total reluctance for the stator tooth can be written as $\mathcal{R}_{IIst} = \mathcal{R}_{IIstt} + \mathcal{R}_{IIsts}$ where $\mathcal{R}_{IIstt}$ and $\mathcal{R}_{IIsts}$ are given by Eq. (6.65) and Eq. (6.66) respectively.

$$\mathcal{R}_{IIstt} = \frac{h_{st} + \frac{h_{sb}}{2}}{\mu_0 \cdot \mu_{ri} \cdot w_t \cdot \ell_m} \tag{6.65}$$

$$\mathcal{R}_{IIsts} = \frac{h_{sts}}{\mu_0 \cdot \mu_{ri} \cdot w_m \cdot \ell_m} \tag{6.66}$$

Third reluctance model

As the translator moves further, the magnet from the neighboring pole '$p+1$' will start to enter the stator tooth. The part of the magnet from the pole 'p' is, however, still under the stator tooth. Once the magnet from pole '$p+1$' enters the stator tooth the third reluctance model is used as illustrated in Figure 6.24. The transition between these two models can be observed in the results where the slope of the flux density changes, see Figure 6.26.

The reluctances for the third model are derived in a similar way as previously. The equations for the different reluctances are given in Appendix A.

Solving procedure of the circuits

To solve equations for the equivalent reluctance network Kirchhoff's and Ohm's laws for the electrical circuit are adopted to the magnetic circuit [45]. Applying Kirchhoff's Current Law (KCL) together with the Ohm's Law, the following equation can be written [46].

$$\nu_p \cdot G_{pp} - \sum_{\substack{j=1 \\ j \neq p}}^{n} \nu_j \cdot G_{jp} = \sum_{\substack{j=1 \\ j \neq p}}^{n} E_{pj} \cdot G_{pj} \tag{6.67}$$

On the left-hand side of Eq. (6.67) G_{pp} is the sum of all permeances connected to node p. Permeance G_{jp} represents the sum of all permeances that are connected between the nodes j and p. The right-hand side of Eq. (6.67) represents the sum of the product between the permeance and

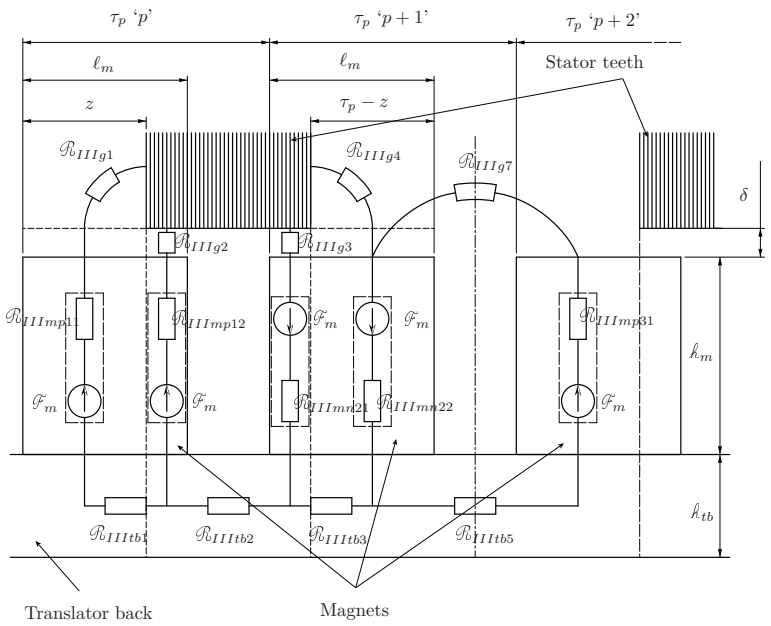

Figure 6.24: *Axial view of the machine used for the 2-D reluctance network development $z > (\ell_{pole} - \ell_m)$in the third reluctance model.*

the MMF between two nodes. The product is positive if the MMF sources work toward the node; otherwise it will have a negative sign. In order to solve Eq. (6.67) one node in the circuit has to be grounded.

In matrix notation this is given by

$$\boldsymbol{\nu}\mathbf{G} = \mathbf{F} \tag{6.68}$$

where $\mathbf{G}$ is a modified permeance matrix and $\mathbf{F}$ is a modified matrix with the product of the magnet MMF and the branch reluctance. The modification is achieved by grounding one node such that one column and one row can be removed from matrix $\mathbf{G}$ and one row from matrix $\mathbf{F}$. A similar way to solve the circuit equations has been described in [47].

The solution for $\boldsymbol{\nu}$ gives the potential in different nodes. Once these are known the desired fluxes can be calculated. The result for the flux in the stator back is shown in Figure 6.26.

The derivation procedure is presented in Appendix B.

6.5.2 Armature reaction field

Not only the leakage flux from the magnets is a design challenge, the flux leakage from the armature reaction is equally important. In order to have a

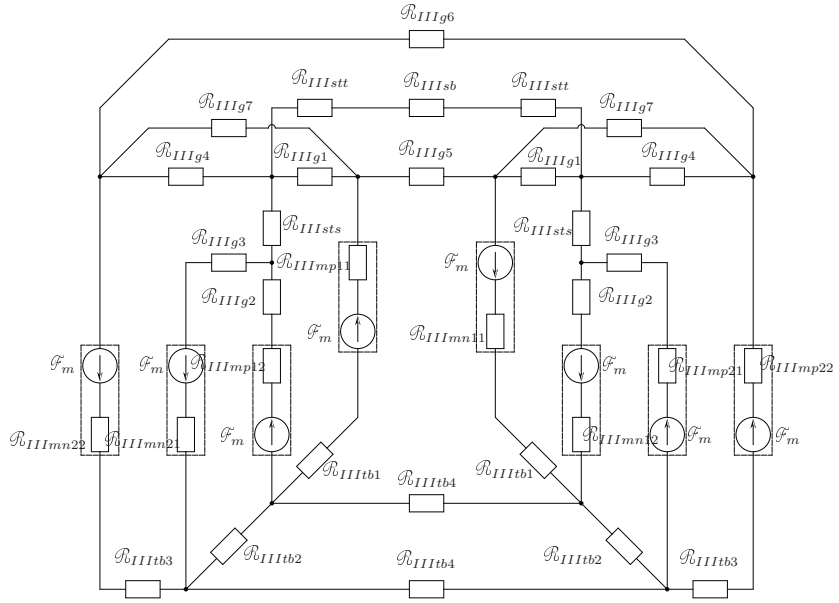

Figure 6.25: *3D-reluctance network used in the analytical model $z > (\ell_{pole} - \ell_m)$ for the third reluctance model.*

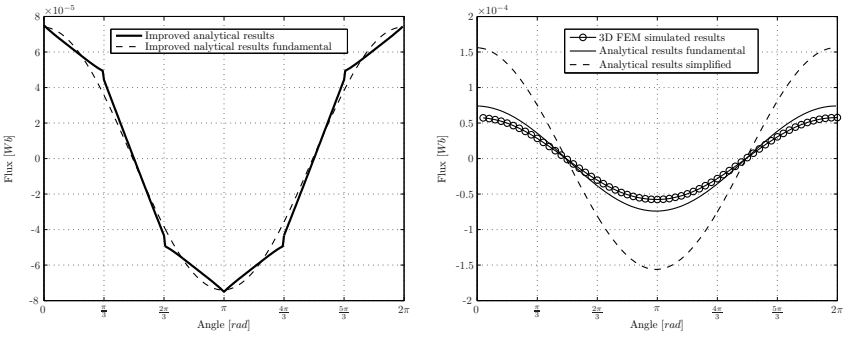

(a) (b)

Figure 6.26: *Flux in the stator back as a function of the translator position a)analytical results b) comparison of analytical and FEM-simulated results.*

better knowledge about the useful armature flux, a more detailed reluctance network of the stator is needed.

Figure 6.27 shows the reluctance network of the stator for two pole pairs, which contains one stator stack together with the space between the

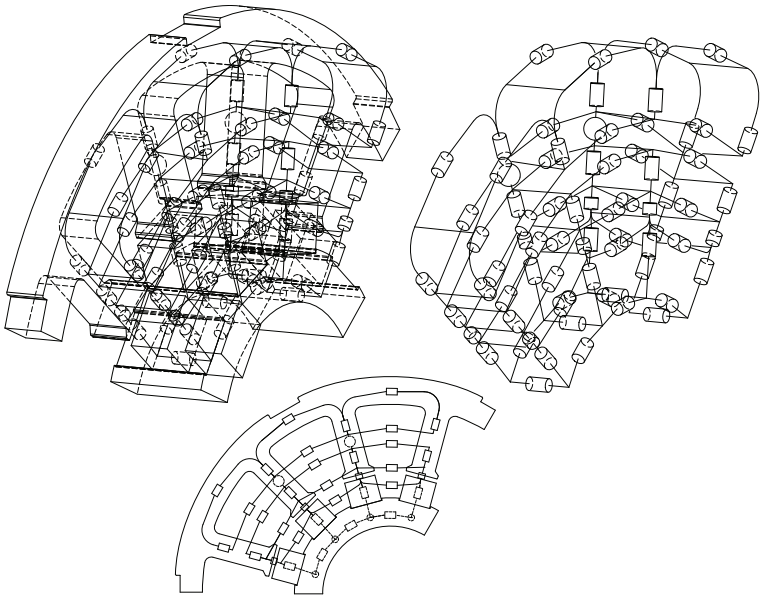

Figure 6.27: *3-D view of the stator reluctance network.*

stator stacks. Because of the 3D nature of the flux, the reluctance network of the armature reaction field has to be accounted in all three dimensions. After some modification the 3-D reluctance network, shown in Figure 6.27, is simplified to a grid reluctance network shown in Figure 6.28.

For simplicity the stator teeth shoe is assumed to be rectangular. Figure 6.29 shows a magnetic circuit for the armature field. As can be seen in this figure the stator tooth reluctance is separated into two parts, where the flux source (the product $n_s \cdot I$ of the stator winding) is placed in between. This is done in order to model the slot leakage reluctance more accurately compared with describing the total slot with only one reluctance.

The reluctance for the stator back was already calculated in the previous section. Thus, $\mathscr{R}_{IVsb}$ is found from

$$\mathscr{R}_{IVsb} = \mathscr{R}_{IIsb} \tag{6.69}$$

In a similar way the reluctance in the air between the stacks can be calculated from

$$\mathscr{R}_{IVsba} = \frac{\theta \cdot \left(R_{so} - \frac{h_{sb}}{2}\right)}{\mu_0 \cdot h_{sb} \cdot (2 \cdot \tau_p - \ell_m)} \tag{6.70}$$

As mentioned, the total tooth reluctance is divided into two equal parts. By doing so, the slot leakage is modeled more accurately. The results

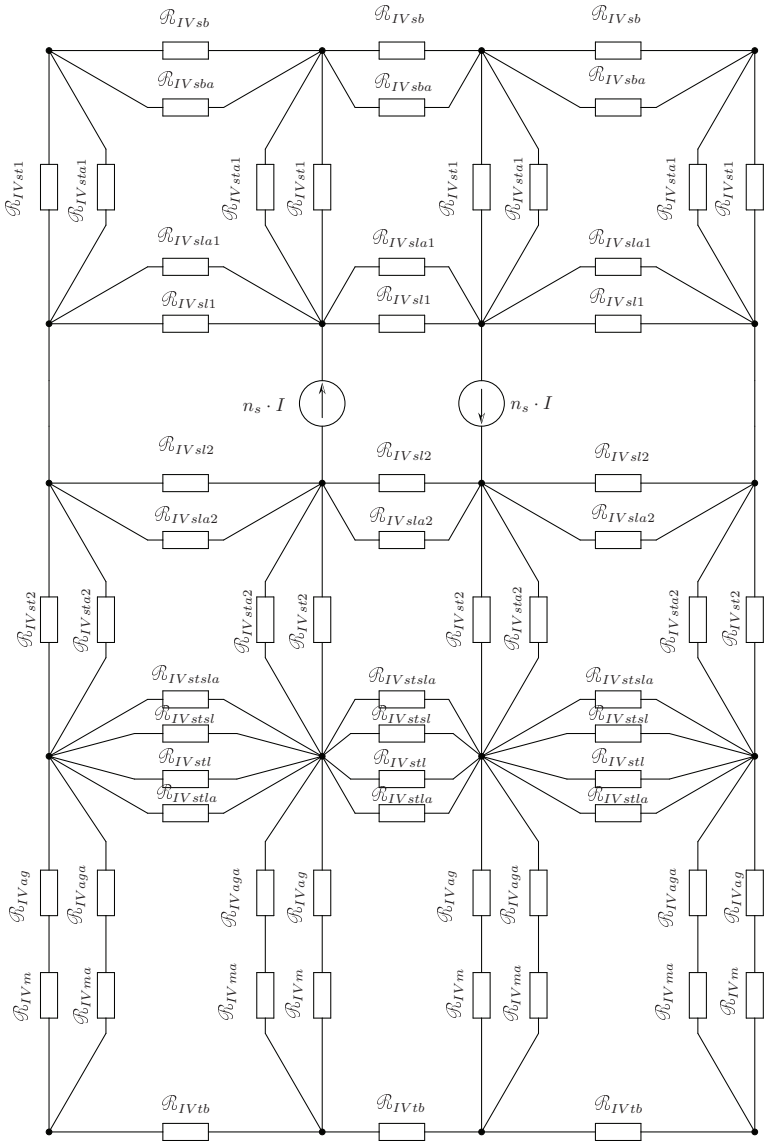

Figure 6.28: *3D armature reluctance network simplified into a grid network.*

would be even better with a more accurate discretization. However, this will also increase the number of reluctance elements which leads to more time consuming computations. For this purpose and in order to obtain results faster the two layer model is considered to be accurate enough.

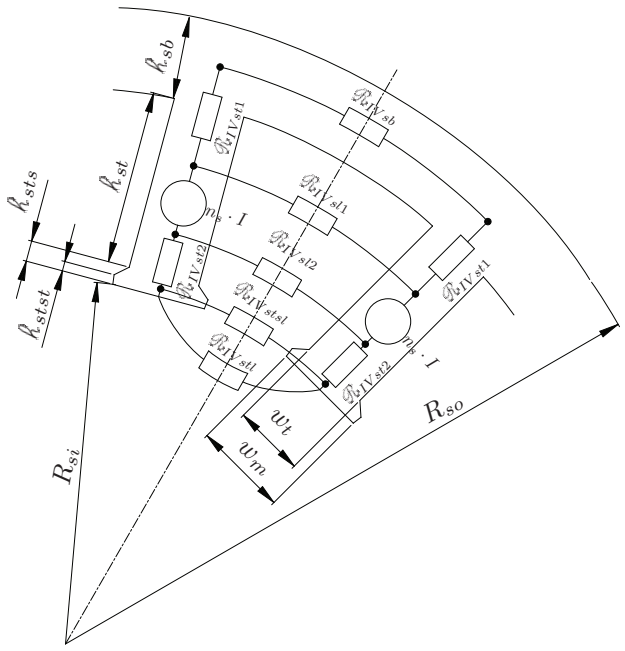

Figure 6.29: *Stator reluctance network with the provided dimensions.*

The upper part of the tooth reluctance can be calculated using

$$\mathcal{R}_{IVst1} = \frac{\frac{\ell_{st}+\ell_{sb}}{2}}{\mu_0 \cdot \mu_{ri} \cdot w_t \cdot \ell_m} \tag{6.71}$$

Similarly, the reluctance behind the stator tooth and between two stacks can be calculated from

$$\mathcal{R}_{IVsta1} = \frac{\frac{\ell_{st}+\ell_{sb}}{2}}{\mu_0 \cdot w_t \cdot (2 \cdot \tau_p - \ell_m)} \tag{6.72}$$

Although the lower part of the stator tooth (part of the tooth closer to the air gap) is not equally wide along its length, due to the stator shoe, it is for the sake of simplicity treated as one reluctance element. For this calculation the width of the stator tooth w_t is used. A small difference in the total reluctance would have a minor impact on the final result in the flux calculation. The tooth shoe will have a greater influence on the leakage reluctances, as described later in this chapter. Thus, the reluctance of the lower part of the stator tooth can be written as

$$\mathcal{R}_{IVst2} = \mathcal{R}_{IVst1} \tag{6.73}$$

In a similar way the reluctance between the two stacks can be written as

$$\mathcal{R}_{IVsta2} = \mathcal{R}_{IVsta1} \tag{6.74}$$

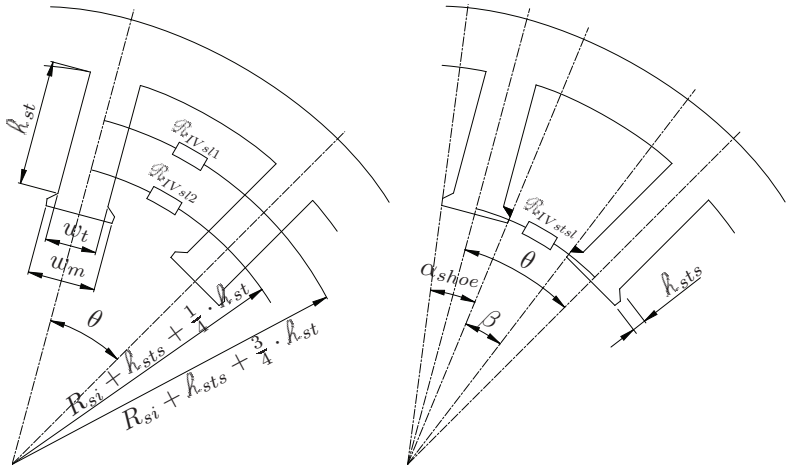

(a) (b)

Figure 6.30: *Leakage reluctance elements in the stator slot a) slot leakage reluctance elements and b) shoe leakage reluctance elements.*

In order to calculate the slot leakage reluctance the average length of the reluctance paths has to be calculated. The length of the upper part is calculated according to

$$\ell_{pa4} = \left(R_{si} + h_{sts} + \frac{3}{4} \cdot h_{st} \right) \cdot \theta - w_t \tag{6.75}$$

where θ is defined as shown in Figure 6.30(b).

In a similar way the length of the lower part of the slot leakage reluctance is calculated according to

$$\ell_{pa5} = \left(R_{si} + h_{sts} + \frac{1}{4} \cdot h_{st} \right) \cdot \theta - w_t \tag{6.76}$$

The slot leakage reluctances can now be calculated according to

$$\mathcal{R}_{IVsl1} = \frac{\ell_{pa4}}{\mu_0 \cdot \frac{h_{st}}{2} \cdot \ell_m} \tag{6.77}$$

and

$$\mathcal{R}_{IVsl2} = \frac{\ell_{pa5}}{\mu_0 \cdot \frac{\hbar_{st}}{2} \cdot \ell_m} \tag{6.78}$$

For the leakage reluctance in between two stator stacks the length of the path should be somewhat modified. The final slot leakage reluctances can then be written as

$$\mathcal{R}_{IVsla1} = \frac{\ell_{pa4} + w_t}{\mu_0 \cdot \frac{\hbar_{st}}{2} \cdot (2 \cdot \tau_p - \ell_m)} \tag{6.79}$$

and

$$\mathcal{R}_{IVsla2} = \frac{\ell_{pa5} + w_t}{\mu_0 \cdot \frac{\hbar_{st}}{2} \cdot (2 \cdot \tau_p - \ell_m)} \tag{6.80}$$

The leakage reluctance between the stator teeth shoes will to a large extent contribute to the stator leakage flux. That is why, it is treated separately from the two leakage reluctances described above. The shape of the tooth shoe is assumed to be rectangular. The calculation procedure is the same as above. At first, the length of the reluctance path is calculated according to the equation below

$$\ell_{pa6} = (R_{si} + \hbar_{stst}) \cdot \beta \tag{6.81}$$

where β is defined as shown in Figure 6.30(b).

The leakage reluctance can then be written as

$$\mathcal{R}_{IVstsl} = \frac{\ell_{pa6}}{\mu_0 \cdot \hbar_{sts} \cdot \ell_m} \tag{6.82}$$

The last reluctance is the tooth leakage reluctance. It is a part of the flux that enters the air gap but instead of going into the mover iron back it completes its path through the air into the neighboring tooth just outside the slot opening. However, one should be careful in associating all this flux as unusable or wasted. Some parts of this flux should be treated as the leakage because it never enters the magnets. However, the other parts or the majority of this flux will certainly contribute to the torque/force development in the machine. Based on the length of the air gap together with the height of the magnet the part of the useful flux can be determined.

An approximate flux path length is calculated as shown in Figure 6.31. The radius of the arc of the flux path is given according to the cosine theorem by the expression

$$R_{arc} = \sqrt{R_{si}^2 + R_{sh}^2 - 2 \cdot R_{si} \cdot R_{sh} \cdot \cos\left(\frac{\theta}{2}\right)} \tag{6.83}$$

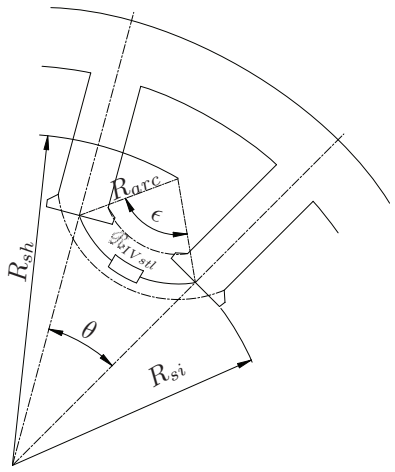

Figure 6.31: *Tooth leakage reluctance in the stator.*

where R_{sh} is calculated from

$$R_{sh} = R_{si} + h_{sts} + \frac{h_{st}}{2} \tag{6.84}$$

The angle of the flux path arc is calculated as

$$\epsilon = 2 \cdot \arcsin\left(\frac{\sin\left(\frac{\theta}{2}\right) \cdot R_{si}}{R_{arc}}\right) \tag{6.85}$$

The length of the arc can then be calculated according to

$$\ell_{pa7} = R_{arc} \cdot \epsilon \tag{6.86}$$

Finally, the reluctance for the tooth leakage flux is given by

$$\mathcal{R}_{IVstl} = \frac{\ell_{pa7}}{\mu_0 \cdot w_t \cdot \ell_m} \tag{6.87}$$

It can be noted from Eq. (6.87) that the calculation of the reluctance, instead of the width of the tooth shoe or the width of the magnet, the width of the stator tooth has been used. It is believed that the overall length of the flux path, that is the length of the arc in Figure 6.31 is somewhat underestimated, as it is slightly shorter than its actual length. Therefore, a smaller width for the flux path has been used in order to compensate for the shorter length which in the end will give a good approximation of the true reluctance.

The leakage reluctance in the area between two stator stacks is given in a similar way

$$\mathcal{R}_{IVstla} = \frac{\ell_{pa7}}{\mu_0 \cdot w_t \cdot (2 \cdot \tau_p - \ell_m)} \tag{6.88}$$

The last three reluctances seen by the armature flux are the reluctance of the air gap, reluctance of the magnet and the reluctance of the iron in the mover back see Figure 6.32. It is assumed that the relative permeability of the magnets is unity, i.e the magnets have the same permeability as air. Although, this in reality is not the case, this assumption has little influence on the results. The relative permeability of the magnets is usually very low and for NdFeB magnets it is about 1.05 which is very close to the assumed value.

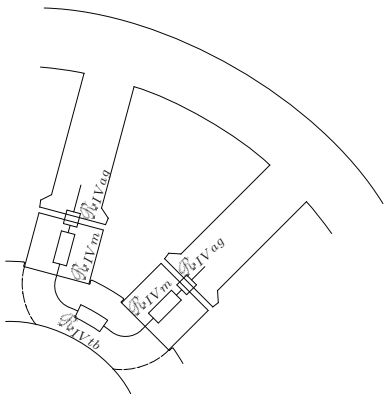

Figure 6.32: *Air gap, magnet and translator reluctances in the machine.*

Due to the above assumption there will be no difference in the reluctivity of air and that of the magnets as seen by the flux from the stator. However, both reluctances are treated separately in the analysis. The air gap reluctance can be written as

$$\mathcal{R}_{IVag} = \frac{\delta}{\mu_0 \cdot w_m \cdot \ell_m} \tag{6.89}$$

The reluctance between two stator stacks is given by

$$\mathcal{R}_{IVaga} = \frac{\delta}{\mu_0 \cdot w_m \cdot (2 \cdot \tau_p - \ell_m)} \tag{6.90}$$

where g is the length of the air gap and w_m is the width of the magnet. The magnet reluctance can be calculated according to

$$\mathcal{R}_{IVm} = \frac{\hbar_m}{\mu_0 \cdot w_m \cdot \ell_m} \tag{6.91}$$

The length of the magnet can vary freely, from 100% pole pitch length and downwards. The effect of different magnet lengths has been investigated in more detail in [48]. In the prototype the ratio of the magnets length and the pole length is $\frac{2}{3}$. Thus, the flux from the armature reaction, as it goes from the stator to the mover iron back will see not only the magnet but also some other material that is filling the space between the magnets. In the prototype machine, this space is filled with a special mixture of epoxy material. However, due to the assumption of the magnets relative permeability, the reluctivity will be the same for both the magnets and the epoxy mixture.

The reluctance of the magnet and the reluctance of the epoxy will therefore be lumped together and treated as one. This reluctance can then be written as

$$\mathcal{R}_{IVma} = \frac{\ell_m}{\mu_0 \cdot w_m \cdot (2 \cdot \tau_p - \ell_m)} \tag{6.92}$$

In the mover back there will therefore be no difference in reluctances just under the stator teeth and between the stator stacks. The mover back is made of iron and reluctance seen by the stator flux is given by

$$\mathcal{R}_{IVtb} = \frac{\left(R_{ti} + \frac{\ell_{tb}}{2}\right) \cdot \theta}{\mu_0 \cdot \mu_{ri} \cdot 2 \cdot \tau_p} \tag{6.93}$$

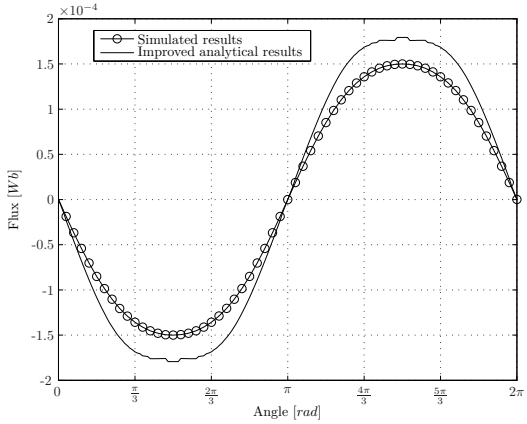

Figure 6.33: *Comparison of FEM-simulated and analytical results for the flux in the back of one stator stack.*

Analytical and simulated results for armature reaction field are shown in Figure 6.33. As can be seen from the figure the agreement between the results is acceptable.

6.6 Power Factor

The common problem for the most of the TFM is the relatively low power factor. This will have a direct impact on the size of the inverter as the inverter rating is inversely proportional to the power factor. In modern drives the current vector can be placed arbitrarily in different positions. By placing the current vector in the position between the induced voltage and the terminal voltage, the value of the power factor can be improved. However, in surface mounted permanent magnet machines where the values of inductance in 'q' and 'd' direction are almost the same, i.e there is no reluctance force contribution, the force production would decrease. This assumes that the magnitude of the current vector is kept constant at a level where the thermal limit due to the ohmic losses in the electrical machine is reached.

Figure 6.34 shows the different control strategies.

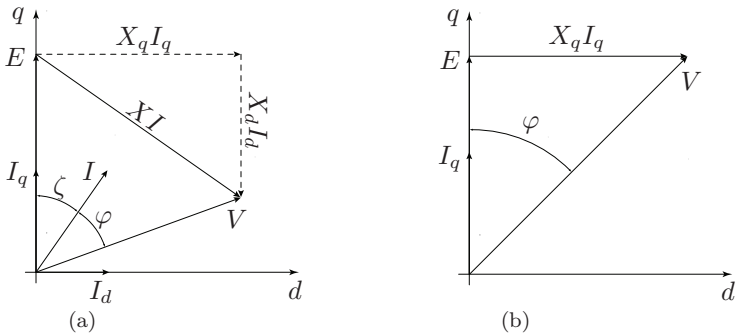

Figure 6.34: *Phasor diagram in a synchronous generator a) $\varphi = \zeta$ and b) with only q current.*

The problem with the power factor in a TFM has been investigated in [31]. In order to have a simple comparison of different machines, the current vector is placed in the phase with the induced EMF. Assuming the resistance in the machine to be negligible, the power factor in TFM can be determined from a simple ratio between the '*stator peak flux from the armature acting alone*' and the '*stator peak flux from the magnets acting alone*':

$$pf = \cos\left[\arctan\left(\frac{\hat{\phi}_{NI}}{\hat{\phi}_{mag}}\right)\right] \tag{6.94}$$

This equation is used to calculate the power factor in the machine both from the FEM-analysis and from the values obtained from the improved analytical model. In the simplified model the power factor is calculated with the following equation

$$pf = \cos\left[\arctan\left(\frac{X_q \cdot I_{phase}}{E}\right)\right] \tag{6.95}$$

The calculated values from the different analytical models are presented in Table 6.4.

Table 6.4: *Power factor for the TFM.*

	Simplified anal.	**Improved anal.**
pf	0.7131	0.3817

As can be seen, the result from these models differ by factor of two. This is mainly due to the underestimated leakage in the simplified model, whereas the induced voltage in the machine is much higher than in reality. These values will be compared with the FEM-simulated values in the next chapter.

6.7 Cogging Force

Cogging force in an electrical machine generates losses, it is also a source of tooth vibration and motor noise. In the free piston energy converter the cogging force is not as critical as in other applications, due to the existence of high average forces during acceleration [14]. However, in order to get an optimal machine design the cogging force should be minimized.

The FPEC can be used in many different areas, e.g. as a stand alone generator unit on a farm. Its purpose, in this study, is to be used as a generating unit in an electric vehicle. As mentioned above, cogging force is one of the sources of noise in the machine and in vehicle application low noise is an essential requirement. Although the combustion itself may generate more noise, the system design should be optimized with respect to the total noise of the system.

The two following methods are proposed in this study to investigate the cogging force: conformal mapping and relative permeance model [49, 50]. Both methods are based on the flux density distribution on the side of the tooth. Once the flux density distribution is known, by using the magnetic pressure integration, the cogging force can be calculated.

6.7.1 Relative permeance model

Usually the cogging torque/force is calculated using the energy method. However, due to the geometry of the machine, calculations of the permeance and final calculations of the rate of change of energy is a tedious task. In [50]

an alternative analytical method to calculate the cogging force is proposed. It is based on an analytical calculation of the air gap field distribution.

According to the proposed method in [50] some of the assumptions needed, in order to simplify the magnetic field calculations are:

- the iron material is assumed to be ideal i.e. $\mu_i = \infty$.
- the flux density distribution, on the side of the tooth is determined from the product of the flux density produced by the magnets and the relative permeance.
- the flux density in the air gap is assumed to have a square wave shape.
- the flux that crosses the air gap is assumed to follow a straight line just above the magnet and a circular line, centered about the corner of a tooth, see Figure D.2.

As illustrated in Figure 6.35(a), the flux density in the air gap is assumed to has a square wave shape. Analytically the flux density is expressed using the Fourier series expansion according to Eq. (6.96). The flux density expressed by the Fourier series, which is also used in the analysis below, is shown in Figure 6.35(b).

$$B_{mag} = \sum_{n=1}^{\infty} \frac{2B_m}{\pi n} \cdot (\cos(n\varpi) - \cos(n\pi - n\varpi)) \cdot \sin\left(n\pi\left(\frac{z_e}{\tau_p}\right)\right) \quad (6.96)$$

where z_e position along the translator axis and ϖ is given by

$$\varpi = \frac{\ell_m}{2\tau_p} \cdot \pi \quad (6.97)$$

According to the theory, the reluctance pressure on the boundary between two regions [49], is given by

$$p_R = \frac{1}{2} \cdot (\mu_2 - \mu_1) \cdot \left(\frac{B_n^2}{\mu_1 \cdot \mu_2} + H_t^2\right) \quad (6.98)$$

At the boundary the normal component of the magnetic induction B_n and tangential component of the magnetic field strength H_t are constant. Furthermore, if the permeability difference between the two boundary regions is large, $\mu_2 \gg \mu_1$, then $H_t = 0$. Eq. (6.98) then can be expressed as

$$p_R = \frac{B_n^2}{2\mu_1} \quad (6.99)$$

The force equation is derived by integrating of the reluctance pressure over the surface.

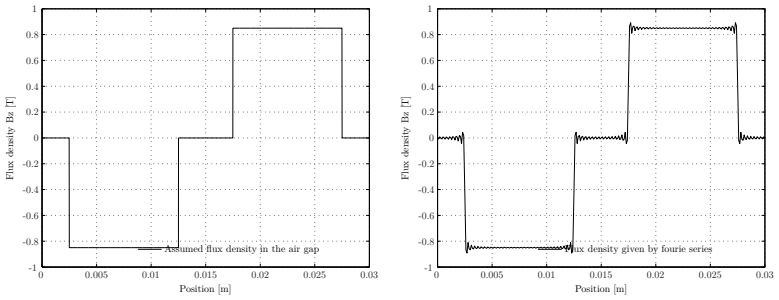

(a) (b)

Figure 6.35: *a) Assumed flux density in the air gap, b) Assumed flux density given by Fourier series.*

$$\vec{F} = \int_S p_R d\vec{S} \tag{6.100}$$

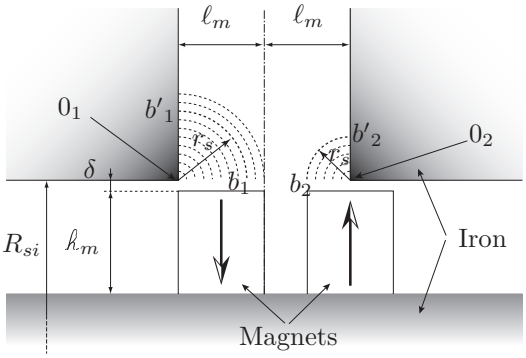

Figure 6.36: *Idealized flux path used for calculation of the permeance.*

The cogging force is calculated by assuming that the flux density distribution on the sides of the teeth (which is perpendicular to the direction of translator motion, between the stator stacks) $B'_{t_{b1}}$, is the same as the flux density distribution in the air gap above the magnet $B_{r_{b1}}$. The only flux density that is of interest, for the calculation of the cogging force is between the stator stacks. This flux is given by

$$B_{r\ \mathrm{at}\,R_{si}} = B_{mag} \cdot \widetilde{\vartheta} \tag{6.101}$$

According to the assumptions above the permeance per unit area ϑ and relative permeance per unit area $\widetilde{\vartheta}$ are given by Eq. (6.102).

$$\begin{cases} \vartheta &= \frac{\mu_0}{\delta+\frac{k_m}{\mu_m}+\frac{2\cdot\pi\cdot r_s}{4}} \\ \widetilde{\vartheta} &= \frac{\vartheta}{\left[\frac{\mu_0}{\delta+\frac{k_m}{\mu_m}}\right]} \end{cases} \tag{6.102}$$

The net cogging force for one phase in any translator position is given by

$$\begin{aligned} F_{cog} = \quad & n_{stack} \cdot \sum_{k=1}^{q_s/3} w_t \int_{toothside} \left(\frac{B'^2_{t_{b1}} - B'^2_{t_{b2}}}{2 \cdot \mu_0} \right) \mathrm{d}y \\ = \quad & n_{stack} \cdot \sum_{k=1}^{q_s/3} w_t \int_0^{\ell_{mag}} \left(\frac{B^2_{r_{b1}} - B^2_{r_{b2}}}{2 \cdot \mu_0} \right) \mathrm{d}r_s \end{aligned} \tag{6.103}$$

Figure 6.37 illustrates the obtained results for one phase.

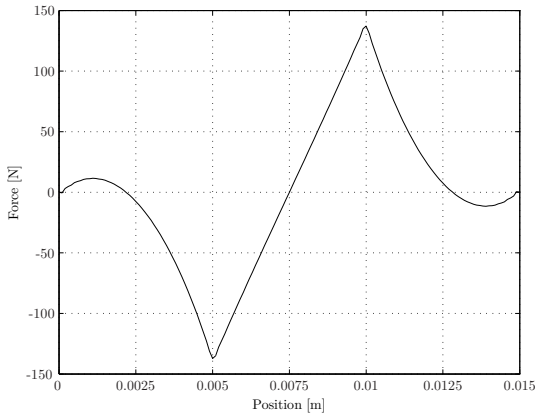

Figure 6.37: *Cogging force in one phase with the original assumption on the relative flux path.*

Due to the relatively large distance between the adjacent stator stacks, the direction of the cogging force is shifted several times during one pole pitch displacement of the translator. As would become evident later, the assumption in the relative permeance model, that the flux follows a circular path centered about the corner of the tooth, has to be modified. It can only be applied if the slot openings are narrow, as compared to the pole length. In the case studied here one magnet can be in the middle of the two stacks and will therefore have no iron tooth just above it. The flux from the magnet that enters the side of the teeth will then no longer travel only in a circular path but more in an elliptical path. In an attempt to

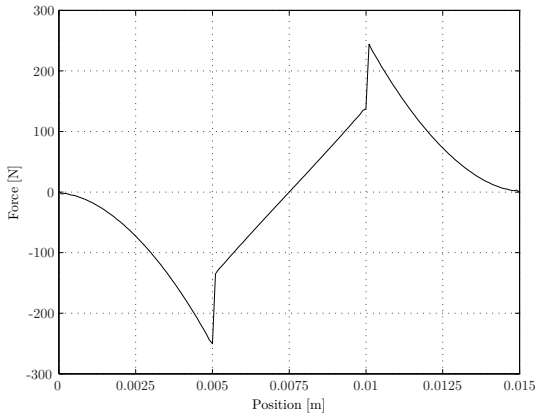

Figure 6.38: *Cogging force for one phase in the machine with the new assumption on the relative flux path.*

improve the model a new assumption of the relative flux path has been made where only a part of the flux that is very close to the stator tooth is allowed to follow a circular flux path. The rest of the flux will follow a linear reluctance path which is the distance between the magnet and the stator tooth. Figure 6.38 illustrates the results from the calculation for one phase from the model with the new assumptions.

The resultant cogging force in the machine is observed by the sum of all three phases, where the force curves for phase 'b' and 'c' has been shifted in the axial direction by 120 and 240 electrical degrees respectively. The results from the calculations of cogging forces in all three phases are illustrated in Figure 6.39(a) and the total cogging force is shown in Figure 6.39(b). However, due to the wide space between the stacks, the assumptions of different relative reluctance paths together with the assumption of the square wave flux density in the air gap does not give a true picture of the actual flux density along the sides of the stator teeth. Thus the results from this method will at best only give a hint to the cogging force magnitude. In order to calculate the cogging force more accurately, the flux density distribution along the stator teeth sides needs to be determined more accurately.

6.7.2 Conformal Mapping CM

Conformal Mapping (CM) is a powerful analytical method, which is very helpful in the determination of the 2D magnetic fields. The idea of conformal mapping is to simplify a complex geometry into a simple one, where the field easily can be calculated. The CM method has its roots in complex

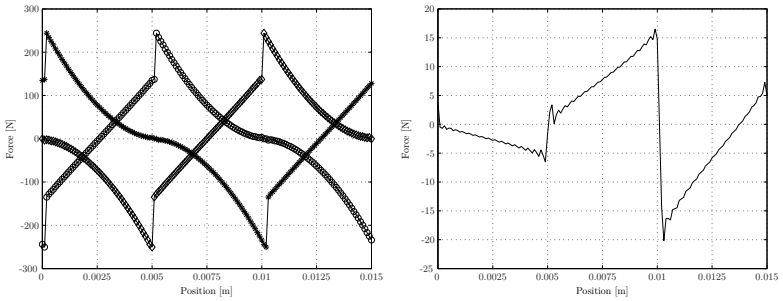

(a) (b)

Figure 6.39: *Cogging force with the new assumption on the relative flux path a) Cogging force for different phases in the machine b) Total cogging force in the machine.*

analysis. The complex geometry is placed in the complex plan 'z' where an analytical complex function $z = f(w)$, called the CM, is applied. This function will map lines, or points, into the new configuration placed in the new complex plane w.

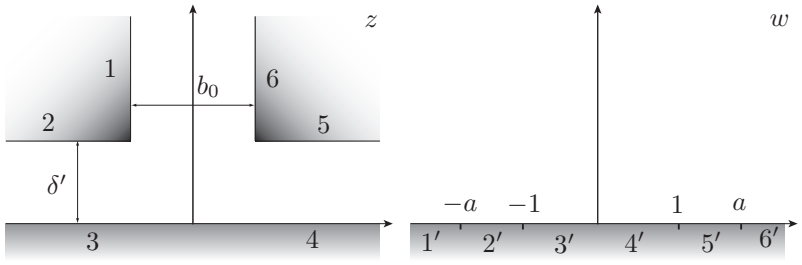

(a) (b)

Figure 6.40: *Simplified TFM configuration in a) z-plane b)w coordinate system.*

It is also possible to perform several CM in a row until a simple enough configuration is obtained. According to [49] the geometry shown in Figure 6.40(a) can be mapped into the new geometry shown in Figure 6.40(b) with the following

$$z = \frac{b_0}{\pi} \cdot \left[\arcsin\left(\frac{w}{a}\right) + \frac{\delta'}{b_0} \cdot \ln\left(\frac{\sqrt{a^2 - w^2} + \frac{2 \cdot \delta'}{b_0} \cdot w}{\sqrt{a^2 - w^2} - \frac{2 \cdot \delta'}{b_0} \cdot w} \right) \right] \tag{6.104}$$

where

$$a = \sqrt{1 + \left(\frac{2 \cdot \delta'}{b_0}\right)} \tag{6.105}$$

and

$$\delta' = \delta + \frac{h_m}{\mu_{rm}} \tag{6.106}$$

However, the transformation function does not give the required field distribution. The cogging force comes from the fields produced by the magnets. In order to obtain the required field distribution, the source of the field, i.e. the magnets has to be transformed into a new system where the field is easily calculated. One way to transform the magnets into the new system is to describe the magnets in the original system with the help of surface currents [51].

Equivalent current model

For modern magnetic materials the B-H characteristic in the second quadrant is a straight line [44]. It is given by

$$B = B_r + \mu \cdot H = B_r + \mu_0 \cdot \mu_r \cdot H \tag{6.107}$$

The magnetization is given by

$$M = \frac{B_r}{\mu_0} + (\mu_r - 1) \cdot H \tag{6.108}$$

For the NeFeB magnets the relative permeability varies between 1.03-1.07. In order to simplify the calculations, the relative permeability μ_r,is assumed to be exactly 1. By choosing the relative permeability as 1 the second term in Eq. (6.108) disappears, and the magnetization is constant for the whole PM body regardless of the field, so the equation becomes:

$$M = \frac{B_r}{\mu_0} \tag{6.109}$$

It is possible to represent the magnetic field produced by the magnets with the equivalent currents. According to [49], a magnet with magnetization $\vec{M}$ can be replaced by a system of two equivalent currents.

- The volume current with the density $\vec{J} = \nabla \times \vec{M}$
- The surface current with the density $\vec{J_s} = \vec{M} \cdot \vec{n}$, where $\vec{n}$ is a unit vector normal to the body surface.

These currents are placed in air. Because the PM magnetization in the magnet is constant, the volume current density is thus zero.

The magnetic field can then be represented by the equivalent surface currents that flows on the lateral sides of PM poles, where the vectors $\vec{M}$ and $\vec{n}$ are in the normal direction to the direction of motion. From this follows that the equivalent surface current density is $J_s = \pm M$ and the total current flowing on the lateral side is [49]:

$$I = J_s \cdot \hbar_m = \pm M \cdot \hbar_m \tag{6.110}$$

In order to obtain the punctual currents, each of the surface currents is divided into the n punctual currents, where $n = INT(\hbar_m)$. This is illustrated in Figure 6.41.

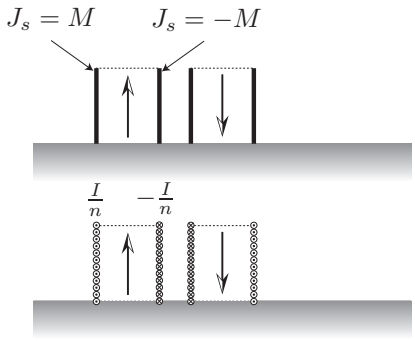

Figure 6.41: *Equivalent PM punctual currents.*

It is now possible to transform all punctual currents into a new 'w' system where the magnetic field strength is easily calculated by applying the method of images. The method states that the magnetic field is a result of the summation of two fields, the applied field with the source in region with permeability μ_1 and the field from the image source in the region with permeability μ_2. The image source should be placed symmetrically on the opposite side of the boundary region and has the value of $I_{image} = I \cdot \frac{\mu_2 - \mu_1}{\mu_2 + \mu_1}$. However, assuming the permeability of the magnetic region as infinite or much higher then the first region i.e. $\mu_2 \gg \mu_1$, it can be understood that the image and the applied source will have the same value of the current. Figure 6.42 shows a conductor with the current I above an infinite iron plane together with the image source.

The example of a conductor with a current I placed at a point $\{x_p, y_p\}$ above an infinitely long iron plane and applying Ampere's law, the magnetic field components at an arbitrary point $\{x, y\}$ is given by

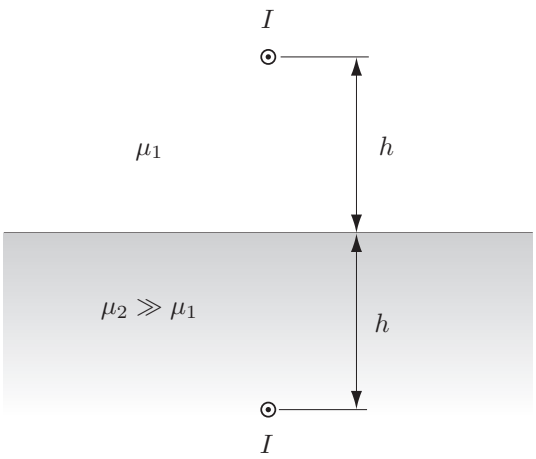

Figure 6.42: *The conductor with the current (applied field) in magnetic media with permeability μ_1 and the image of the conductor in a magnetic media with permeability μ_2.*

$$H_x = -\frac{I}{2\pi} \cdot \frac{y - y_p}{(x - x_p)^2 + (y - y_p)^2} \tag{6.111}$$

and

$$H_y = \frac{I}{2\pi} \cdot \frac{x - x_p}{(x - x_p)^2 + (y - y_p)^2} \tag{6.112}$$

Introducing the complex field strength the value of the magnetic field is given by

$$H_w = H_x + \jmath H_y = \frac{I}{2\pi} \left[\frac{1}{(z - z_p)^*} + \frac{1}{\left(z - z_p^*\right)^*} \right] \tag{6.113}$$

where $z = x + \jmath y$ and $z_p = x_p + \jmath y_p$ $\left(z_p^* = x_p - \jmath y_p\right)$.

Once the magnetic field is calculated in 'w' coordinate system it has to be transformed into a original coordinate system 'z' before the force on the side of the teeth can be calculated. This transformation is given by

$$H_z = H_w \cdot \left(\frac{\partial w}{\partial z} \right)^* \tag{6.114}$$

With the knowledge of the magnetic field strength in the 'z' coordinate system, it is possible to calculate the force that acts on the side of the stator stack.

In [51] it has been shown that the reluctance force can be derived from Maxwell's stress force. The cogging force acting on one stator tooth is calculated by Eq. (6.115). The cogging force is mostly acting on the sides of the teeth between two stator stack but also on the teeth front. The surface of integration is composed of four different surfaces, Figure 6.43.

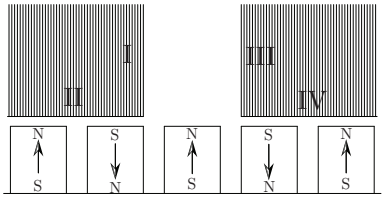

Figure 6.43: *Four different surfaces of integration.*

$$\vec{F} = \int_{I+II+III+IV} p_R d\vec{S} \tag{6.115}$$

In order to solve the equation above a numerical integration is performed.

A simple 2D-FEM model has been developed and simulated, see Figure 6.44(a) in order to verify the model described above. The simulation model includes only two magnets as shown in the figure. The analytical result and the results obtained from the simulation are illustrated in Figure 6.44(b).

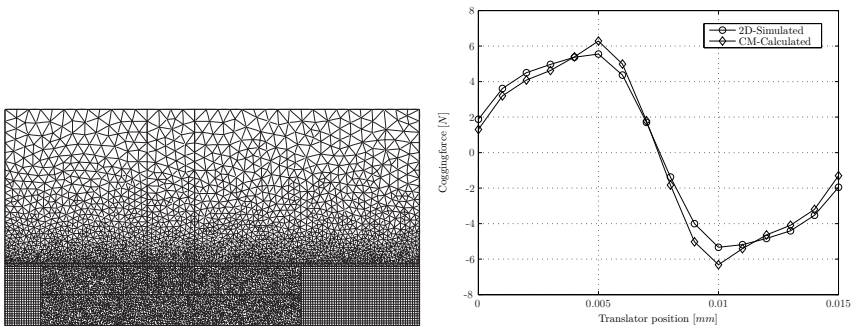

(a) (b)

Figure 6.44: *Validation of the CM model a)2D-FEM geometry and b) result comparison.*

As can be seen the agreement between the results is very good. The discrepancy in the results can be explained by the mesh density in the FEM model and by the density of punctual currents representing the magnet.

The number of punctual currents representing one magnet is chosen as equal to 12. As the magnets are relatively high, ca 12 mm the space between the currents is about one mm. In order to improve the agreement of the results, the number of punctual currents has to be increased to at least twice. However, for the purpose of the final analysis the model was considered as accurate enough.

The final goal of the analysis is the calculation of the cogging force in the prototype. The analytical results are compared with the results obtained from the 3D-FEM simulations. As the 3D-FEM model has the periodic boundary conditions on the sides (a more detailed explanations is given in the next chapter) the CM model has been solved with 5 magnets. This is done in order to have a continuity as it is the case in the 3D-FEM model which in the end will result in a better agreement of the results.

Figure 6.45(a) shows the analytical and 3D-FEM simulated results for only one row of magnets in the machine. As can be seen from the results, the amplitudes of the force ripple does not agree very well. However, the shapes of the curves have a better agreement. In the analytical results only two dimensions are considered. Usually, in order to reduce an analysis to a two dimensional case, the third dimension is assumed to be infinitely long or in some other way does not significantly interfere with the results of the two dimensional analysis. As the magnets in the prototype machine are only 14 mm thick and the stator teeth are only 11 mm long the end effects will have an impact on the results. This can explain the difference in the results, as in the 3D-FEM simulations all effects are included as all three dimensions are present.

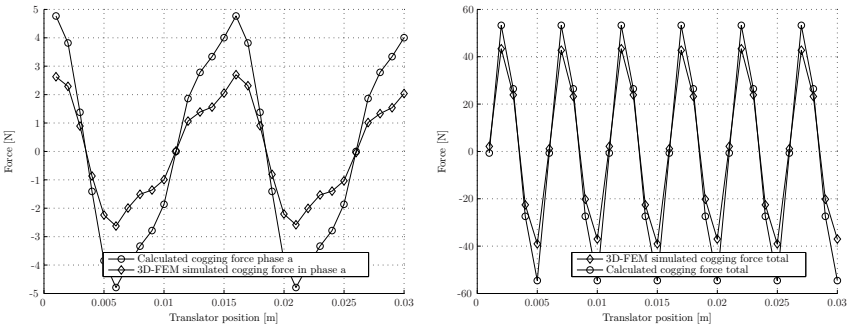

(a) (b)

Figure 6.45: *Cogging force as a function of the mover position analytical and simulated results a) for one and b) for three phases respectively.*

The results for the total cogging force in the machine are obtained by shifting the one phase results by 120 and 240 electrical degrees for the

other two phases respectively. The total cogging force is the sum of the contributions of all phases. The results for the total cogging force are shown in Figure 6.45(b). Although the amplitudes in the results are still different, the agreement is better compared with the results for only one row.

6.8 Conclusions

In this chapter different models for the analysis of the novel TFM machine are presented. The simplified model which has been used in the design of the prototype clearly underestimates the leakage flux in the machine. There was a natural need for a better model to obtain a better agreement which resulted in the improved analytical model. The results from this model has shown much better agreement with the simulated results. Still, there is a slight disagreement in the result comparison. However, these discrepancies can probably be eliminated with the improvement of different reluctance paths.

The cogging force in the machine is calculated with the method of Conformal Mapping. This method is a powerful tool to calculate the magnetic field in a complex geometry. It is mainly used in the 2D analysis, which to some extent is also reflected in the results. The comparison between the results obtained from the CM method and the 3D-FEM simulations shows disagreement in the amplitude. However, the shape of the curves is in better agreement. This indicates that the effects in the third direction does have an impact on the results and cannot be totaly neglected.

Chapter 7

3D-FEM simulations

This chapter will describe the model of the novel TFM used in the FEM simulations. The results obtained from the simulations will be compared with the analytical results.

7.1 Introduction

The Finite Element Method has become an important tool in the design and analysis of electrical machines. It is used both as a complement to the analytical analysis but also as a major design tool for different tasks. The evolution progress of the hardware has been followed up by the different software packages that are easy to use and thereby offer quick access to the results.

Today there exist several different software packages that are capable of performing both 2D- and 3D-FEM analysis. In the following analysis the software package Flux-3D by Cedrat is used. This package offers both 2D and 3D-analysis.

7.1.1 2D-FEM limitations

In 2D-FEM analysis the 3rd dimension is assumed to be infinite and quantities such as flux, currents etc are assumed to be invariant in this direction. In order to simplify the geometry even further, it is desirable to identify the periodic or symmetric boundaries where adequate boundary conditions can be applied. Thus, the time required for the simulation can be reduced. In a conventional rotary radial flux machine it is often assumed that the flux density along the length of the machine does not vary. It is then not possible to identify and analyze the end effects in the machine. However, if the length to bore diameter ratio is large, end effects in the machine can

normally be neglected, unless forces on the end windings in for example large synchronous machines are to be calculated.

Conventional linear machines are often considered as axi-symmetrical where i.e. the flux density variation in the circumferential plane is assume to be negligible. Here it is sometimes possible to identify situations when end effects should be taken into consideration.

In the examples given above the movement and the winding layout lie in planes perpendicular to each other while in a TFM these two lie in the same plane. Hence, for a TFM machine, it is difficult to calculate the force from a 2D-FEM analysis.

Another important issue is the investigation of the leakage flux in the machine. The pole to pole leakage flux in the TFM is one of the important phenomena that must be taken into consideration. As this leakage occurs in the '3:de' dimension it is difficult or impossible to perform accurate analysis using simply a 2D-FEM model.

7.1.2 3D-FEM analysis

Due to the limitations of 2D-FEM mentioned above, most of the analysis are therefore performed with 3D-FEM. Certain problems were encountered in the beginning of the project. The model that was built in the software did not converge and it was not possible to obtain any results. In the beginning it was believed that the way the model was built was the reason behind the convergence problem. The approach in the second model was to enable the mesh generation in a different way. This model shared the same faith as the first and no convergence could be obtained. However, these issues were solved as the software developed.

Both dynamic and static simulations are performed in the following analysis.

7.2 Simulated geometry

The simulated segment of the machine geometry is shown in Figure 7.1. Thanks to the periodicity in the machine it is sufficient to simulate only one pole pair. Periodic boundary conditions are placed on the upper and the lower sides of the segment. These conditions require that the mesh on these two sides are exactly the same. There are different ways to achieved the desired geometry together with the adequate boundary conditions. The approach chosen here is considered not only to be simple to draw but also to have some advantages in the post processing.

The model is simulated with a non-meshed coil, MA600-50 steel and the relative permeability of the magnet is set to 1.05. As the non-meshed coil is not a part of the geometry it can be defined after the geometry is

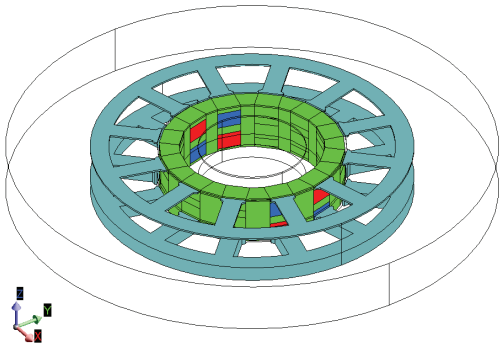

Figure 7.1: *3D Simulated model.*

finished. Hence, the model becomes more flexible. An advantage of the non-meshed coil is that it allows for automatical calculation of the total flux despite the fact that only a part of the machine is simulated. However, due to the periodic boundary conditions, this option is not accessible in the simulated model. Instead, the total flux is calculated by multiplying the value obtained by the number of stacks in the machine. End effects are therefore not considered in these analysis.

3D-FEM model was developed in two stages. The first stage was the static simulation model. Once the results were obtained from this, the model was further developed and adopted for dynamic simulations in the second stage. The mesh density of the model is shown in Figure 7.2.

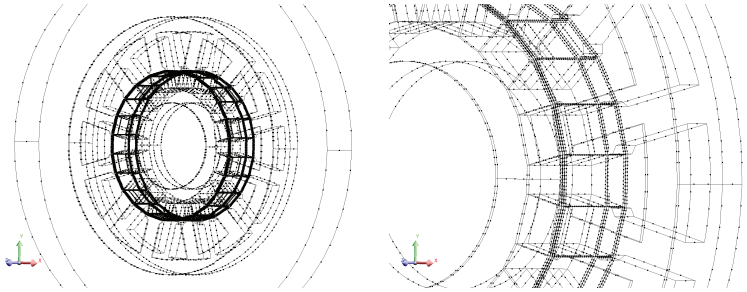

(a) (b)

Figure 7.2: *Density of mesh points in the simulated model a) density of the mesh points in the whole model b) Closer view of the mesh density close to the air gap.*

7.3 Flux

As mentioned above, the static simulations were carried out first. These simulations are used to investigate the flux densities and fluxes in the different regions of the machine. The prototype machine is designed using the simplified analytical model with the requirement of $\hat{B}_\delta = 0.85$T which is the flux density in the air gap, $B_{sb} = B_{st} = B_{tb} = 1.4$T in the stator back, stator teeth and translator back respectively. The flux density in the air gap is shown in Figure 7.3. As can be noted from the figure the peak

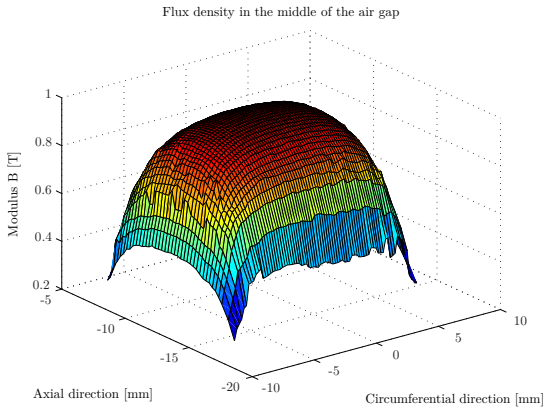

Figure 7.3: *Flux density in the air gap under one stator tooth.*

value of the flux density in the air gap is somewhat higher compared with the analytically calculated value. There are two reasons for this, the first is the assumption of the equivalent air gap explained earlier in chapter 6. The other reason is due to the fact that only the fundamental component of the flux density is considered in the design procedure. Although the flux density in the air gap is higher compared with the analytical results the question is if the machine can take advantage of this in the best possible way. Further investigation of the flux density in different regions of the machine, however, showed a large leakage flux. Only a fraction of the flux available in the air gap ended up as useful flux.

7.3.1 Leakage flux

Figure 7.4 shows the grids used in the 3D-FEM model for the investigation of the flux density in different parts of the machine. As shown in the figure the flux density is determined at six different locations: stator back, translator back, end of the stator tooth, beginning of the stator tooth, beginning of the stator tooth shoe and in the middle of the air gap. Regarding the no

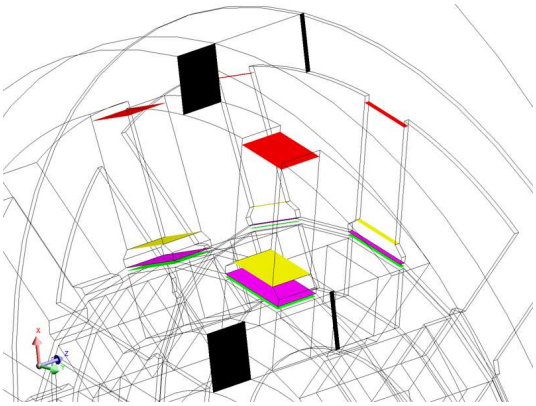

Figure 7.4: *2D grids in Flux3D software for the investigation of the flux density in different machine parts.*

load EMF, the most interesting parameter which defines the useful flux is the flux density in the stator back or at the end of the stator tooth. This flux density together with the flux density in the air gap will give a hint on the magnitude of leakage that is present in the machine.

Looking at the results shown in Figure 7.5, having in mind that the machine has been designed with the selected flux density value of 1.4T in the stator tooth and the stator back, a certain leakage of the flux can be observed. Figure 7.5(a) shows the flux density just inside the stator tooth shoe. As can be seen from the figure the maximum flux density is about 0.95T. Furthermore, from Figure 7.5(b) it can be noted that, though the area of the tooth is smaller the value of the flux density is also smaller, which indicates a leakage flux. Looking at the value of the flux density at the end of the stator tooth in Figure 7.5(c) a further reduction of flux density can be noted. Despite the fact that the analytical design method predicted a flux density of 1.4 T in the stator tooth and in the stator back, it is evident that only a fraction of this flux is available. This indicates a weakness in the magnetic design of the machine.

In order to have a better understanding of the cause of the leakage, two additional simulations are preformed. In the first simulation, only the magnets in phase 'a' are active. In the second simulation the model is simplified even further as only the magnets in phase 'a' under the stator teeth i.e each second pole in phase 'a' were active.

Only magnets in phase 'a'

As mentioned, in this simulation only magnets belonging to the phase 'a' are active, the rest of the magnets are turned off. It is interesting to

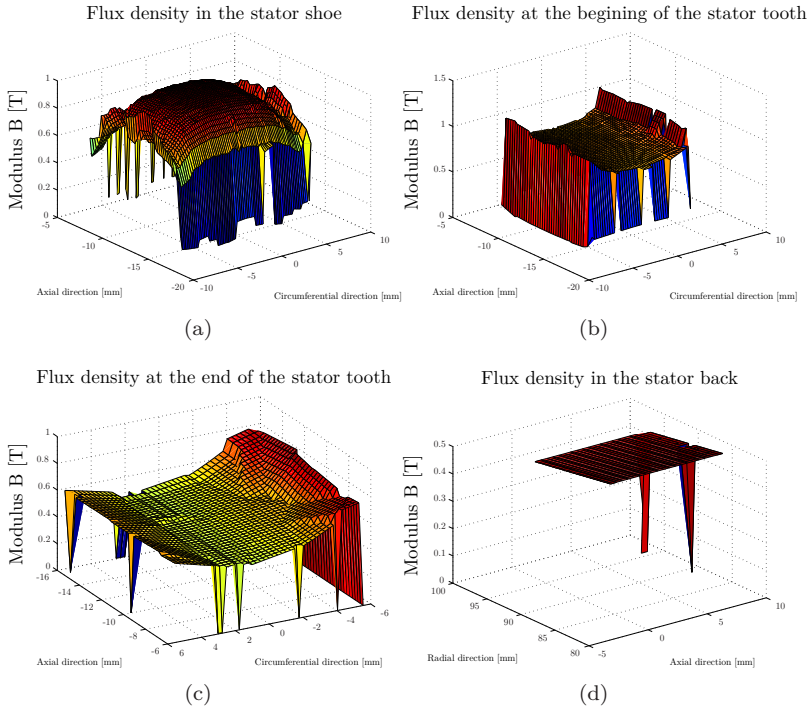

Figure 7.5: *Flux densities in different regions of the machine: a) just inside the stator tooth shoe, b) at the beginning of the stator tooth, c) at the end of stator tooth and d) in the stator back.*

investigate the interference of the magnetic circuits belonging to different phases, and its effects on the flux densities in the machine. Figure 7.6 shows flux densities in different regions of the machine. Results in Figure 7.6 can be compared with the results in Figure 7.5. As can be seen there is no significant difference between these results. Figure 7.6 indicates a slight decrease in the flux density, however, this decrease is of minor importance. There must be another phenomenon that gives rise to the large leakage of flux.

Only active magnets in phase 'a'

Further investigation includes only magnets that contribute to the useful flux. In other words magnets belonging to phase 'a' in each second pole are turned off. Figure 7.7 shows the simulation results. From these results it is evident that the flux densities in different regions change dramatically. The flux densities are more close to the values chosen and calculated in the

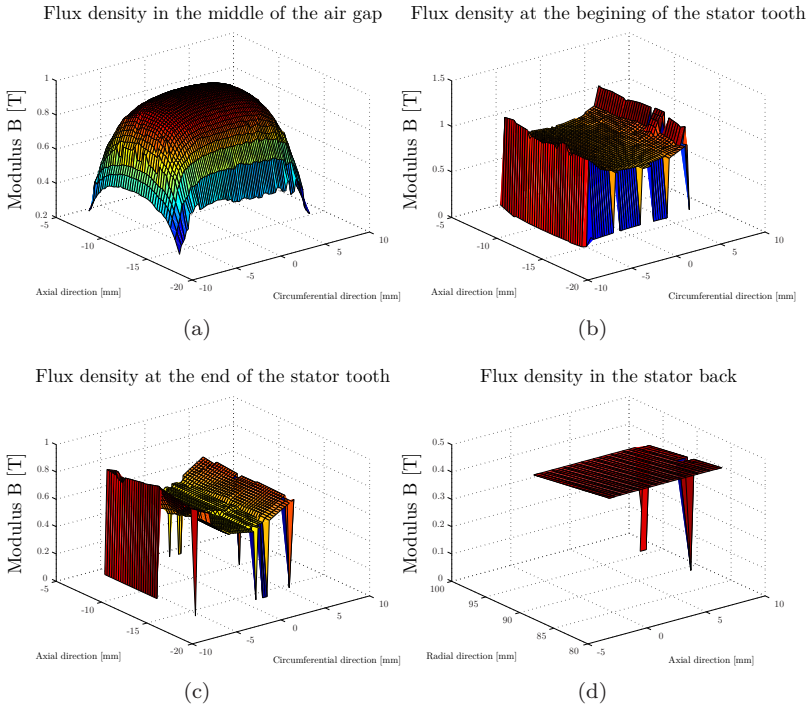

Figure 7.6: *Flux densities in different regions of the machine with magnets only in phase a: a) in the air gap, b) at the beginning of the stator tooth, c) at the end of stator tooth and d) in the stator back.*

simple analytical circuit. It can therefore be concluded that the reason for the high flux leakage lies in the inactive magnets that do not contribute to any useful flux, in fact, these magnets attract the flux from the main flux path and thereby cause a large loss in the useful flux.

7.4 Power factor

In order to calculate the power factor of the machine Eq. (6.94) is used. Two different simulations are performed, one with only magnets active and one with only the rated current in the windings. The results obtained from the simulations are shown in Table 7.1.

As can been seen from the Table 7.1 the simplified analytical model highly overestimates the power factor of the machine compared to the FEM simulated results. However, the results from the improved analytical model has a better agreement with the FEM simulated results. The

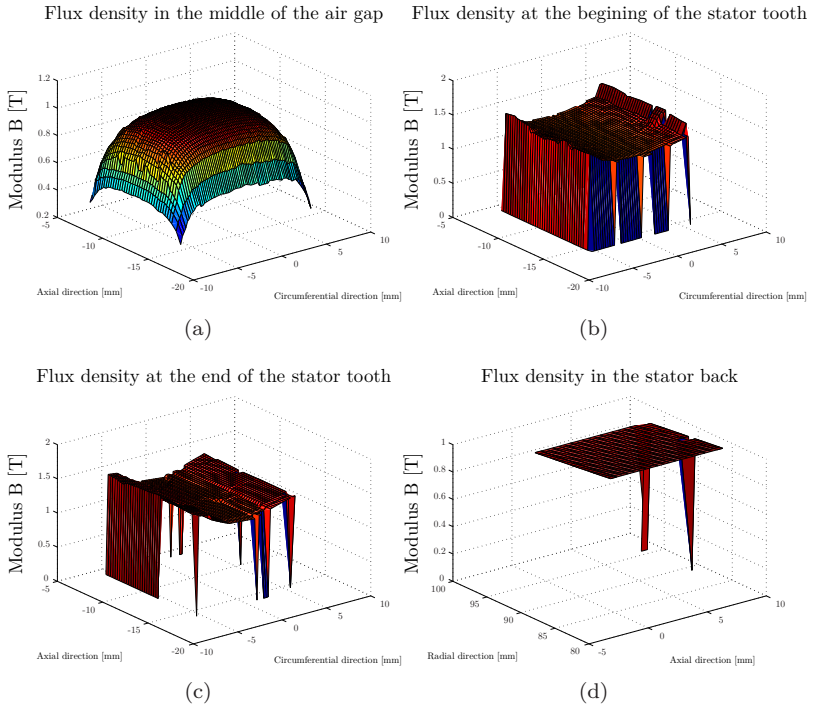

Figure 7.7: *Flux densities in different regions of the machine with only active magnets in phase a: a) in the air gap, b) at the beginning of the stator tooth, c) at the end of stator tooth and d) in the stator back.*

Table 7.1: *Power factor for the TFM obtained from the simulated values.*

	Simplified anal.	**Improved anal.**	**3D-FEM simul.**
pf	0.7131	0.3817	0.3279

small difference between them can be explained by the modeling of the leakage reluctance paths. By improving these models, the difference could be even smaller.

7.5 No load EMF

After the static simulations were carried out the 3D-FEM model was further developed and adapted for dynamic simulations. This model is used to determine the force produced, cogging force and the induced no load

voltage. Furthermore, the simulation under loaded conditions were also performed.

The Flux3D software allows for a circuit coupling to the meshed geometry. In this way the no load voltage is directly observed from the circuit in the post processing. The no load EMF is shown in Figure 7.8. As can be seen from the results, the no load voltage confirms the leakage

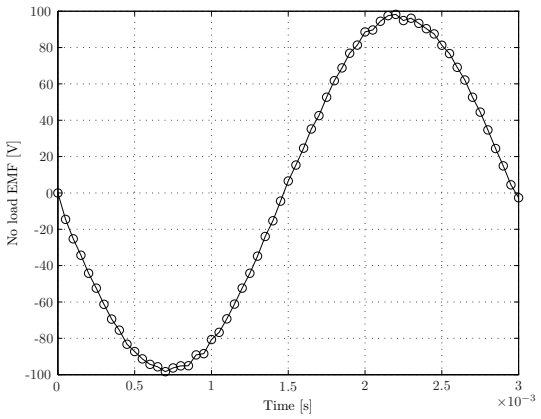

Figure 7.8: *Induced no load EMF.*

flux identified earlier. Desired value of the no load voltage is 200 V RMS. From the figure it can be seen that the RMS value is about 71 V which is approximately 1/3 of the value expected.

One interesting detail is the shape of the curve. Clearly the no load voltage is almost sinusoidal, which is in a way promising as this means that harmonic losses will be low.

7.6 Force

One of the final and most important figure of merit is the machines capability in force production. Thus, the simulations with a current introduced in the machine windings are performed. These simulations are carried out on the dynamic model, in a similar way to the no load voltage simulations. However, the circuit coupled to the 3D-FEM model is somewhat modified. A closer description of the different circuits is given in Appendix C. The simulation results are shown in Figure 7.9. As can be seen the maximum force produced is close to 1 kN. This value is lower compared with the maximum force from the simplified analytical model which is calculated to 2.54 kN. One of the main reasons for this is the large leakage flux.

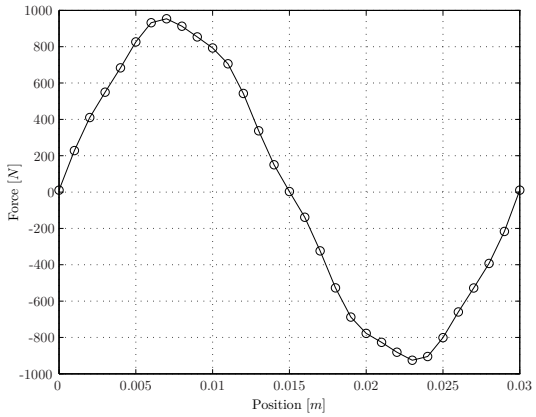

Figure 7.9: *3D FEM simulated values of the force.*

7.6.1 Cogging force

In order to validate the analytical results for the cogging force a 3D-FEM simulation was performed. The cogging force is a result of interaction between the magnets and the armature when unexcited i.e no current is present in the stator winding [52]. Thus the 3D-FEM model is of a multi-static nature rather than a dynamic. The simulated results for the total force in the machine are shown in Figure 7.10. As can be seen from the

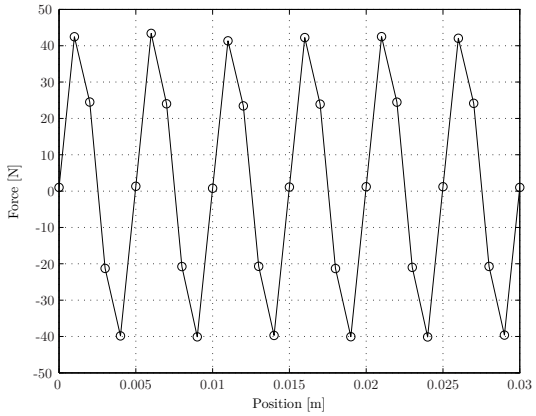

Figure 7.10: *3D-FEM simulated cogging force total.*

figure the peak to peak value of the cogging force is about 80 N.

The basic idea with the analytical results is to calculate the cogging force for one phase only. Due to the symmetry these results are then

shifted in the axial direction by 120, and 240 electrical degrees for phases 'b' and 'c' respectively. The total cogging force in the machine is then given by the sum of all three phases. In order to validate the analytical results a simulation with only one row of magnets is performed. The results are presented in Figure 7.11.

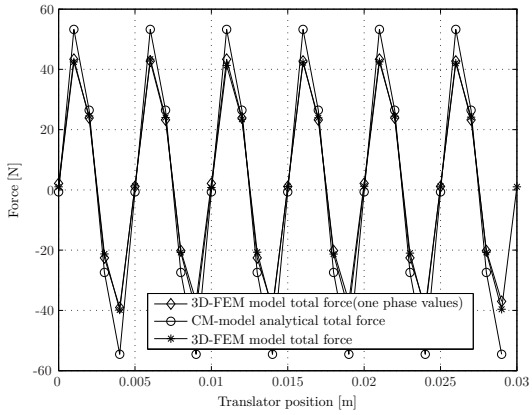

Figure 7.11: *Comparison of the simulated and analytical total cogging force.*

As can be seen from the figure the comparison between the results shows very good agreement. Although, the analytical results predict a somewhat higher cogging force the shapes of the curves are in very good agreement.

7.6.2 Comparison of One-layer versus Two-layer design

As described earlier in chapter 5 there are different possible designs of a global winding. It can either be wound in one layer or in two layers. Looking at the magnetic circuit, the two layer design seems to be a more natural choice. However, as can be seen from the results in Figure 7.12, there is negligible difference in the induced no load EMF. However, when it comes to force production the one-layer winding design will have a lower force. This is mainly due to the saturation of the magnetic circuit. In order to overcome this drawback, the one-layer machine has to be designed with irregular teeth shape. The width of the tooth in the middle of the winding should be increased to obtain a constant magnetic loading of the iron circuit. Furthermore, the area of the neighboring teeth has to be lowered in order to preserve the same copper area.

It can be concluded that the one layer winding design does not have any technical advantage compared with the two layer design. One possible advantage is cost reduction where only 6 windings have to be wounded instead of 12.

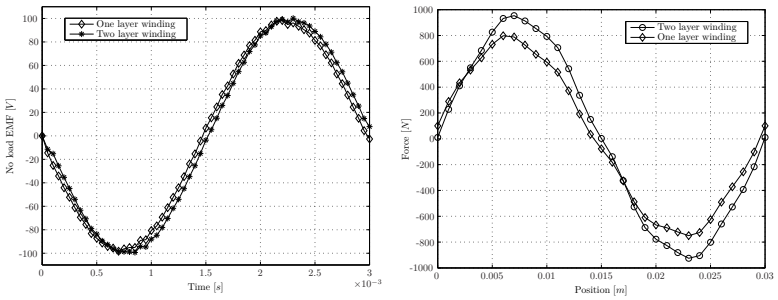

(a) (b)

Figure 7.12: *Comparison of the simulation results between one- and two layer winding: a) No load EMF induced and b) Force produced in the machine.*

7.7 Conclusions

In this chapter 3D-FEM simulations were presented. The results showed a large discrepancy between the FEM-simulated and simplified analytical results. In order to analyze the machine characteristics more closely, different simulation models were developed and analyzed. It was discovered that the machine suffers from a high leakage flux in the axial direction, which to a great extent is caused by the magnets in adjacent poles. These magnets do not contribute to any useful flux. As the magnets face only air, and no iron, they instead attract a part of the useful flux and disturb the main flux path. This was confirmed by the FEM-simulations when these magnets were turned off.

In order to improve the machine design, the most important task is to reduce the high leakage. Theoretically there are simple ways to do this, however, if manufacturing aspects are to be considered as well, this becomes a more complicated task.

Chapter 8

Manufacturing of the Prototype

This section will describe the prototype manufacturing process. It will discuss some problems related to manufacturing of the TFM. These problems mostly appeared during the manufacturing of the low leakage prototype [14]. It will also describe some problems encountered during the manufacturing process of the novel TFM that is investigated in this thesis.

8.1 Introduction

In principle TFM may be seen as a modular construction, where each pole pair is one module. At one instance of time, the axis of the poles on the mover must coincide with the axis of the stator teeth, in order to obtain the maximum flux. This presupposes that the lengths of the stator and the translator poles are the same. If there is a difference in the lengths the maximum flux may still be achievable, however, the shape of the flux linkage will not be the same as the predicted one.

8.1.1 Low leakage topology

Earlier prototype, built for the FPEC application, was a design of a low leakage topology. The aim with the design was to increase the utilization of the existing material. For the surface magnet design this was not possible, however, for the buried magnet design it was found, that the desired specifications could be fulfilled.

A 1.7 kW one-phase proof-of-concept prototype of the design of Figure 8.1 was dimensioned, analyzed and built [14]. Testing and the measurement of the prototype indicated that the flux linkage from the magnets was not in accordance with the FEM and analytical results. Further investigations of the machine showed two major manufacturing defects incurred during the construction of the prototype. The first was the partial demagnetization

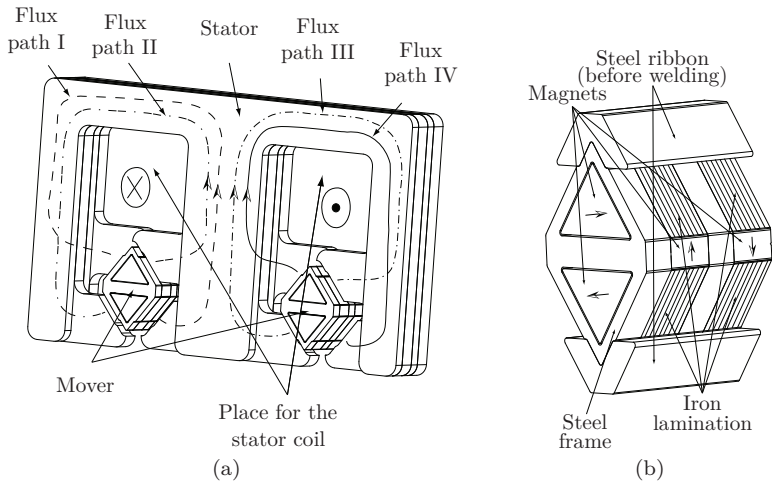

Figure 8.1: *3-D view of the Low Leakage linear TFM a) cross-sectional view of one phase b) detailed view of the mover [14].*

of the magnets due to the high temperature during the welding process of the translator. When the temperature reaches the curie temperature the magnetic properties of the magnets are completely destroyed. The second was the misalignment of the stator and the rotor poles. During the measurement it was not possible to identify the d and q axis in the machine. The stator laminations are pressed together and then weld on the upper side (outer surface). The translator, however, needed to be glued together before a stainless steel ribbon was placed on the each side of the triangle and then welded on the steel frame that keeps the magnets. The presence of different materials(laminations, rectangular-magnets, triangular-magnets, the rhombus steel-casings and the glue used to join these different portions) resulted in an elongated translator pole. Stacking of the poles by pressing did not result in the desired compression. The problems with misalignment of the poles is illustrated in Figure 8.2.

8.2 Magnet assembling

The assembling of the magnets on the mover may or may not be a difficult process depending on the mover design. Due to the high remanence flux, magnets tends to align themselves, which makes it very difficult to keep the magnets in place. Using magnet material before it is magnetized could solve this problem. However, it is very difficult to find a suitable solution for magnetizing the magnets already mounted on the rotor/translator, with the exception for some more simple designs.

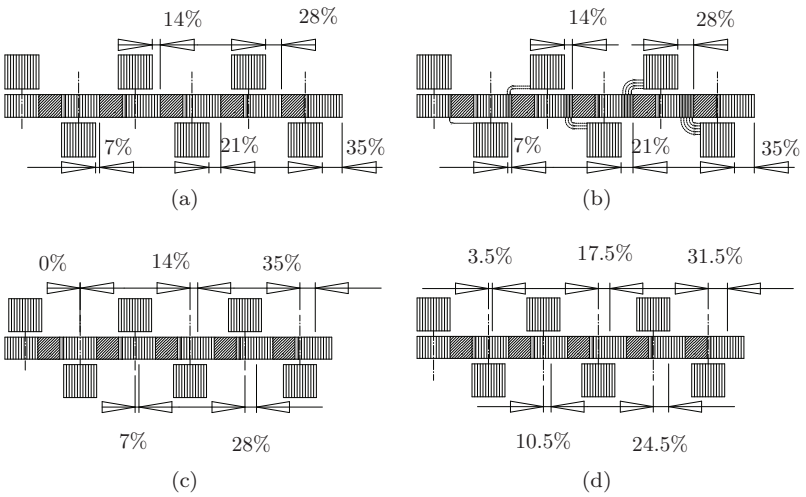

Figure 8.2: *Results of the incorrect mover tolerances: a) Enlargement of the mover pole, b) Loss in magnet-flux, c) Misalignment of axis, d) Shifting of (c) to facilitate calculations [14]*

Usually the magnets are stacked on the rotor/translator back iron from one side to the other. However, for the linear TFM, if there is a positioning error it will propagate over the entire mover length as was the case with the low leakage prototype [14]. For a conventional machine design this does not necessarily mean a significant loss in flux and in the worst case it can probably end up in a loss of a few percent. For the transverse flux machine this is of crucial importance. A misalignment at one pole in the direction of motion will result in a misalignment in the consecutive poles.

By gluing the magnets on a fixture first, the positioning error of the magnets is kept to a minimum. Another advantage is that several magnets can be glued at the same time, see Figure 8.4. For large scale production all magnets can be glued simultaneously.

8.2.1 Magnet coating

In order to avoid oxidation and prevent an erosion of the magnet, some magnets like NdFeB are protected by a thin layer of coating material. The thickness of the coating is usually in the order of some μm.

Different types of material are used in the coating process. From the perspective of gluing, some coating materials are to be preferred as different materials possess different so called 'surface tensions'. In order to achieve

a good attachment between the glue and the material, the surface tension of the material has to be higher than that of the glue.

Even more important is perhaps the stiffness of the coating itself. In the '*pull*' test, performed in the laboratory, it was evident that the coating of the magnets was the weakest part at the contact point. In other words, no mater how good the bound is, the coating of the magnet will still loosen first. This may be very critical in some demanding applications.

As mentioned, the coating protect the magnets from erosion which in the end will destroy the magnets and eventually also the machine. However it is not necessary to have the coating on the magnets in all applications. In some demanding applications where the humidity of the air is very high (e.g. $> 80\%$ relative humidity) other types of magnets , e.g. SmCo, that show negligible corrosion, can be used instead.

8.2.2 New assembling method

Experience from earlier prototype shows that the linear TFM are very sensitive for the misalignment of the stator and the mover axis. Misalignment leads not only to loss of the effective magnet area but also to increased leakage flux. This is true for the buried as well as the surface-mounted-magnets mover designs. In order to overcome this problem greater emphasis must be put in the assembly of the machine, already at the design stage. For

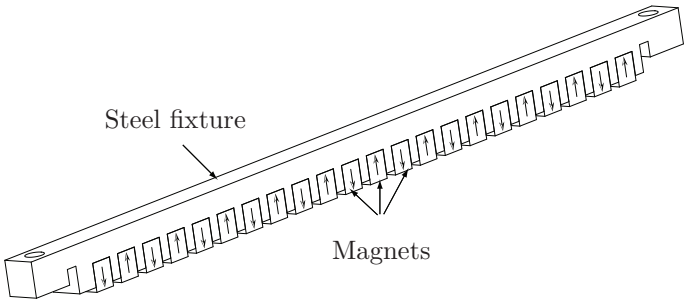

Figure 8.3: *3-D view of the fixture together with the magnets ready to be glue on the mover.*

the surface mounted magnet designs the two-glue-method has been chosen. The idea is to place the magnets on a fixture by gluing them with a special type of fast hardening glue as illustrated in Figure 8.3 and Figure 8.4(a). The strength of the glue should be high enough to overcome the magnetic pull force. Once the magnets are in place on the fixture another type of one component epoxy is applied on the top of the magnets that will glue the magnets on the mover. While the one component epoxy gets harder with increased heat, the fast harden glue looses its strength. The strength

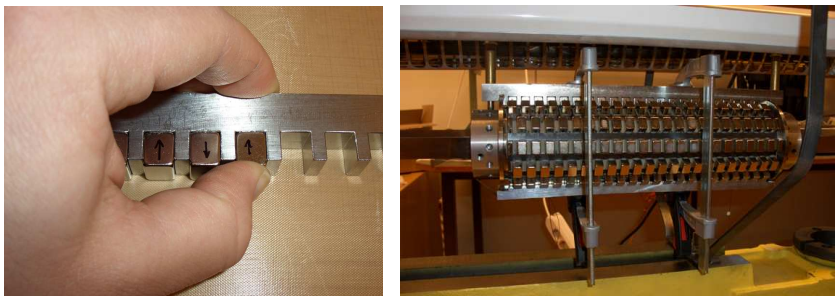

(a) (b)

Figure 8.4: *a) Magnets glued on fixture. b) Magnets on fixture glued on the translator.*

of the glue should be minimized to the extent that the fixture can be removed from the magnets without damaging them or damage the coating. Figure 8.5 shows the cure time and the stiffness of the glues. The different glues were chosen carefully in order to obtain good results. In this case the fast hardened glue was Loctite 4860 and the one component epoxy was the Bondmaster ESP109. In order to avoid any unexpected losses in the glue due to the armature reaction magnetic field, the glue with the non-metallic filled ceramic bonding was chosen. The maximum shear strength for one component epoxy is $30MPa$.

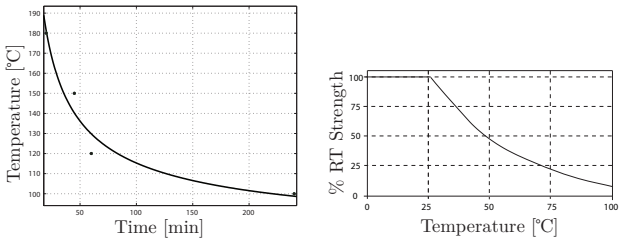

(a) (b)

Figure 8.5: *a) Cure time for the Bondmaster ESP 109. b) Stiffness as a function of time for the Loctite 4860.*

The glue itself does not provide enough support for the magnets in order to withstand the high forces during operation. With the aim to increase the stiffness of the translator, the void between the magnets was filled with a special mixture of epoxy. Before the epoxy was added to the translator a glass fiber bandage was wrapped around the magnets as an extra precaution. Then the translator was put into a cylinder and the

epoxy mixture was sucked in using a vacuum. Figure 8.6 shows the finished translator with the epoxy and the glass fiber bandage.

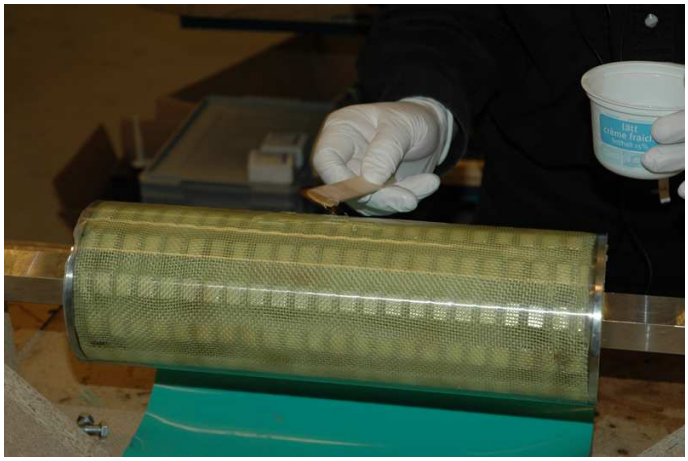

Figure 8.6: *Finished translator with the epoxy and the glass fiber bandage.*

8.2.3 Heat associated problems

Some problems associated with the heat were also encountered during the manufacturing process. In order to guide the fixture with the magnets to the right place some guide screws were employed. When the fixture is heated during the curing process it will expand slightly and due to the fixed guide pins it will also bend slightly, see Figure 8.7 below. The gap between the magnets and the stator back will increase closer to the middle of the translator. It was expected that the increased thickness of the fixture

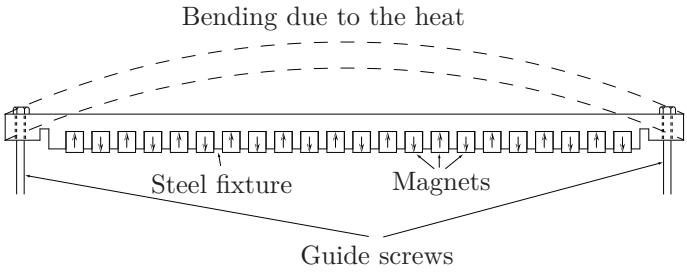

Figure 8.7: *Bending of the fixture from heat during the curing process.*

back would eliminate this problem. However, in order to harden the glue the temperature was increased to above 100 ℃. At this temperature the

problem with the bending was evident. In order to avoid this problem, clamps are applied at the several places along the fixture as can be seen in Figure 8.4(b).

8.2.4 Stator Construction

As mentioned the TFM is essentially a modular design where each pole can be seen as one module. The buried magnet design does not have any air pockets between the poles. This is a possible solution but the loss in force is about 30% as reported in [14]. The flux path in the machine is truly 3 dimensional. Not only the leakage flux but also the active flux is 3 dimensional. In novel the topology the active part of the flux is 2

Figure 8.8: *Laser cutting of the stator and translator iron laminations.*

dimensional and the designers intention is also to keep it that way. In order to have a reciprocating flux in the stator back the iron is therefore divided in stacks along the direction of movement of the translator. This is similar to the cooling ducts in large synchronous machines. However, while the cooling ducts are dimensioned for cooling and are preferably kept very small in order to have a more compact machine design, the space between the stacks is very much determined by the length of the pole. It can certainly be varied depending on how much pole area is covered by the magnets and the flux wave-shape that is required in the machine. However, in the simplest case where the entire pole length is covered by the magnets the space between the stacks will be the length of the pole. In the other

case where the length of the stack is prolonged the flux from the opposite magnet will lower the induced voltage, assuming negligible leakage flux.

In large synchronous machines the cooling ducts are usually made by welding a small iron part of the stator iron. These are only welded on the top surface on the stator back and not on the stator teeth. This is done in order to avoid folding of the iron sheet where welding is performed, which would result in a lower stacking factor and higher iron losses.

In the novel TFM the spacers are glued on the iron. Because the iron spacer is wide the welding process would certainly effect the iron lamination, and as mentioned above, would result in a lower stacking factor. The spacers are chosen wide to counteract the high forces in the axial direction. It will keep the iron teeth in position and minimize the risk for vibrations, which can generate a high noise level and in the worst case eventually a breakdown of the machine.

(a) (b)

Figure 8.9: *a)Only 4 spacer glued on the stack. b) Spacers glued on the stack iron sheet in the fixture.*

In order to preserve a high pressure on the stack a frame of steel was constructed around the stator, see Figure 8.10. Once all the stacks were in place they were exposed to very high pressure with a special fixture. Steel laths were put across the stator and welded at the ends of the steel frames which have a similar cross section to the stator iron, see Figure 8.9.

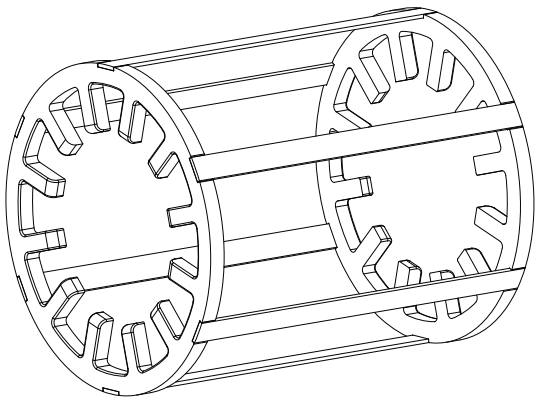

Figure 8.10: *Steel frame that is used to keep the stator together.*

8.2.5 Bearings

The translator in this machine is not allowed to rotate in any direction. In order to assure only axial movement and avoid any rotation of the translator the shaft of the translator was chose rectangular, see Figure 8.11. There are a lot of different types of linear bearings. However, not many of them offer the option that prevent the shaft from rotating.

The electromagnetic air gap is 1.25 mm. The physical air gap however, is very small, about 0.5 mm, because of the bandage and the epoxy layer. It is therefore very important that the bearings can preserve their tolerances under relatively high speeds.

The rectangular bearings are arranged so that the rectangular shaft rests on two sides in the bearing, thus avoiding wear of only one side in the bearing.

8.2.6 Shrink fitting of the stator

Once the stator was finished and the windings were in place it was fixed in an aluminum case as shown in Figure 8.12. In order to identify the exact position of the stator, screw holes were drilled afterwards. The stator was fixed into an aluminum case through a method that is well known in industry as the so called shrink-fitting method. The aluminum case

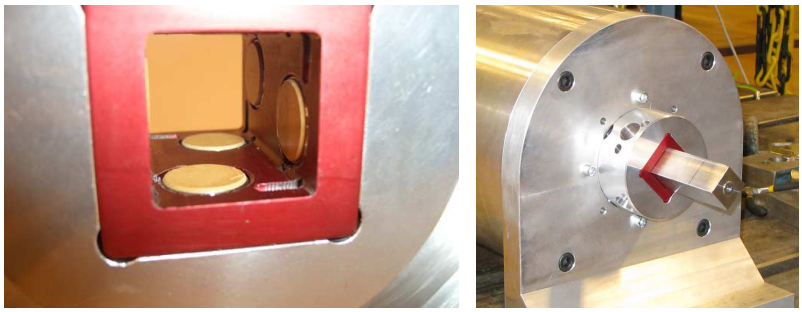

(a) (b)

Figure 8.11: *a) Rectangular sliding bearings in the prototype b) Rotation of the bearing by 90 degrees.*

is heated up to certain temperature and as the temperature of the case is increased the inner diameter of the case increases. The stator is then forced into position in the aluminum case. As the temperature of the case reduces the inner diameter will shrink back to its original dimensions, thereby applying a strong pressure on the stator and keeping it in position.

Figure 8.12: *Stator placed in an aluminum case.*

In order to preserve a certain pressure the inner diameter of the case

has to be somewhat lower compared with the outer diameter of the stator.

Screw holes are drilled after the stator was placed in the case and the exact position of the stator teeth could be determined. In this way once the translator is placed in the stator, magnetic poles on the translator can be placed in the middle of the stator teeth, thus avoiding any loss of flux due to the misalignment of the stator and magnet pole axis.

Chapter 9

Measurements

This chapter discusses the measured results from the prototype machine, which are later compared both with the analytical and the 3D-FEM simulation results. Furthermore, the differences in the obtained results are explained and some conclusions are drawn.

9.1 Force production

Comparison of force production is one of the best indicators that the machine works as expected. Simulated and the measured results are shown in Figure 9.1. The figure shows the force as a function of the translator position. The DC current has been applied to the machine which was Y-connected. The applied current flows through phase 'a' and through phase 'b' and 'c' where the later two are connected in parallel. This represents an instance of sinusoidally supplied current to the windings. Then, the position has been varied slowly and the force has been measured at each position.

The force has been measured with the force meter Burster Compression Load Cell 2 KN with a precision of 0.5% over its range.

As can be seen from the figure the measurements have been performed with different amplitudes of the currents with the maximum current of 40A. These values are compared with the 3D-FEM simulations. The result in Figure 9.1(a) shows that there is a discrepancy between the simulated and measured results. The cogging force is more pronounced at lower value of the electromagnetic force and the armature current . However, as the current amplitude increases it can be noticed that the agreement between the results improves drastically. Figure 9.2 shows simulated results of the force at the armature current of 65 A. At the moment measurements were performed it was not possible to reach a higher current value than 45A due to technical difficulties. However, based on the previous result illustrated

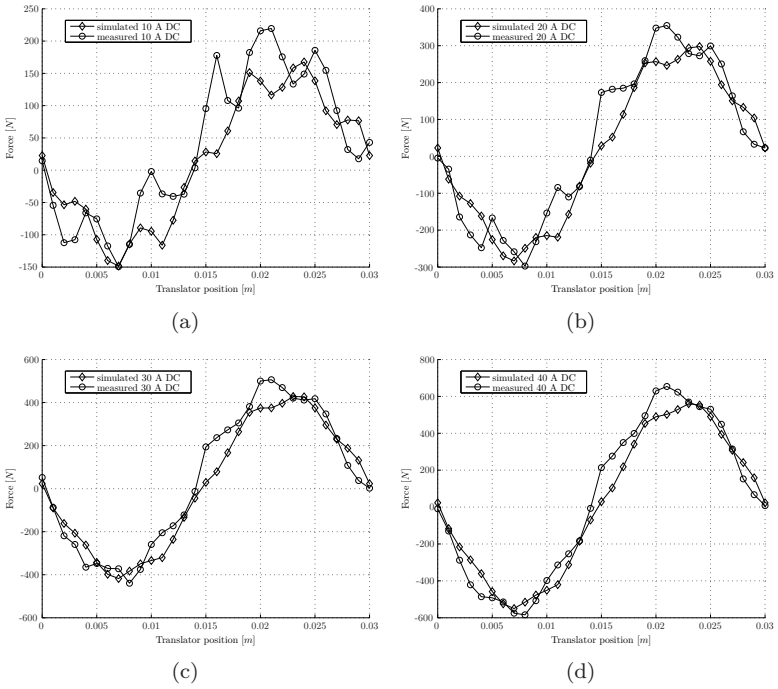

Figure 9.1: *Measured and 3D-FEM simulated force as a function of the translator position a) I= 10 A, b) I= 20 A, c) I= 30 A and d) I= 40 A .*

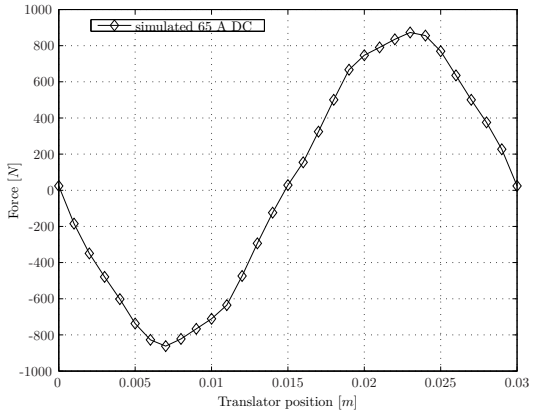

Figure 9.2: *3D-FEM simulated force as a function of the translator position*

above, it can be concluded that the force with 65A should agree quite well with the simulations.

9.1.1 Cogging force

Cogging force is usually a non-desired effect in electrical machines. It gives rise to pulsations in the main force produced by the machine, which also results in higher vibrations and noise. Furthermore, it also generate some extra losses.

Figure 9.3 shows the total force measured in the machine together with the 3D-FEM simulated results. As can be seen form Figure 9.3(a) the results obtained from the measurement gave only a positive net force. However, if the offset in the measured results is removed the agreement between the results is very good as shown in Figure 9.3(b). Furthermore, it can be observed that the amplitude of the measured force is slightly higher compared to the simulated. There are two possible explanations to this.

The first is due to the difference between the simulated model and the prototype machine. The spacers between two stator stacks are not included in the simulation model and the space between two stacks is treated as air. In the prototype the spacers are made of nonmagnetic steel, which in theory should behave as air as the relative permeability of this type of steel is close to one. However, during the processing, the material was exposed to heat because of the friction heat that was generated during the cutting process. This heat can influence the magnetic properties of the material, in a similar manner the heat influences magnetic properties of the permanent magnet materials. This phenomenon was discovered shortly after the assembling of the machine had started. However, no further investigation on the magnetic

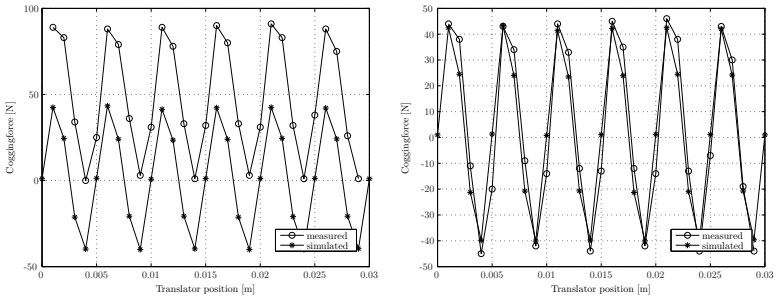

(a) (b)

Figure 9.3: *Measured and 3D-FEM simulated cogging force as a function of the translator position a) original measured force b) measured force without offset.*

properties of the material was made. It is therefore difficult to quantify this

effect. The magnetic properties could be different in different parts. It is, however, reasonable to assume that the magnetic properties in different parts are roughly the same.

The second reason is the level of friction in the sliding bearings in the prototype. This could be verified by removing the stator housing and leaving only the mover and the bearings. By pulling or pushing the mover the friction force in the bearings can be measured. Although this has not been done it can be concluded that the amplitude of the measured force would be lower when the friction force is excluded (subtracted). Therefore, the agreement between the calculated and measured results would be even better.

Figure 9.4 shows a comparison between the results obtained from all different methods used to analyze the cogging force i.e. FEM-simulated, measured and analytical methods.

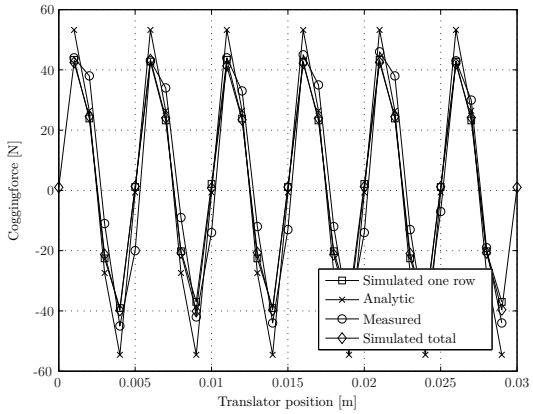

Figure 9.4: *Comparison of analytical, FEM-simulated and measured results of total cogging force in the machine.*

As can be seen from Figure 9.4 the shape of the different curves agree very well. It can also be noticed that the agreement between measured and analytical results is fairly good. However, this agreement should be taken with a certain precaution. The analytical method can be used for a preliminary optimization but should be supplemented by a 3D-FEM analysis when greater accuracy is required.

9.2 Flux

Another good indicator of the characteristic of an electrical machine is the flux linkage. Figure 9.5 shows the fluxes in different phases obtained from the measurements and from the 3D-FEM simulations. The measurement of

the flux is performed by a flux meter, which basically is a voltage indicator. By slowly moving the translator a voltage is induced in the phase winding. This voltage is integrated and the flux is obtained for different translator positions as shown in the figure.

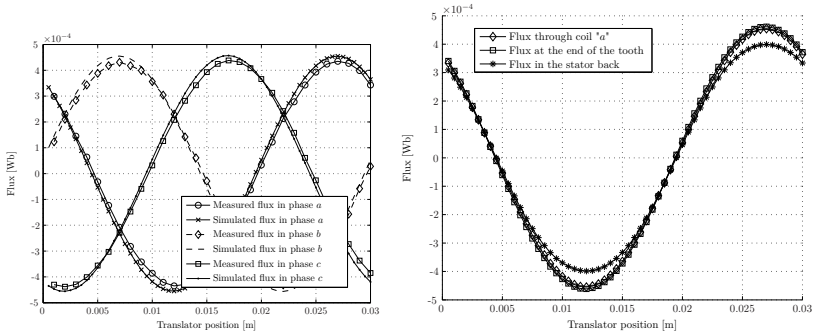

(a) (b)

Figure 9.5: *Fluxes obtained from the measurement and from the 3D-FEM simulations a) simulated and measured fluxes for all three phases b) simulated values in phase 'a'.*

The simulated values are obtained from the software by calculating the flux seen by the winding. However, there are also other ways to calculate the flux. One is by looking at the flux density in the stator back. This method has been used in [53], according to which the total flux seen by the winding is not only the flux in the stator back but also some minor flux paths. These minor flux paths are the interaction of the fluxes with the neighboring phases. The magnetic circuit from phase 'a' interacts with the magnetic circuit of the phase 'b' and phase 'c' that lie next to each other. In order to obtain the total flux it is therefore more accurate to calculate the flux at the end of the stator tooth. The area of the calculation of flux is shown in Figure 9.6. The result from the calculations of flux in different areas are shown in Figure 9.5(b). As can be seen the flux calculated in the stator back is somewhat lower compared with the flux calculated at the end of the stator tooth. At the same time it can be noted that the flux calculated at the end of the stator tooth agrees much better with the total flux seen by the coil, which is the option given by the software Flux 3D.

In [53] the measured value of the winding flux linkage was higher compared to the simulated value, which was calculated at the stator back. There are at least two reasons causing this disagreement. The first is, as already explained, that the integration of the flux density at the end of the stator tooth should be used in the calculations and the second is the remanent flux density of the magnets. In order to compensate for the op-

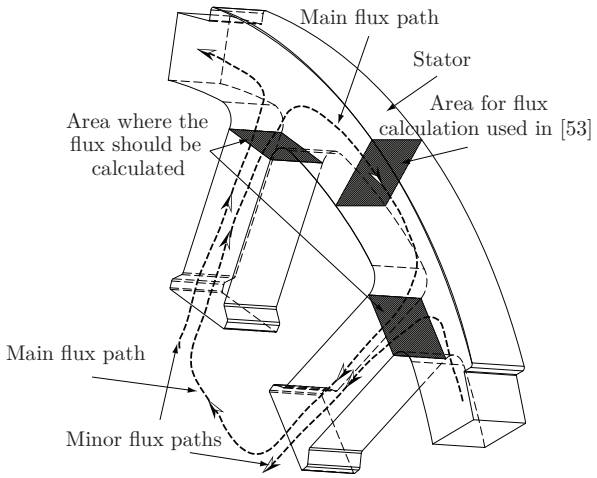

Figure 9.6: *3-D view of the portion of the stator where the flux is calculated and where it should have been calculated.*

eration temperature in the FPEC application, the remanent flux density in the magnets was lowered to 1.1T in the simulations. However, the measurements performed on the prototype in the laboratory, were conducted at an ambient temperature of 25 ℃. At this temperature the remanent flux density of the magnets is around 1.25 T, which has also been corrected in the simulations in the latest results. As can be seen from the results in Figure 9.5 the agreement between the measured and simulated flux is very good.

9.2.1 No load EMF

The variation of the no load induced voltage with the translator position is shown in Figure 9.7. The agreement between the simulated and measured voltage is very good. This comes as no big surprise as the induced voltage is directly proportional to the rate of change of the flux linkage. The measured value is derived from the measured flux. The simulated value is obtained directly from the simulation software. Flux 3D allows the user to connect the circuit to the geometry and the voltage is then easily obtained across an infinite resistance at the terminal connections in the circuit. The figure also shows the derived, no load EMF, from the simulated flux calculated at the end of the stator tooth.

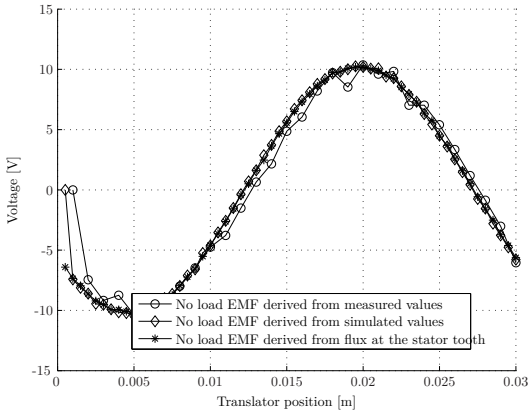

Figure 9.7: *No load EMF induced at speed of 1* $\frac{m}{s}$.

9.3 Machine parameters

The correct values of the machine parameters are very important. The value of the resistance gives direct information on the copper losses and the resistive voltage drop in the machine. Usually the calculation of the resistance is a straight forward process which is also true for the measurements. The resistance varies with temperature, this however does not impose any difficulties and can easily be predicted with very high accuracy.

For the control of the machine, the values of the inductances in the machine are of great importance. An accurate value of the d-axis inductance is important, at the same time this value indicates the field weakening capability of the machine.

9.3.1 Inductance measurement

There are different ways to measure inductance in the machine. One of the simplest methods is looking at the time constant. First the current in the machine is built up to a certain level and then the terminals of the machine are short circuited. By simply measuring the current in the circuit and knowing the value of the resistance, the inductance can be found by solving the equation below

$$0 = L \cdot \frac{\mathrm{d}i}{\mathrm{d}t} + R \cdot i \tag{9.1}$$

Although this method is very simple it is not recommended for accurate measurements [54].

There are several other methods to measure the inductance. Most of them are performed with the rotor at stand still. Due to the fact that

the mover is standing still the magnets will see an alternating flux from the stator. This is especially true for the d-axis position of the mover. Depending on the magnetic circuit design of the machine, there might me some problems with the magnetic field displacement caused by the eddy currents induced in the magnets. The field generated by eddy currents will have a counteracting effect on the field from the stator, thus the resultant field in the magnets will become inhomogeneous. According to Hallén [55] the field constriction in a material can be calculated according to

$$\hat{B}(x) = \hat{B}_0 \cdot \sqrt{\frac{\cosh(2 \cdot \chi \cdot x) + \cos(2 \cdot \chi \cdot x)}{\cosh(\chi \cdot x) + \cos(\chi \cdot x)}} \cdot e^{j\varphi} \tag{9.2}$$

where $\hat{B}_0$ is the flux density at the surface, just inside the magnet and it is the magnitude of the flux density without any interference from the eddy currents in the magnet. Factor $x = \pm\frac{\ell_m}{2}$ represents the end points in the magnet in the axial direction and factors χ and φ are given by Eq. (9.3). Here it should be mentioned that factor χ is the damping constant.

$$\begin{cases} \varphi = \arctan(\tanh(\chi x)\tan(\chi x)) - \arctan\left(\tanh\left(\chi\frac{\ell_m}{2}\right)\tan\left(\chi\frac{\ell_m}{2}\right)\right) \\ \text{where} \qquad \chi = \sqrt{\frac{1}{2} \cdot \mu_m \cdot \mu_0 \cdot \omega \cdot \sigma} \end{cases} \tag{9.3}$$

From the equation above it can be noted that the magnetic field displacement is increasing with the conductivity and the permeability of the magnet, and also with the frequency of the imposed field.

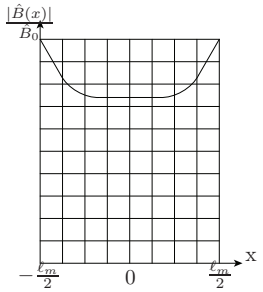

Figure 9.8: *Field displacement inside the magnet.*

Figure 9.8 illustrates the flux density distribution in the magnet. The flux density is lowest in the middle of the magnet. For the case of the prototype the width of the magnet in the axial direction $\ell_m = 10$ mm $\sigma_{magnet} = 625000$ and $\mu_m = 1.05$ which gives a maximum reduction of the flux in the range of 1%. This indicates that the flux density in the magnet will not be significantly affected. Hence the value of the inductance from

the standstill method can be considered accurate enough also for loaded conditions. Three different methods are described in the following section.

Calculation of L_d and L_q from self and mutual inductances

The first method is based on the calculation of L_d and L_q inductances from the self and mutual inductances. Therefore, this method requires that the neutral in the machine is accessible. According to [56], in a sinusoidally distributed winding, the self and mutual inductances of each phase can be expressed as a function of rotor position

$$L = L_0 \pm L_1 \cdot \cos\left(2 \cdot \theta_m\right) + L_{lk} \tag{9.4}$$

$$M = M_0 \pm M_1 \cdot \cos\left(2 \cdot \theta_m \pm \frac{2 \cdot \pi}{3}\right) \tag{9.5}$$

where L_{lk} is the leakage inductance and L and M represents the self and mutual inductances respectively. θ_m is the mover position given in mechanical degrees. For the linear machine however the θ_m has to be translated into a linear position of the mover. This is given by

$$\theta_m = \frac{\pi}{\ell_{stroke}} \cdot z \tag{9.6}$$

where ℓ_{stroke} is the length of the stroke in the machine and the z is the position of the mover relative the end position of the mover.

For the practical machine, where the effect of space harmonics may not be negligible, L_d and L_q inductance can be calculated by the Eq. (9.7) and Eq. (9.8) respectively [56].

$$L_d = (L_0 - M_0) - \left(\frac{L_1}{2} + M_1\right) + L_{lk} \tag{9.7}$$

$$L_q = (L_0 - M_0) + \left(\frac{L_1}{2} + M_1\right) + L_{lk} \tag{9.8}$$

If, on the other hand, the effect of the space harmonics is sufficiently low, the equations above can be somewhat simplified. The connection diagram for the measurement setup is shown in Figure 9.9.

One phase is supplied by a voltage source where the line current is measured, at the same time the voltage in one of the other two phases is measured. The measurements are performed for different position of the mover. The self and mutual inductances for the different positions of the mover are given by following equations

$$L_a = \frac{\sqrt{\left(\frac{V_a}{I_a}\right)^2 - R^2}}{2 \cdot \pi \cdot f} \tag{9.9}$$

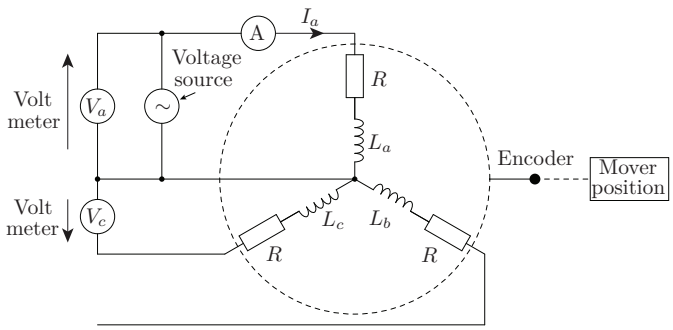

Figure 9.9: *Inductance measurement setup for the standstill method with access to the neutral point.*

$$M_{ac} = \frac{V_c}{2 \cdot \pi \cdot f \cdot I_a} \tag{9.10}$$

where R is the stator resistance, f is the supply frequency,V_a is the supply voltage, V_c is the measured voltage induced in the one of the other two phases and I_a is the measured line current.

The length of the stroke in the measurement is set equal to the length of one pole. This does not significantly affect the results of the measurements. Calculated values of L_a and M_{ac} are shown in Figure 9.10. A curve fitting is applied to the measured values which is also shown in the figure. From these curves, the values of the self and mutual inductance are calculated according to Eq. (9.4) and Eq. (9.5). The parameter L_0, M_0, L_1 and M_1 which are determined accordingly are then used to calculate the values of L_d and L_q according to equations Eq. (9.7) and Eq. (9.8).

The result of the L_d and L_q inductances obtained according to the method described above are shown in Figure 9.11.

As can be noted from the figure, the inductances have been measured at approximately only half the rated current which is 46 A. This is because the neutral point is not dimensioned for the rated current. The neutral was mounted after the machine was wound. These measurements will therefore not give the complete picture of the inductances in the machine, as the most interesting values of inductances are at rated current where saturation effects start to become evident. However, the measured values still give a hint about the value of the inductances and its slope.

Calculation of L_d and L_q from the flux linkages

In order to overcome the problem with the neutral point another method has been proposed in [57]. This method is a variant of the previous method.

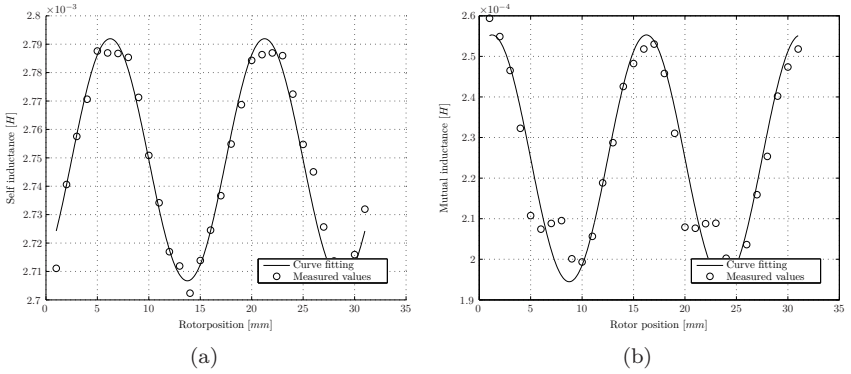

(a) (b)

Figure 9.10: *Variation of self and mutual inductance with mover position, measured and curve fitted values a) self inductance and b) mutual inductance.*

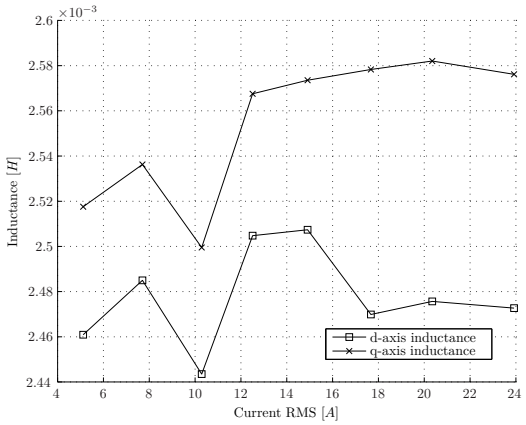

Figure 9.11: *L_d and L_q inductance as a function of line current RMS value*

As in the previous method, the measurements are obtained with the mover at standstill. However, instead of performing the measurements with the mover placed in different positions the method is further simplified by keeping the mover either in the *d*- or in the *q*-position. Since the availability of neutral is no longer necessary, two phases are connected in parallel and thereafter connected in series with the third phase. The connection diagram of the circuit is shown in Figure 9.12.

As shown in the circuit above, the machine is supplied by a voltage source and the measurement of line current and voltage are performed. In the laboratory setup, the voltage source supply delivers almost a per-

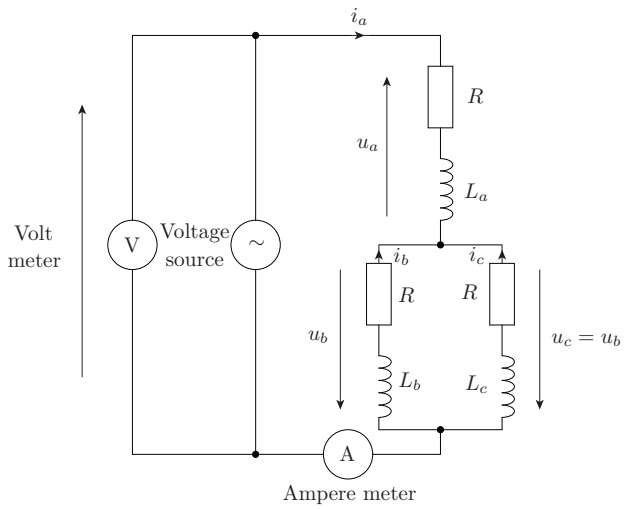

Figure 9.12: *Inductance measurement set up for the AC standstill method without the neutral.*

fect sinusoidal voltage. The mover is locked in either the d- or in the q-axis position. The d-axis position is found by applying a DC-current to the machine windings, with the mover unblocked. The windings were connected according to the circuit in Figure 9.12 with the difference that the AC-supply voltage has been replaced by DC-source voltage that has been tuned to give the rated current in the circuit. Once the mover has been aligned to the d-axis it is locked in this position and measurements were then performed with the AC-supply voltage. The L_d inductance is then calculated from the measurements. In a similar way measurements and calculations are performed for the L_q inductance. The position of the mover in the q-axis is half a pole length from the d-axis of the machine.

The phase voltages u_a, u_b and u_c are transformed into d- and q-axis components u_d and u_q by using Parks transformation. The d- and q-axis voltages can be expressed by Eq. (9.11).

$$\begin{cases} u_d = \frac{2}{3} \cdot (u_a - u_b) \cdot \cos(\theta) = \frac{2}{3} \cdot u \cdot \cos(\theta) \\ u_q = -\frac{2}{3} \cdot (u_a - u_b) \cdot \sin(\theta) = -\frac{2}{3} \cdot u \cdot \sin(\theta) \end{cases} \tag{9.11}$$

where the θ is the translator position in electrical radians.

From Eq. (9.11) it can be noted that the u_d- and u_q-voltages are directly proportional to the measured voltage. Since the mover is blocked during the measurement, the angel θ is constant which can be either 0, $\frac{\pi}{2}$, $\frac{3\pi}{2}$ or

2π. In the similar way the i_d and i_q currents can be calculated from the measured current in the laboratory setup.

The relation between the flux linkage, voltage and the current is given by Eq. (9.12) [58].

$$u(t) = R \cdot i(t) + \frac{d\Psi(t)}{dt} \tag{9.12}$$

where $u(t)$, $i(t)$ and $\Psi(t)$ are instantaneous values of voltage, current and flux linkage respectively. From Eq. (9.12) above the instantaneous flux linkages are given from the following expression

$$\Psi(t) - \Psi(0) = \int_0^t (u(t) - R \cdot i(t))\, dt \tag{9.13}$$

the value of the $\Psi(0)$ is the flux linkage at time $t = 0$. Thus, from the equation above, the value of the flux linkages is easily calculated at any instant of time. Here, an implicit assumption is made that the value of the resistance is well known. Furthermore, from the flux linkage above the inductance is given by

$$L = \frac{\Psi(t) - \Psi(0)}{i(t)} \tag{9.14}$$

The values of the flux linkages in the d- and the q-axis can now be calculated. These values are given by

$$\begin{cases} \Psi_d(t) - \Psi_m - \Psi_d(0) = \int_0^t (u_d(t) - R \cdot i_d(t))\, dt \\ \Psi_q(t) - \Psi_q(0) = \int_0^t (u_q(t) - R \cdot i_q(t))\, dt \end{cases} \tag{9.15}$$

Ψ_m is the magnet flux linkage and is not time dependant since the mover is locked. When the mover is placed in the d-axis position the q-axis current is zero and the value of L_d can be calculated from Eq. (9.14). Similarly, when the mover is in q-axis position the value of the i_d current is zero and the value of L_q can be calculated.

Two methods have been used to determine the inductance: 3D-FEM simulations and the measurements. Simulation software allows for the coupling of the electrical circuit to the meshed geometry. Thus, this method is well suited to calculate the inductances. In both cases voltage and current wave-forms have been integrated. For the simulation results, however, an alternative method is to calculate the flux linkages directly in the software. The circuit used in the simulations is similar to the circuit shown in Figure 9.12. The mover is placed in the desired position and the speed is set to 0.

The corresponding measurements are performed on the prototype machine. As mentioned, the machine is supplied by an almost perfect sinusoidal voltage. The current and the voltage are measured at the two

different mover positions: the d- and the q-axis positions. The current in the machine is set to a 45 A RMS which is close to the rated current of the machine (46 A RMS).

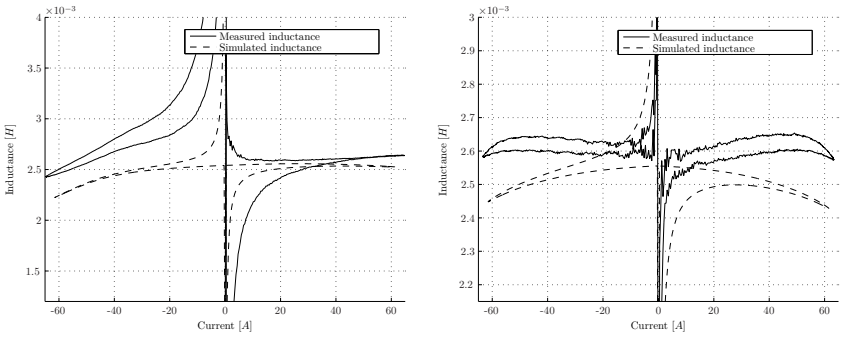

Figure 9.13: *Measured and simulated inductances as a function of the current 9.13(a) d-axis and 9.13(b) q-axis .*

Figure 9.13(a) shows the measurement- and the simulation results for the d-axis direction. As can be noted the simulation results are slightly lower than the measurement results. One of the reasons is the simulation model of the machine.

With the aim of reducing the simulation time it is often necessary to find symmetries or periodicity in the machine and thereby reduced the size of the simulation model. In the 3D-FEM model of the novel TFM topology only 2 pole lengths, which corresponds to 1/8 of the total machine length, have been simulated.

The 3D flux software is a powerful simulation tool which allows, although only one part of the machine is simulated, for the calculation of the total flux linkage. By using the non-meshed coils the software can take into account of symmetries in the machine and calculate the total flux linkage. However, in the simulation model used for the novel TFM the periodic boundary conditions makes it difficult to obtain the total amount of flux directly in the software environment. Instead, in order to obtain the total flux and thereby the total inductance, the results of the simulated part has to be multiplied by the total number parts that make up the complete machine. One drawback of this is that the end effects in the machine are not really represented in the simulation model.

Another reason for the deviation of the result is, as explained in an earlier chapter, the presence of nonmagnetic steel spacers which are not taken into account in the simulation model.

From Figure 9.13(b), it can be noted from the measured results, that the value of the inductance increases with increasing current before it starts to decrease again. Usually the values of the inductance are decreasing with increasing current. This is due to the effect of saturation of the soft iron material that is usually present in electrical machines. This can be clearly seen from the simulation results in the figure. It is difficult to explain the reason behind the phenomenon of increasing inductance with increasing current, which is obtained in the measured results. One possible explanation might be the presence of the steel spacer. As mentioned, in the simulated results the iron spacers are absent.

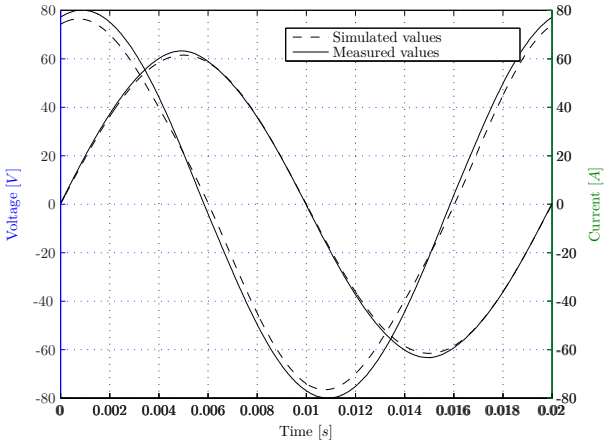

Figure 9.14: *Simulated and measured values of voltage and current when the mover is placed in the q-axis direction (the curves with higher amplitude represent the voltage)*

Figure 9.14 shows the current and the voltage waveforms, both measured and simulated, with the mover in the q-axis direction.

Calculation of L_d and L_q from the reactive power

For this method the measurement set up is the same as in the previous measurements. The translator is placed in the d and the q direction respectively, where the L_d and L_q inductances are calculated according to

$$L_d = \frac{2}{3} \cdot \frac{Q_{daxisposition}}{2 \cdot \pi \cdot f \cdot I^2_{daxisposition}} \tag{9.16}$$

$$L_q = \frac{2}{3} \cdot \frac{Q_{qaxisposition}}{2 \cdot \pi \cdot f \cdot I^2_{qaxisposition}} \tag{9.17}$$

The measurements are performed for different RMS current values in the circuit. The results are presented in Figure 9.15.

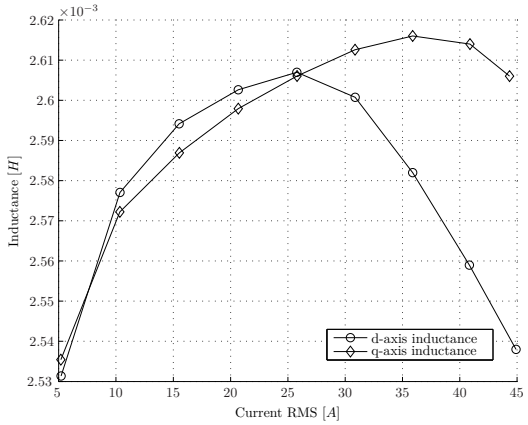

Figure 9.15: *Inductance as a function of the current obtained through reactive power measurements.*

As can be seen from the figure the effect of the iron spacers is evident even in this method.

Comparison of different methods

All methods have their strengths and weaknesses. The first method described requires access to the neutral point which is not always available. If, however, there is an access to the neutral point the method is quite convenient as there is no need for measuring the phase angle but only the RMS values of the current and the voltage. A disadvantage is that there has to be an encoder or some other device for the measurement of the position of the mover/rotor.

The second method described does not require any encoder as the measurements are performed only for two mover positions i.e. d- and q-axis. Thus the measurement is slightly more simplified. However, as the curves have to be integrated in order to calculate the inductances the measurement equipment has to be accurate.

The last method is based on measurement of the voltage current and the phase angle between them. Thus a power meter or any other equipment that can measure the phase angle between the voltage the current is required. This method does not require access to a neutral point. It can be seen as a combination of the previous two methods as the RMS current has to be varied as in method one but only in the d- and the q-axis directions as in method two.

It is not easy to say which method is to be preferred before the other. All methods gave similar results. However, looking at the FEM simulations it can be concluded that the method 2 is to be preferred as only two simulations have to be performed whereas a few more simulations have to be performed for the other two methods.

9.3.2 Resistance

The measurement of resistance is straight forward. A DC current source is connected to the winding and the voltage across the winding is measured. The resistance is calculated by dividing the voltage with the current. The measurements are performed on all three phases and the final value is the average value of these.

As the resistance is temperature dependant it should be mentioned that the measurements are performed at an ambient temperature of about 20 ℃.

The obtained value from the measurements was 0.228 Ω while the calculated value was 0.2292 Ω, which agrees very well.

9.4 Loaded condition

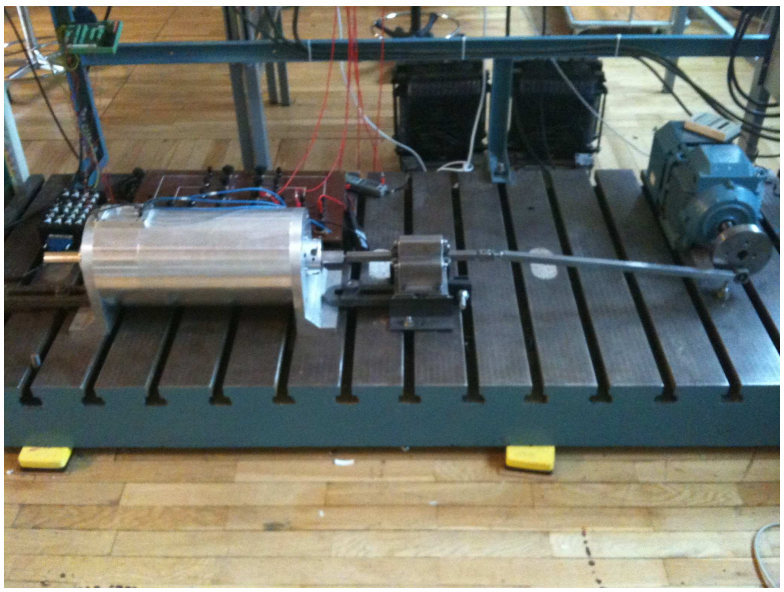

Figure 9.16: *Measurement setup for load conditions.*

The machine is connected to a conventional engine and is driven through a rotating motion as shown in Figure 9.16. The resultant motion of the prototype will not be a linear motion as is sometimes desired. The current and the voltage have the waveforms according to Figure 9.17.

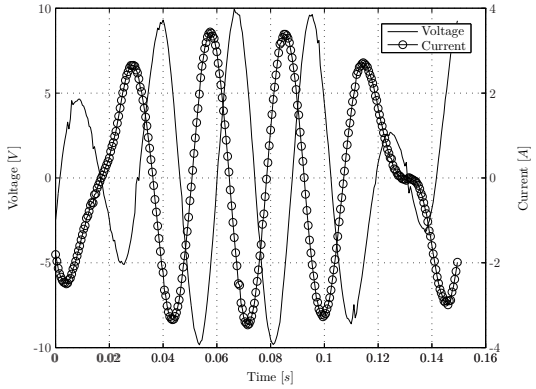

Figure 9.17: *Voltage and current at the speed of ca 1* $\frac{\mathrm{m}}{\mathrm{s}}$ *and the load of* $R_{load} =$ 2.684 Ω.

The simulation results based on nonlinear motion are compared with the measurement, shown in Figure 9.18.

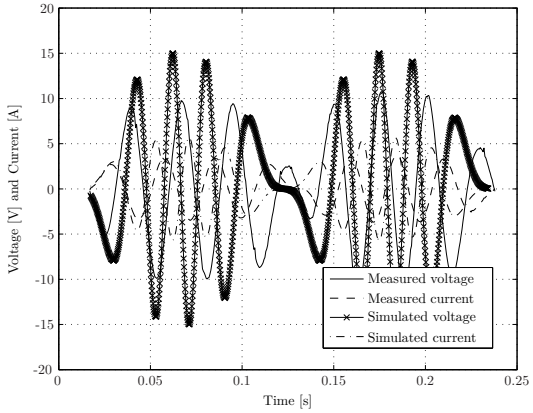

Figure 9.18: *Simulated and measured values at the speed of 270 rpm and a stroke length of 120 mm with* $R_{load} = 2.684\ \Omega$.

As can be seen the agreement of the results is not very good. This is mainly due to the difference in the motion profile of the translator. In

the simulation environment the motion of the translator is assumed to be sinusoidal. The profile in the measurements seems to be different.

The speed versus time profile has not been recorded during the measurements as in theory this profile should be sinusoidal as it is achieved by a rotating motion. However, due to friction and other forces in the linear machine it seems that the rotating machine does not have enough capacity to keep a constant rotational speed.

9.5 Conclusions

Several measurements have been performed and the results have been compared with both the analytical and the simulated values. The simulated force values showed good agreement with the measurements. At lower values of the current the effect of the cogging force was evident, however, as the value of the current was increased the agreement between the obtained results is much better.

The agreement between the simulated and the measured values of the flux linkage was also very good. In Chapter 6 simulated values were compared with the analytical results, both for the simplified- and improved analytical model. From these comparisons it was shown that the simplified analytical model overestimated the flux linkage by almost twice times the observed peak value. The improved analytical model, however, showed a much better agreement where the difference between the peak values is about 20%. This indicates a strength of the improved analytical model. Further, it can be concluded that there exist a certain interaction between the adjacent magnetic circuits which belong to the different phases. Therefore, in order to obtain the correct magnetic flux linkage, the flux density at the end of the stator tooth should be used instead of the flux density in the stator back.

Three different methods were described and used for the measurements of the inductances. All three methods showed similar results both for the d-axis and for the q-axis inductances. In the analytical calculations it was assumed that the value of the inductance was equal in both d and q directions, where the value of inductance was calculated to $L = 2.0154$ mH. This is lower compared to the measured and simulated results that varied between $2.4 - 2.6$ mH. However the agreement is still acceptable. The resistance value on the other hand was in much better agreement.

The comparison of the simulated- and measured results for the loaded conditions, did not show very good agreement. This is mostly due to the speed profile, which in the simulations was assumed to be purely sinusoidal but in reality was something else. As the correct speed profile was not recorded and used during the simulations it was difficult to make a justi-

ficable comparison. Nevertheless, the comparison is acceptable under the prevalent circumstances.

Chapter 10

Discussion and Future Work

The novel TFM linear machine, presented in this thesis, is mainly considered for use in a Linear Free Piston Energy Converter FPEC. The aim with the FPEC unit is to enable full implementation of Homogeneous Charge Compression Ignition HCCI, where it is possible to achieve high efficiency together with very low level of Nitrogen oxide emissions. One of the biggest challenges with the FPEC is the requirement of low moving mass i.e. the mass of the translator in the electrical machine. Based on the previous studies, where different types of machines have been investigated, it was concluded that the only promising candidates were the permanent magnet machines and TFM in particular.

The TFM machines are generally renowned for their high force/torque density but also for their complex structure which make them difficult to manufacture. This was also partly confirmed by the earlier designed low-leakage TFM topology prototype which suffered from partial demagnetization of the magnets, magnet pole displacement which resulted in high loss of useful flux. Therefore in the novel TFM strong emphasis was put in not only the electromagnetic performance but also in the manufacturing process of the machine. The novel TFM model is perfectly suited for a linear machine with a tubular cross section. The stator can be manufactured easily and is as simple to produce as the stator of a conventional rotary machine. The magnets are easily assembled on the translator with the new two-glue method. By this method the magnets are glued on a fixture, with a special fast hardening glue, before they are glued on the translator with another type of glue which cures at a higher temperature. By exposing the glues to higher temperatures, the glue between the magnets and the fixture, will slowly loose its adhesive properties while the glue between the magnets and the translator will cure, thus the magnets will be stuck to the translator and the fixture can easily be removed. Here it should be noted that the fast hardening glue has to be chosen carefully with respect to its

temperature capability. It is important that the curie temperature of the magnets, which is the maximum allowable temperature before the magnets demagnetize, is not exceeded. The fast hardening glue has to loose all its adhesive abilities before this temperature. This method turned out to be very effective in preventing a misalignment of the stator and translator poles. This was also evident from the agreement between simulated and measured results which was very good.

The novel TFM concept offers different options both for stator winding arrangement and translator magnet arrangement. Choice of the winding arrangement can influence the choice of the magnet configuration. In this thesis some of the winding and magnet arrangements are investigated in detail.

Two different winding arrangements abbreviated as local and global winding design have been studied. In the local winding design the winding is wound around each tooth separately while in the global winding design the winding is similar to the concentrated winding in conventional rotary machines. One major difference between these two configurations is utilization of the magnets on the translator. Local winding arrangement has the advantage in simultaneous utilization of all magnets. However, the disadvantage is that the space between two stator stacks has to be reserved for the coils. Thus, the peculiar quality of a TFM which is the ability to increase the power rating of the machine by increasing the number of poles in the machine is lost. Another disadvantage of the local winding design is the complexity of the winding process. Therefore, the global winding design was chosen for further detailed investigation.

Investigation of the different magnet arrangements has shown that two topologies have the potential to minimize the weight of the translator: the buried magnet and Halbach magnet designs. A common feature shared by both topologies is that they do not require any iron in the translator back like the surface mounted magnets. Thus, the weight of the translator can be minimized.

Advantages of the buried magnet design compared with the Halbach magnet design is that it requires fewer magnet pieces which makes the design cheaper and makes some simplification in the manufacturing process. Therefore the buried magnet design was analyzed first. However, the analytical analysis showed a major weakness of this design; there was considerable amount of leakage flux between the adjacent poles on the translator. Only a fraction of the flux, produced by the magnets, entered the stator. In the Halbach magnet design one of the magnets, just like in the buried magnet design, is oriented in the circumferential direction. Thus, there is a risk that the Halbach magnet design will suffer from the same weakness as the buried magnet design i.e. large leakage flux. This, however, has not been investigated at a detailed level. Instead, the focus was put to the more conventional surface magnet design.

Analytical analysis

A simple analytical model, used in the beginning of the investigation of the electromagnetic properties, overestimated the flux linkage by more then double, which is why a new improved analytical model was developed. Due to the 3D-nature of the flux in the machine, it was not possible to identify a suitable 2D-geometry for an analytical magnetic field distribution analysis. Instead, in such analysis all three dimensions in the machine have to be considered, which make the analysis very complicated and time consuming. Hence, the new analytical model is based on the determination of different reluctance paths, which takes into account the reluctances in all three dimensions.

Both armature reaction and the flux from the magnets have been investigated. In the investigation of the flux generated only from the magnets, depending on the translator position, three different reluctance models have been identified. It should be noted, however, that the number of different reluctance models is strongly related to the ration between the length of the magnet, the length of the pole and the length of the stator stack. The results obtained from the analytical model showed good agreement with the simulated and the measured results. The small remaining difference could be further reduced by better modeling of the reluctance paths. Each reluctance could be divided into a several smaller reluctances thereby achieving a denser reluctance grid and better agreement of the results. However, a higher number of reluctance parts would also result in a longer computation time. An acceptable solution is a compromise between the accuracy in the results on one hand and the computation time on the other.

In the analysis of the armature reaction flux alone, the magnets are treated as air, thus, the position of the translator does not affect the reluctance paths seen by the flux. The comparison of the analytical and simulated results showed a difference of about 15-20%. As mention, this difference can be reduced by implementing a denser reluctance grid.

The cogging force in the machine is investigated both analytically and with 3D-FEM simulations. Two different analytical methods, which are based on the analysis of the flux density distribution on the side of the tooth in the axial direction (between two stator stacks) are used. By integrating the flux density the cogging force in the machine is calculated. The results obtained from one method were unacceptable, whereas the other method, based on conformal mapping, showed better agreement with the measured and simulated values. Because, conformal mapping is inherently a 2D-geometry solution, a certain simplification of the real flux density distribution is introduced. Thus, this method should be used with a certain precaution.

FEM-analysis

A 3D FEM model was developed and analyzed. Due to the symmetry in the machine only two pole lengths have been simulated.

Investigation of the flux linkage, force and cogging force showed a close agreement with the results obtained from the measurements. The maximum force developed from the simulated results indicated a value of 900 N. This is less than half the value predicted by the simple analytical model 2540 N. Similar results are obtained with the no load EMF where the calculated value was 220 V(RMS) and the measured value was about 80 V(RMS).

The 3D-FEM model was extensively used in order to gain a better knowledge for the reason behind the lower performance. The simulation results showed a large leakage flux between the adjacent poles in the direction of motion. The same phenomenon was observed in the improved analytical model where these reluctance paths were taken into account.

Close agreement was also obtained between the simulated and measured values of the inductance and resistance of the machine. A small disagreement of the results in the inductance depends on the simulation model, where only two pole lengths of the machine are simulated. Hence, the end effects in the machine are not included in the simulation results.

Measurements

As mentioned, there was a close agreement between the measured, analytical and especially FEM-simulated values. The only disagreement between simulated and measured results was found at load conditions. However, this is mostly based on the motion profile of the machine in the measurements. In an ideal situation the machine should have a sinusoidal speed profile which also was introduced in the simulation model. However, due to the mechanical connection between the novel linear TFM and a conventional rotating machine, this speed profile was not maintained. Hence, the disagreement was not only in the amplitude but also in the frequency.

Future work

The challenge here is to enhance the electromagnetical performance of the machine while keeping the simplicity in the manufacturing process. One way to enhance the performance of the machine is to significantly reduce the leakage flux. This can be achieved by inserting an iron peace in the stator between two stator stack so that the inactive magnetic pole is short circuited. In addition, the magnetic circuit can be further improved by isolating the magnetic poles on the translator, where iron between two adjacent poles is replaced by some other nonmagnetic material. However, both improvements add some complexity in the manufacturing process.

Another alternative is to use the local winding design. As mentioned, in this design all magnets are used simultaneously. Hence, there is less risk for a high leakage flux. However, even this design will imply further complexity in the manufacturing process.

Some of the more important issues that can be investigated in future work are given below:

- Improving the analytical model. There was still some disagreement between the results from the improved analytical model and measured and FEM-simulated results. In order to improve the analytical model the reluctance paths, that have been derived, can be further divided into several more paths.
- Detailed investigation of the local winding design. This will probably require 3D-FEM investigation in order to make sure that the leakage flux is not underestimated.
- Optimal length of the magnet. Use the improved analytical model together with 2D-FEM analysis in order to find an optimal length ratio between the length of the pole and the length of the magnet.
- Investigation of the performance of the novel concept when the poles in the translator are isolated from each other and when an extra iron piece is inserted between two stator stacks.

Bibliography

[1] K.T. Chau and C.C. Chan. Emerging Energy-Efficient technologies for hybrid electric vehicles. *Proceedings of the IEEE*, 95(4):821–835, 2007.

[2] *Toyota hybrid synergy drive information terminal*, 23 edition, 07 2009.

[3] V. Wouk. Hybrids: then and now. *Spectrum, IEEE*, 32(7):16–21, 1995.

[4] K. Chen, A. Bouscayrol, A. Berthon, P. Delarue, D. Hissel, and R. Trigui. Global modeling of different vehicles. *Vehicular Technology Magazine, IEEE*, 4(2):80–89, 2009.

[5] Jorgen Hansson. *Analysis and Control of a Hybrid Vehicle Powered by a Free-Piston Energy Converter*. KTH, Stockholm Sweden, 2006.

[6] Erik Nordlund. *The Four-Quadrant Transducer System*. KTH, Stockholm Sweden, 2005.

[7] Freddy Magnussen. *On design and Analysis of synchronous Permanenr MAgnet Machines for Field-weakning Operation*. KTH, Stockholm Sweden, 2004.

[8] J.M. Miller. Hybrid electric vehicle propulsion system architectures of the e-CVT type. *Power Electronics, IEEE Transactions on*, 21(3):756–767, 2006.

[9] C.C. Chan. An overview of electric vehicle technology. *Proceedings of the IEEE*, 81(9):1202–1213, 1993.

[10] C.C. Chan. Present status and future trends of electric vehicles. In *Advances in Power System Control, Operation and Management, 1993. APSCOM-93., 2nd International Conference on*, pages 456–469 vol.1, 1993.

[11] Yimin Gao and M. Ehsani. Design and control methodology of plug-in hybrid electric vehicles. In *Vehicle Power and Propulsion Conference, 2008. VPPC '08. IEEE*, pages 1–6, 2008.

[12] Jakob Fredriksson. *Modeling of a free piston energy converter*. Chalmers University of Technology, Göteborg Sweden, 2006.

[13] R. Mikalsen and A.P. Roskilly. A review of free-piston engine history and applications. *Applied Thermal Engineering*, 27(14-15):2339–2352, October 2007.

[14] Waqas M. Arshad. *A Low-Leakage Linear Transversal-Flux Machine for a Free-Piston Generator*. KTH, Stockholm Sweden, 2003.

[15] Jens Linback & Alija Cosic. *Undersökning och systemsimulering av en frikolvsgenerator*. KTH, Stockholm Sweden, 2003.

[16] M. West, S. Long, Jiabin Wang, C. Bingham, and D. Howe. Emergency braking for free piston energy converters. In *Power Electronics and Applications, 2005 European Conference on*, pages 8 pp.–P.8, 2005.

[17] W.R. Cawthorne, P. Famouri, Jingdong Chen, N.N. Clark, T.I. McDaniel, R.J. Atkinson, S. Nandkumar, C.M. Atkinson, and S. Petreanu. Development of a linear alternator-engine for hybrid electric vehicle applications. *Vehicular Technology, IEEE Transactions on*, 48(6):1797–1802, 1999.

[18] D. Carter and E. Wechner. The free piston power pack: sustainable power for hybrid electric vehicles. *SAE Paper 2003-01-3277*, 2003.

[19] Pempek system webpage. 08 2009.

[20] O. Vysok. Linear combustion engine as main energy unit for hybrid vehicles. *Proceedings of Transtec Prague. Prague: Czech Technical University*, 2007.

[21] G. Kastinger. Design of of a novel tranverse flux machine. 2002.

[22] Peethamparam Anpalahan. *Design of Transverse flux Machines using Analytical Calculations and Finite Element Analysis*. KTH, Stockholm, Sweden, 2001.

[23] E.R.Laithwaite, J.F. Eastham, H.R. Bolton, and T.G.Fellows. Linear motors with transverse flux. *Proceedings of the IEE*, 118:1761–1767, 1971.

[24] H. Weh and H. May. Achievable force densities for permanent magnetexcited machines in new configurations. *Int. Conf. Electrical Machines*, 118:1107–1111, 1986.

[25] M.R. Harris, G.H. Pajooman, and S.M. Abu Sharkh. The problem of power factor in VRPM (transverse-flux) machines. In *Electrical Machines and Drives, 1997 Eighth International Conference on (Conf. Publ. No. 444)*, pages 386–390, 1997.

[26] G. Henneberger and M. Bork. Development of a new transverse flux motor. In *New Topologies for Permanent Magnet Machines (Digest No: 1997/090), IEE Colloquium on*, pages 1/1–1/6, 1997.

[27] M.R. Harris, G.H. Pajooman, and S.M. Abu Sharkh. Performance and design optimisation of electric motors with heteropolar surface magnets and homopolar windings. *Electric Power Applications, IEE Proceedings* -, 143(6):429–436, 1996.

[28] Maxime R. Dubois. Clawpole Transverse-Flux machine with hybrid stator. In *ICEM 2006 International Conference on Electrical Machines*, Kreta, 2006.

[29] M.R. Harris and B.C. Mecrow. Variable reluctance permanent magnet motors for high specific output. In *Electrical Machines and Drives, 1993. Sixth International Conference on (Conf. Publ. No. 376)*, pages 437–442, 1993.

[30] H. Weh. Transverse flux (tf) machines in drive and generator application. In *Stockholm Power Tech Conference*, page Invited Paper, Stockholm, 1995.

[31] M.R. Harris, G.H. Pajooman, and S.M. Abu Sharkh. The problem of power factor in vrpm (transverse-flux) machines. In *Electrical Machines and Drives, 1997 Eighth International Conference on Conf. Publ. No. 444*, pages 386–390, 1997.

[32] W.M. Arshad, T. Backstrom, and C. Sadarangani. Investigating a transverse flux machine with intermediate poles. In *Power Electronics, Machines and Drives, 2002. International Conference on (Conf. Publ. No. 487)*, pages 325–328, 2002.

[33] Johan van den Oever. *First analysis of moving part.* Number WP6. Breda Holland, 2003.

[34] Chandur Sadarangani. *Electrical Machines, Design and Analysis of Induction and Permanent Magnet Motors.* KTH Högskoletryckeriet, Stockholm, Sweden, 2000.

[35] Jacek F. Gieras and Mitchell Wing. *Permanent Magnet Motor Technology Revised (Electrical Engineering and Electronics, 113).* CRC, 2002.

[36] Zweygbergk S. Us patent no: 5117142. US patent office, 1992.

[37] Floarance Libert. *Design, Optimization and Comparioson of Permanent Magnet Motors for a Low-Speed Direct-Driven Mixer*. KTH, Stockholm Sweden, 2004.

[38] J. Cros and P. Viarouge. Synthesis of high performance pm motors with concentrated windings. *IEEE Transactions on Energy conversion*, 17(2):248–253, 2002.

[39] K. Halbach. First order perturbation effects in iron-dominated two-dimensional symmetrical multipoles. *Nuclear Instruments and Methods*, 74(1):147–164, October 1969.

[40] K. Halbach. Design of permanent multipole magnets with oriented rare earth cobalt material. *Nuclear Instruments and Methods*, 169(1):1–10, February 1980.

[41] D.L. Trumper, M.E. Williams, and T.H. Nguyen. Magnet arrays for synchronous machines. In *Industry Applications Society Annual Meeting, 1993., Conference Record of the 1993 IEEE*, pages 9–18 vol.1, 1993.

[42] David K. Cheng. *Field and Wave Electromagnetics (2nd Edition) (Addison-Wesley Series in Electrical Engineering)*. Addison-Wesley, 1989.

[43] Duane C. Hanselman. *Brushless Permanent Magnet Motor Design*. The Writers' Collective, 2003.

[44] Edward P. Furlani. *Permanent Magnet & Electromechanical Devices: Materials, Analysis, and Applications (Electromagnetism)*. Academic Press, London UK, 2001.

[45] A. Demenko, L. Nowak, and W. Szelag. Reluctance network formed by means of edge element method. *Magnetics, IEEE Transactions on*, 34(5):2485–2488, 1998.

[46] Viktor Pinter. *Osnove Elektrotehnike (Knjiga Prva)*. Tehnička Knjiga, Zagreb, 1970. In Croatian.

[47] Gilbert Strang. *Introduction to Applied Mathematics*. Wellesley-Cambridge Press, 1986.

[48] Dmitry Sveckharenko. *On Analytical Modeling and Design of a novel Transverse Flux Generator for Offshore Wind Turbines*. KTH, Stockholm Sweden, 2007.

[49] M. Markovic, M. Jufer, and Y. Perriard. Determination of tooth cogging force in a hard-disk brushless dc motor. *Magnetics, IEEE Transactions on*, 41(12):4421–4426, 2005.

[50] Z.Q. Zhu and D. Howe. Analytical prediction of the cogging torque in radial-field permanent magnet brushless motors. *Magnetics, IEEE Transactions on*, 28(2):1371–1374, 1992.

[51] Miroslav Markovic. *Magnetic field analysis in electric motors using conformal mapping*. PhD thesis, Lausanne, 2004.

[52] Jiabin Wang, D. Howe, and G.W. Jewell. Fringing in tubular permanent-magnet machines: part II. cogging force and its minimization. *Magnetics, IEEE Transactions on*, 39(6):3517–3522, 2003.

[53] A. Cosic, C. Sadarangani, and J. Timmerman. Design and manufacturing of a linear transverse flux permanent magnet machines. In *Industry Applications Society Annual Meeting, 2008. IAS '08. IEEE*, pages 1–5, 2008.

[54] D.Y. Ohm, I. Drivetech, and V. Blacksburg. Dynamic model of PM synchronous motors. *Drivetech Inc., Blacksburg, Virginia, www. Drivetechinc. com*.

[55] Erik Hallén. *Elektricitetslära*. Almquist och Wiksell, Stockholm, 1953. In Swedish.

[56] R. Dutta and M.F. Rahman. A comparative analysis of two test methods of measuring d - and q -Axes inductances of interior Permanent-Magnet machine. *Magnetics, IEEE Transactions on*, 42(11):3712–3718, 2006.

[57] Florance Meier. *Permanent-Magnet Synchronous Machines with Non-Overlapping Concentrated Windings for Low-Speed Direc-Drive Applications*. KTH, Stockholm Sweden, 2008.

[58] R. Krishnan and P. Materu. Measurement and instrumentation of a switched reluctance motor. In *Industry Applications Society Annual Meeting, 1989., Conference Record of the 1989 IEEE*, pages 116–121 vol.1, 1989.

Appendix A

Reluctance model III

$$\mathcal{R}_{IIImp11} = \frac{h_m}{\mu_0 \cdot \mu_m \cdot w_m \cdot z} \tag{A.1}$$

$$\mathcal{R}_{IIImp12} = \frac{h_m}{\mu_0 \cdot \mu_m \cdot w_m \cdot (\ell_m - z)} \tag{A.2}$$

$$\mathcal{R}_{IIImn21} = \frac{h_m}{\mu_0 \cdot \mu_m \cdot w_m \cdot (\tau_p - \ell_m + z)} \tag{A.3}$$

$$\mathcal{R}_{IIImn22} = \frac{h_m}{\mu_0 \cdot \mu_m \cdot w_m \cdot (\tau_p - \ell_m - z)} \tag{A.4}$$

The reluctance for the opposite magnets (in the circumferential direction are given by $\mathcal{R}_{IIImn11} = \mathcal{R}_{IIImp11}$, $\mathcal{R}_{IIImn12} = \mathcal{R}_{IIImp12}$, $\mathcal{R}_{IIImp21} = \mathcal{R}_{IIImn21}$, and $\mathcal{R}_{IIImp22} = \mathcal{R}_{IIImn22}$

$$\mathcal{R}_{IIItb1} = \frac{\ell_m + h_{tb}}{2 \cdot \mu_0 \cdot \mu_i \cdot w_m \cdot h_{tb}} \tag{A.5}$$

$$\mathcal{R}_{IIItb2} = \frac{h_{tb} + \tau_p - \frac{3 \cdot \ell_m}{4}}{\mu_0 \cdot \mu_i \cdot w_m \cdot h_{tb}} \tag{A.6}$$

$$\mathcal{R}_{IIItb3} = \mathcal{R}_{IIItb1} \tag{A.7}$$

$$\mathcal{R}_{IIItb4} = \frac{\theta \cdot \left(R_{ti} + \frac{h_{tb}}{2}\right)}{\mu_0 \cdot \mu_i \cdot \ell_m \cdot h_{tb}} \tag{A.8}$$

$$\mathcal{R}_{IIIsb} = \frac{\theta \cdot \left(R_{so} - \frac{h_{sb}}{2}\right)}{\mu_0 \cdot \mu_i \cdot h_{sb} \cdot \ell_m} \tag{A.9}$$

$$\mathscr{R}_{IIIstt} = \frac{\hbar_{st} + \frac{\hbar_{sb}}{2}}{\mu_0 \cdot \mu_i \cdot w_t \cdot \ell_m} \tag{A.10}$$

$$\mathscr{R}_{IIIsts} = \frac{\hbar_{sts}}{\mu_0 \cdot \mu_i \cdot w_m \cdot \ell_m} \tag{A.11}$$

$$\mathscr{R}_{IIIg1} = \frac{\pi}{4 \cdot \mu_0 \cdot w_m} + \frac{\delta}{\mu_0 \cdot w_m \cdot z} \tag{A.12}$$

$$\mathscr{R}_{IIIg2} = \frac{\delta}{\mu_0 \cdot w_m \cdot (\ell_m - z)} \tag{A.13}$$

$$\mathscr{R}_{IIIg3} = \frac{\delta}{\mu_0 \cdot w_m \cdot \left(z - \frac{\ell_m}{2}\right)} \tag{A.14}$$

$$\mathscr{R}_{IIIg4} = \frac{\pi}{4 \cdot \mu_0 \cdot w_m} + \frac{\delta}{\mu_0 \cdot w_m \cdot \left(\frac{3 \cdot \ell_m}{2} - z\right)} \tag{A.15}$$

$$\mathscr{R}_{IIIg5} = \frac{\ell_{pa1}}{\mu_0 \cdot w_m \cdot z} \tag{A.16}$$

$$\mathscr{R}_{IIIg6} = \frac{\ell_{pa1}}{\mu_0 \cdot w_m \cdot \left(\frac{3 \cdot \ell_m}{2} - z\right)} \tag{A.17}$$

$$\mathscr{R}_{IIIg7} = \frac{\xi \cdot r_{pa2}}{\mu_0 \cdot w_m \cdot z} \tag{A.18}$$

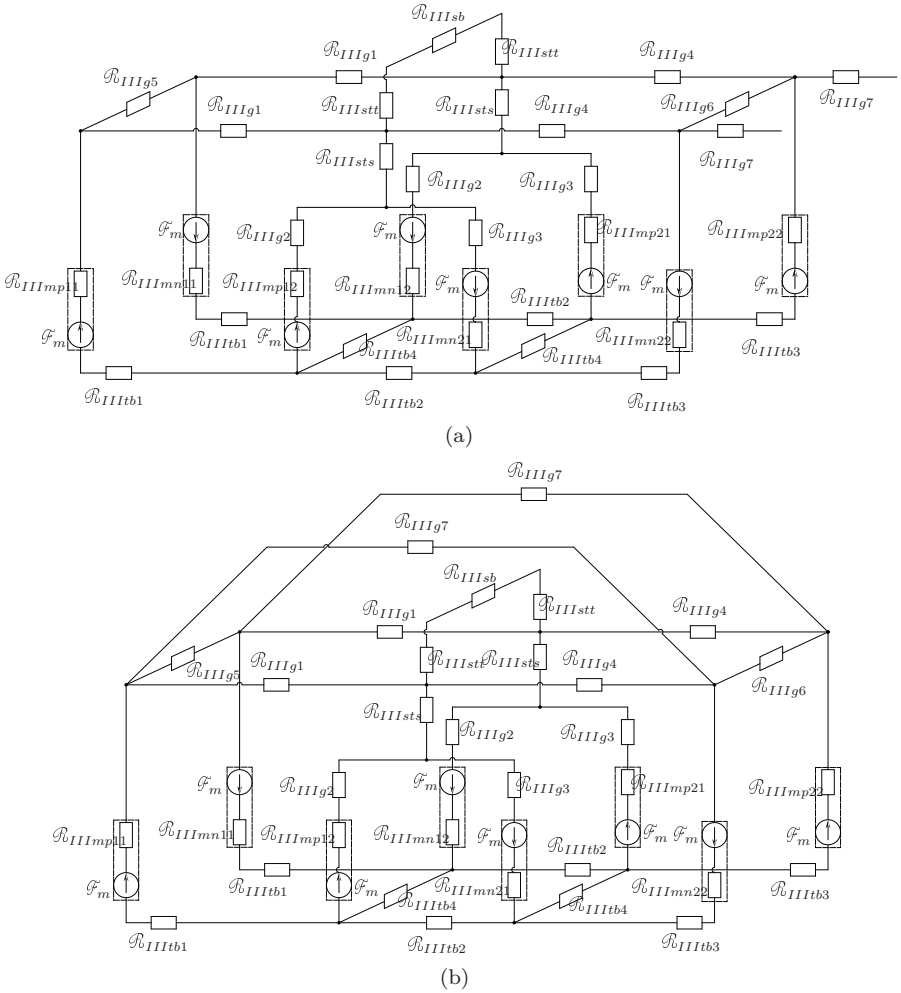

(a)

(b)

Figure A.1: *3D-reluctance network used in the analytical model $z > (\ell_{pole} - \ell_m)$ a) original b) modified due to the presence of symmetry.*

Appendix B

Nodal analysis

There exist several different methods for solving electrical circuit. This section presents an example of how a circuit is solved using the nodal method. This method is later used to solve the equivalent magnetic circuit.

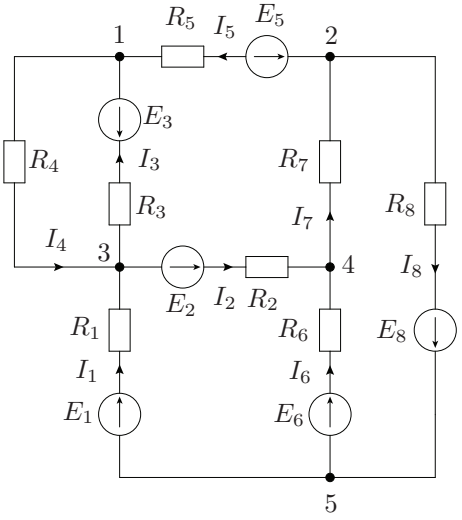

Figure B.1: *Circuit used in analysis.*

In order to solve this circuit or to derive a more general equation to solve similar circuits with more unknowns two laws are used, the Kirchhoff's first law and the Ohm's law.

One node is chosen as a reference whereupon the potential of this node is set equal to zero.

In this example node number 5 is chosen as a reference node. For the rest of the nodes Kirchhoff's first law gives the following equations:

$$I_3 + I_5 = I_4 \tag{B.1}$$
$$I_7 = I_5 + I_8 \tag{B.2}$$
$$I_1 + I_4 = I_3 + I_2 \tag{B.3}$$
$$I_7 = I_6 + I_2 \tag{B.4}$$

First the potential for different nodes using voltage sources and the voltage drops across the resistances can be written according to:

$$\nu_1 = \nu_3 + I_4 \cdot R_4 \tag{B.5}$$
$$\nu_1 = \nu_2 - E_5 - I_5 \cdot R_5 \tag{B.6}$$
$$\nu_1 = \nu_3 - E_3 - I_3 \cdot R_3 \tag{B.7}$$
$$\nu_3 = 0 + E_1 - I_1 \cdot R_1 \tag{B.8}$$
$$\nu_4 = 0 + E_6 - I_6 \cdot R_6 \tag{B.9}$$
$$\nu_2 = 0 - E_8 + I_8 \cdot R_8 \tag{B.10}$$
$$\nu_2 = \nu_4 - I_7 \cdot R_7 \tag{B.11}$$
$$\nu_4 = \nu_3 + E_2 - I_2 \cdot R_2 \tag{B.12}$$

Applying Ohm's law and using the equations above the currents in different branches can be calculated according to equations:

$$I_1 = (-\nu_3 + E_1) \cdot G_1 \tag{B.13}$$
$$I_2 = (\nu_3 + E_2 - \nu_4) \cdot G_2 \tag{B.14}$$
$$I_3 = (\nu_3 - E_3 - \nu_1) \cdot G_3 \tag{B.15}$$
$$I_4 = (\nu_1 - \nu_3) \cdot G_4 \tag{B.16}$$
$$I_5 = (\nu_2 - E_5 - \nu_1) \cdot G_5 \tag{B.17}$$
$$I_6 = (-\nu_4 + E_6) \cdot G_6 \tag{B.18}$$
$$I_7 = (\nu_4 - \nu_2) \cdot G_7 \tag{B.19}$$
$$I_8 = (\nu_2 + E_8) \cdot G_8 \tag{B.20}$$

Inserting equations B.13-B.20 into equations B.1-B.4 and after some rearrangement the following equations can be obtained:

$$\nu_1 \cdot G_{11} - \nu_2 \cdot G_5 - \nu_3 \cdot G_{13} = -E_3 \cdot G_5 - E_5 \cdot G_5 \tag{B.21}$$
$$-\nu_1 \cdot G_5 + \nu_2 \cdot G_{22} - \nu_4 \cdot G_7 = E_5 \cdot G_5 - E_8 \cdot G_8 \tag{B.22}$$
$$-\nu_1 \cdot G_{13} + \nu_3 \cdot G_{33} - \nu_4 \cdot G_2 = E_1 \cdot G_1 - E_2 \cdot G_2 + E_3 \cdot G_3 \tag{B.23}$$
$$-\nu_2 \cdot G_7 - \nu_3 \cdot G_2 + \nu_4 \cdot G_{44} = E_2 \cdot G_2 + E_6 \cdot G_6 \tag{B.24}$$

where $G_{11} = G_3 + G_4 + G_5$, $G_{22} = G_5 + G_7$, $G_{33} = G_1 + G_2 + G_3 + G_4$, $G_{44} = G_2 + G_6 + G_7$ and $G_{13} = G3 + G_4$. If the conductance G_2, G_5 and G_7 in the equations B.21-B.24 is replace by $G_2 = G_{34} = G_{43}$, $G_5 = G_{12} = G_{21}$ and $G_7 = G_{24} = G_{42}$ it can be realized that the equations above can be written in the following form

$$+\nu_1 \cdot G_{11} - \nu_2 \cdot G_{12} - \nu_3 \cdot G_{13} - \nu_4 \cdot G_{14} = \sum_{\substack{1 \\ j \neq 1}}^{5} E_{1j} \cdot G_{1j} \tag{B.25}$$

$$-\nu_1 \cdot G_{21} + \nu_2 \cdot G_{22} - \nu_3 \cdot G_{23} - \nu_4 \cdot G_{24} = \sum_{\substack{1 \\ j \neq 1}}^{5} E_{2j} \cdot G_{2j} \tag{B.26}$$

$$-\nu_1 \cdot G_{31} - \nu_2 \cdot G_{32} + \nu_3 \cdot G_{33} - \nu_4 \cdot G_{34} = \sum_{\substack{1 \\ j \neq 1}}^{5} E_{3j} \cdot G_{3j} \tag{B.27}$$

$$-\nu_1 \cdot G_{41} - \nu_2 \cdot G_{42} - \nu_3 \cdot G_{43} + \nu_4 \cdot G_{44} = \sum_{\substack{1 \\ j \neq 1}}^{5} E_{4j} \cdot G_{4j} \tag{B.28}$$

In a more general form for the potential in node p the equation can be written as:

$$\nu_p \cdot G_{pp} - \sum_{\substack{j=1 \\ j \neq p}}^{n} \nu_j \cdot G_{jp} = \sum_{\substack{j=1 \\ j \neq p}}^{n} E_{pj} \cdot G_{pj} \tag{B.29}$$

If there exist a so called super node, where one branch only contains the voltage source this analysis cannot be applied. As is evident from Equation B.29 the voltage source has to multiplied by the conductance of that branch. If the conductance is not present i.e. $G = 0$ there will be no contribution from that voltage source and the analysis will fail. However, the circuit can be modified so that the super node is eliminated, whereupon the nodal analysis can be applied to the new circuit. The elimination of the super node is shown in figure B.2.

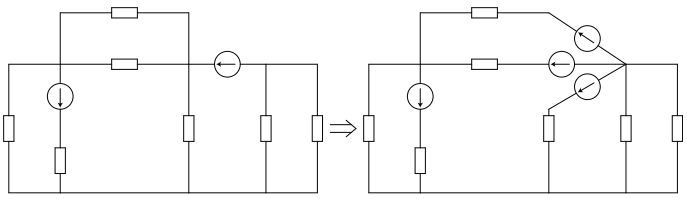

Figure B.2: *Example of elimination of a super node.*

Appendix C

Circuit modeling in Flux3D

The Flux3D software enables a circuit to be coupled to the meshed geometry. In this way, voltages and fluxes are easily obtained in the postprocessing.

Force measurement

During the static simulations, the value of the current is defined directly in the coil and therefore no circuit is necessary. Total phase winding consists of four coils. Two coils that share the same slot must have current defined in the same direction. This is illustrated in Figure C.1.

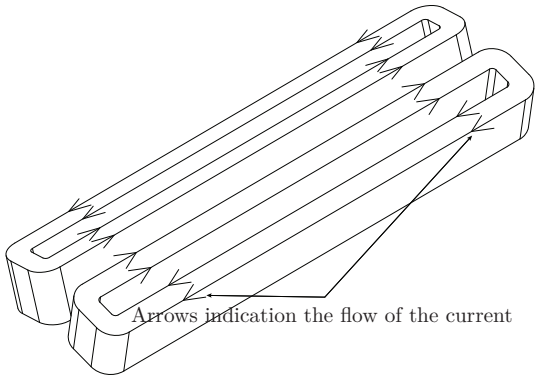

Figure C.1: *Example of coil orientation for two coils that share same slot.*

No load voltage

In the simulation software, both a winding and a circuit can be oriented independently. The circuit together with the winding controls the power

flow. It is very important that these two are oriented in a way that the resultant current flows in the desired direction.

In order to simulate the no load voltage the circuit in Figure C.2(a) is used. The resistances in the circuits are put to a very high value, which will represent the high impendence at the terminals. Thus, the current in the circuit will be negligible. The speed profile is dedicated to the translator and the no load voltage is obtained from the simulations.

Inductance

The simulated part represent only 1/8 of the total machine, hence, only 1/8 of the inductance will be present in the simulations. In order to match the real current and the voltage in the machine the resistance in the circuit needs also to be 1/8 of the total value.

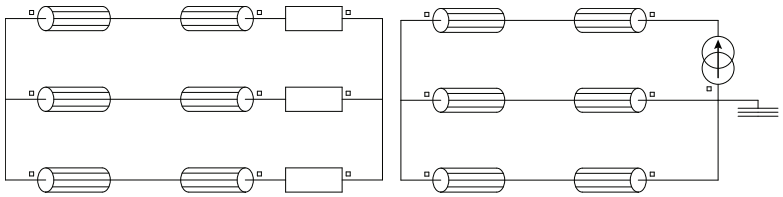

Figure C.2: *circuit diagrams used in simulations a) no load voltage simulations b) inductance simulations.*

Figure C.2(b) shows the circuit used in the simulations.

Appendix D

Machine dimensions

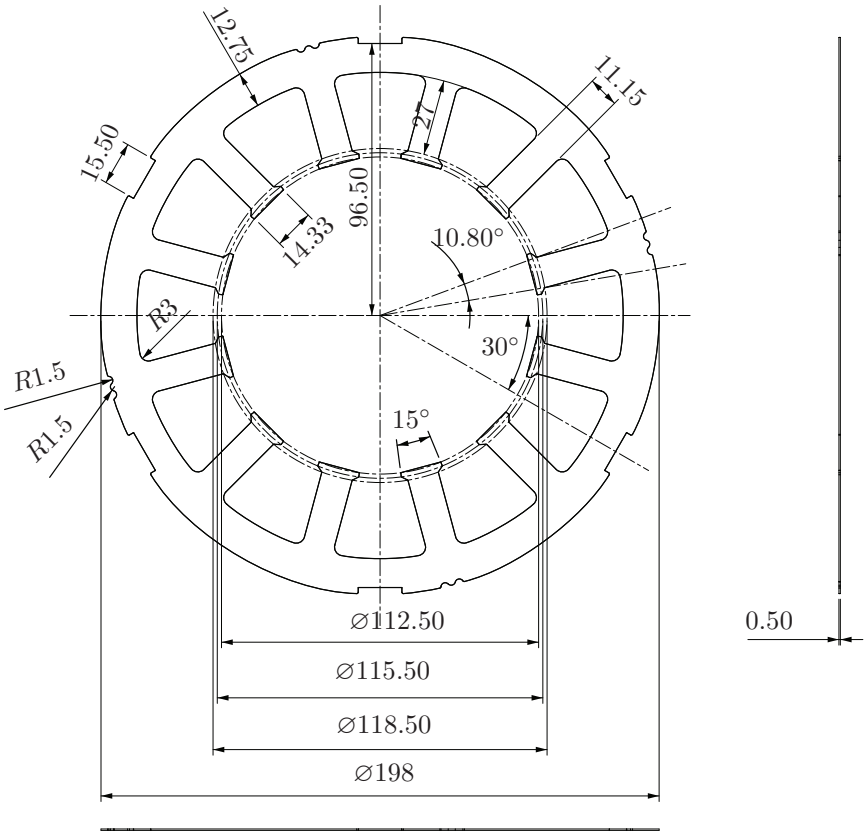

Figure D.1: *Dimensioning details for the stator laminations.*

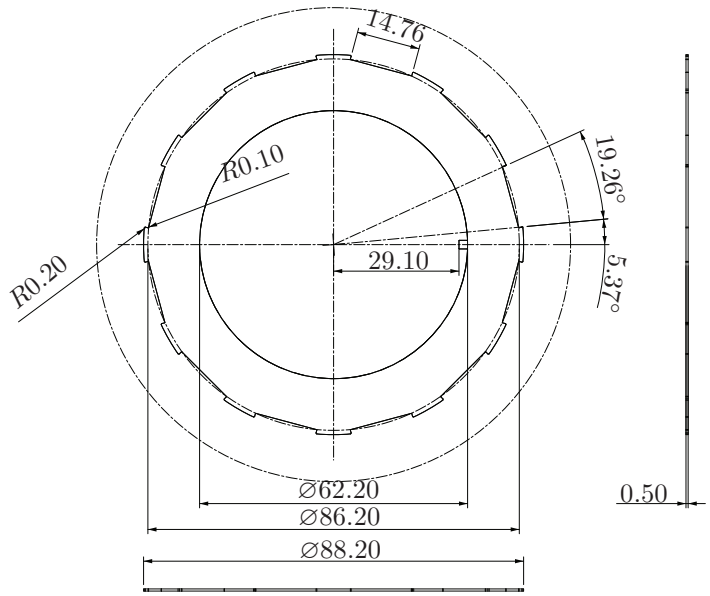

Figure D.2: *Dimensioning details for the translator laminations.*

Appendix E

List of symbols

Dimensioning details

τ_p	Length of the pole pitch	[m]
τ_s	Length of the slot pitch	[m]
ℓ	Length	[m]
ℓ_m	Length of the magnet	[m]
ℓ_s	Length of the stator	[m]
ℓ_t	Length of the translator	[m]
ℓ_{stroke}	Length of the stroke	[m]
ℓ_{end}	Length of the end winding	[m]
$\hbar_{tb}$	Hight of translator back	[m]
$\hbar_{sb}$	Hight of stator back	[m]
$\hbar_{st}$	Hight of stator tooth	[m]
$\hbar_{sts}$	Hight of stator tooth shoe	[m]
$\hbar_{stst}$	Hight of stator tooth shoe tip	[m]
$\hbar_m$	Hight of magnet	[m]
w_m	Width of the magnet	[m]
w_t	Width of the stator tooth	[m]
r	Radius	[m]
R_{ti}	Inner radius of the translator	[m]
R_t	Radius of the translator without magnets	[m]
R_{to}	Outer radius of the translator	[m]
R_{si}	Inner radius of the stator	[m]
R_{so}	Outer radius of the stator	[m]
R_{scu}	Inner radius of the slot insulation	[m]
R_{cu}	Radius of the conductor in the machine	[m]
R_c	Radius of a conductor	[m]
R_{ew}	Radius of the end winding	[m]
D_{to}	Outer diameter of the translator	[m]

δ	Height of the air gap (electromagnetic)	[m]
δ'	Relative height of the air gap and the magnet	[m]
δ_e	Equivalent height of the air gap (electromagnetic)	[m]
b_0	Distance between two stator stacks	[m]
x	Percentage of total distance between two stator stacks	[-]
A	Area	[m^2]
A_{cu}	Area of the conductor in the machine	[m^2]
A_{ins}	The insulated copper area	[m^2]
A_{slott}	Area of the slot	[m^2]
α_{shoe}	Angle of the stator tooth shoe	[rad]
α_{tooth}	Angle of the stator tooth	[rad]
θ	Angle of the slot pitch	[rad]
β	Angle of the slot opening	[rad]
ξ	Angle for calculation of the reluctance $\mathscr{R}_{g4}$	[rad]
ϵ	Angle for calculation of the reluctance	[rad]
γ	Angle for calculation of the reluctance $\mathscr{R}_{g4}$	[rad]
w_{pa}	Width of a path for calculation of a reluctance	[m]
h_{pa}	Height of a path for calculation of a reluctance	[m]
r_{pa}	Radii of a path for calculation of a reluctance	[m]
l_{pa}	Length of a path for calculation of a reluctance	[m]

Reluctances

$\mathscr{F}$	mF source	[A]
$\mathscr{R}_{mp}$	Reluctance of positive oriented magnet	$[\frac{\text{At}}{\text{Wb}}]$
$\mathscr{R}_{mn}$	Reluctance of negative oriented magnets	$[\frac{\text{At}}{\text{Wb}}]$
$\mathscr{R}_{tb}$	Reluctance of the translator back	$[\frac{\text{At}}{\text{Wb}}]$
$\mathscr{R}_{stt}$	Reluctance of the upper part of the stator tooth	$[\frac{\text{At}}{\text{Wb}}]$
$\mathscr{R}_{sts}$	Reluctance of the stator tooth shoe	$[\frac{\text{At}}{\text{Wb}}]$
$\mathscr{R}_{st}$	Reluctance of the stator tooth total	$[\frac{\text{At}}{\text{Wb}}]$
$\mathscr{R}_{sb}$	Reluctance of the stator back	$[\frac{\text{At}}{\text{Wb}}]$
$\mathscr{R}_{g}$	Reluctance in the air gap	$[\frac{\text{At}}{\text{Wb}}]$
$\mathscr{R}_{stsl}$	Reluctance of the stator tooth shoe leakage	$[\frac{\text{At}}{\text{Wb}}]$
$\mathscr{R}_{stl}$	Reluctance of the stator tooth leakage	$[\frac{\text{At}}{\text{Wb}}]$
Subscript I	Reluctance of the first reluctance model	[-]
Subscript II	Reluctance of the second reluctance model	[-]
Subscript III	Reluctance of the third reluctance model	[-]
Subscript IV	Reluctance of the armature reaction flux model	[-]
Subscript a	Reluctance in the air (between two stator stacks)	[-]

Electrical parameter

W_m	Magnetic energy	[J]

W	Energy	[J]
Λ	Total flux linkage	[Wb]
Ψ	Total flux linkage	[Wb]
ϕ	Flux	[Wb]
λ	Specific coefficient	[-]
θ_e	Electrical degree	[rad]
P	Active power	[W]
Q	Reactive power	[VAr]
F	Force	[N]
F_d	Force density	$[\frac{\mathrm{N}}{\mathrm{m}^2}]$
F_{cog}	Cogging force	[N]
E	Voltage	[V]
e	Induced voltage	[V]
EMF	Electro Magnetic Force	[V]
E_{tooth}	Voltage in one tooth	[V]
E_{phase}	Voltage in one phase	[V]
ϕ	Flux	[Wb]
$\hat{\phi}_{NI}$	Peak flux from armature reaction alone	[Wb]
$\hat{\phi}_{mag}$	Peak flux from magnets alone	[Wb]
f	Frequency	[Hz]
t	Time	[s]
U	Voltage	[V]
R	Resistance	[Ω]
X_q	Reactance in q-direction	[Ω]
X_d	Reactance in d-direction	[Ω]
I_{phase}	RMS current in one phase	[A]
I_a	RMS current in one phase	[A]
I_q	q-axis current	[A]
I_d	d-axis current	[A]
v	Speed	$[\frac{\mathrm{m}}{\mathrm{s}}]$
k_f	Waveform factor	[-]
k_{fill}	Fill factor	[-]
$\hat{B}_\delta$	Peak flux density in the air gap	[T]
B_{rm}	Remanent flux density of the magnet	[T]
B_{mag}	Flux density in the air gap	[T]
B_m	Flux density in the air gap	[T]
B_n	Flux density normal comp. to the surface	[T]
B_t	Flux density tangential comp. to the surface	[T]
B_{tb}	Flux density on the side of the stator tooth (ax. dir.)	[T]
B_{rb}	Relative flux density in the air gap	[T]
B_0	Flux density at the surface just inside the magnet	[T]
H_n	Magnetic field intensity nor. comp. to the surface	$[\frac{\mathrm{A}}{\mathrm{m}}]$
H_t	Magnetic field intensity tan. comp. to the surface	$[\frac{\mathrm{A}}{\mathrm{m}}]$

H_x	Magnetic field intensity in comp. plane x-comp.	$[\frac{\mathrm{A}}{\mathrm{m}}]$
H_y	Magnetic field intensity in comp. plane y-comp.	$[\frac{\mathrm{A}}{\mathrm{m}}]$
H_w	Magnetic field intensity in comp. plane	$[\frac{\mathrm{A}}{\mathrm{m}}]$
z_e	Axial position	[m]
S_δ	Current loading	$[\frac{\mathrm{A}}{\mathrm{m}}]$
n_{stack}	Number of stacks in the machine	[-]
n	Number of turns	[-]
n_s	Number of turns in one coil	[-]
n_1	Number of turns in one phase	[-]
n_{slot}	Number of turns in one slot	[-]
$n_{s_{effective}}$	Effective number of turns in a phase (local wind.)	[-]
q_s	Number of slots in the machine	[-]
L_{main}	Main inductance	[H]
L_{slot}	Slot leakage inductance	[H]
L_{leak}	Air gap leakage inductance	[H]
L_{line}	Inductance of a circular inductor	[H]
L_{stack}	Main inductance	[H]
L_{end}	End winding inductance	[H]
L_{tot}	Total phase inductance	[H]
L_a	Self inductance phase a	[H]
L_0	DC component self inductance	[H]
L_1	Self inductance	[H]
M_{ac}	Mutual inductance phase a and c	[H]
M_0	DC component mutual inductance	[H]
M_1	Mutual inductance	[H]
μ_m	Permeability of the magnet	$[\frac{\mathrm{H}}{\mathrm{m}}]$
μ_{rm}	Relative permeability of the magnet	[-]
μ_{ri}	Relative permeability of the iron	[-]
μ_0	Permeability of vacuum	$[\frac{\mathrm{H}}{\mathrm{m}}]$
μ_1	Permeability of material 1	$[\frac{\mathrm{H}}{\mathrm{m}}]$
μ_2	Permeability of material 2	$[\frac{\mathrm{H}}{\mathrm{m}}]$
φ	Angle between phase voltage and phase current	[rad]
ζ	Angle between induced voltage and phase current	[rad]
ϖ	Angle between induced voltage and phase current	[rad]
ϑ	Magnet and air gap permeance	$[\frac{\mathrm{Wb}}{\mathrm{At}}]$
$\tilde{\vartheta}$	Relative magnet and air gap permeance	[-]